12-2012

Development of a Two-dimensional Model of a Pneumatic Tire

Timothy Lewis
Clemson University, tlewis3348@gmail.com

DEVELOPMENT OF A TWO-DIMENSIONAL MODEL OF A PNEUMATIC TIRE

A Thesis
Presented to
the Graduate School of
Clemson University

In Partial Fulfillment
of the Requirements for the Degree
Master of Science
Mechanical Engineering

---

by
Timothy R. Lewis
December 2012

Accepted by:
Dr. Paul F. Joseph, Committee Chair
Dr. Timothy B. Rhyne
Dr. Gang Li

ABSTRACT

The pneumatic tire has been studied extensively since its invention in 1888. With the advent of high-powered computers and the use of the finite element method, the understanding of the tire's complex non-linear behavior has grown tremendously. However, one weakness of finite element models is that parameter studies are difficult and time consuming to perform. In contrast, an analytical model can quickly and easily perform extensive parameter studies. To the knowledge of the author, all existing analytical models of the tire make assumptions concerning the tire's behavior and construction that while useful for obtaining some of the first-order characteristics, are limited since they cannot relate tire behavior such as force-deflection to individual tire stiffnesses. As such, an adequate two-dimensional model of a pneumatic tire, including a finite element model, does not exist.

Therefore, an analytical, two-dimensional model for a pneumatic tire in static contact with a rigid surface is developed and presented. The case of a non-pneumatic tire can be obtained as a special case. The quasi-static investigation concentrates on finding the relationships between the tire's size and stiffness and its deformation under loading. A total of seven stiffness parameters are accounted for. The belt of the tire is modeled using curved beam theory, developed by Gasmi, et al. (2011), which accounts for bending (EI), shearing (GA), and extensional (EA) deformations. The sidewall of the tire is modeled as a bi-linear spring (K_r^T, K_r^C) with pre-tensioning (F_P^*) in the radial direction and a linear torsional spring (K_θ) in the circumferential direction. Application of virtual work leads to a set of sixth order differential equations for the displacements in the belt that must be solved in three distinct regions. The first region is the region where the radial deformation is greater than the radial deformation of

the inflated and unloaded tire. The second region is the region where the radial deformation of the sidewall is less than the inflated position but not in contact with the ground, and the third region is defined to be the region in contact with the ground.

The length of the contact patch is represented by the angle enclosed by the edges of contact, and analytical expressions of stress resultants and displacements at the centroids of cross-sections are expressed in terms of this angle. In order to improve the accuracy of the model for large deformations, a special inflation pressure was calculated that allowed the most accurate solution to the linear model to be obtained by minimizing the circumferential force in the region of the largest rotation of the curved beam. This solution was then modified to account for the true inflation pressure. This two-step solution procedure was validated with a geometrically nonlinear finite element model of a non-pneumatic tire.

Force vs. deflection and force vs. counter deflection results were compared to experimental data for a pneumatic tire for a range of inflation pressures from zero to four bar. From this, it is concluded that while it is clearly possible to match the data, more work needs to be done to determine the best method for determining parameters that match a real tire. Extensive sensitivity analysis was performed on all the stiffness parameters.

DEDICATION

I dedicate this work to my wife, Kathleen Lewis, who gave me the support, encouragement, prayer, and love I needed when everything was going well and when nothing seemed to be going right. I could not have done it without you.

ACKNOWLEDGEMENTS

I would like to extend my gratitude to some people for, without their help and guidance, the completion of this work would not have been possible.

I would like to, first of all, address my sincere thanks to my research advisor, Dr. Paul F. Joseph for his guidance and support throughout my studies. I am particularly grateful for his insight into the complex structural behavior present in the tire. Additionally, his patience with me as I learned how to understand and express complex concepts myself was very encouraging. Finally, his unceasingly optimistic outlook and refusal to be satisfied with an unsatisfactory match of the experimental data was a significant factor in motivating me to press on to the end.

Special thanks should also go to my research committee members and teachers Dr. Timothy B. Rhyne and Dr. Gang Li. Dr. Rhyne's extensive knowledge of tire behavior was invaluable, and without his advice and insight, successfully modeling the tire would have been significantly more difficult, if not, impossible. Dr. Li's challenging classes provided a solid foundation from which my current understanding was built.

Sincere gratitude is expressed to my family and especially to my wonderful wife, Kathleen Lewis, for their love, prayers, and support.

Additionally, I thank my office mates Dhananjay Joshi and Mohamed Trabelsi for the many stimulating conversations and moral support.

Furthermore, I greatly appreciate the financial support of both the Clemson University Undergraduate Mechanical Engineering Lab and the Michelin Americas Research and Development Company.

Last but not least, I praise my Lord and Savior Jesus Christ who created this marvelous universe, saved me from my sin and despair, and gave me the grace and strength to endure to accomplish this work.

TABLE OF CONTENTS

LIST OF TABLES

Table Page

LIST OF FIGURES

Figure Page

CHAPTER 1
–
LITERATURE SURVEY

Since its invention in 1888 by J.B. Dunlop, the pneumatic tire has been an integral part of the transition to motorized travel [1]. Due to the significant part that it plays in automotive design, much work has been done to understand how a tire responds in different situations. This has produced many different theoretical and empirical models to describe, among other things, the tire's dynamic, thermodynamic, and mechanical behavior; and predict such things as high-speed stability, rolling resistance, force and moment response, and hydroplaning. Due to its complexity, often the only viable approach is a fully non-linear three-dimensional finite element analysis. A tire's construction does not easily lend itself to a two-dimensional treatment. However, depending on the desired result and the required accuracy of the prediction, much can be gained by appropriate simplifications and analytical means.

The purpose of this research is to develop a two-dimensional analytical model of a pneumatic tire in static contact with a rigid ground. As much as possible, all the stiffening mechanisms in the belt and sidewall will be accounted for and the contact problem will be addressed with mathematical rigor. The model will predict the tire's deformation and use that information to analyze other aspects of its behavior. First, however, it is useful to survey the available literature on comparable approaches to pneumatic tires to determine how this research will further develop the understanding of tire behavior. For an extensive literature review on the status of tire behavior research, see Clark [2] and Gent and Walter [3].

Additionally, Ghoreishy [4] reviews the research that has been accomplished in the finite element modeling of pneumatic tires.

There are three different aspects of dynamic tire behavior that have been studied, namely, the natural frequencies and mode shapes, the force and moment response, and curve fitting of empirical data. Kung, et al. [5] analytically predict the natural frequencies and modes shapes of a pneumatic tire represented by a two-dimensional ring on an elastic foundation with radial and circumferential stiffnesses. The purpose for developing the analytical model was not to precisely predict the natural frequencies and mode shapes analytically, but rather to understand the cause of peculiarities in the solutions obtained using a finite element model. Therefore, because these peculiarities were observed over a wide range of parameters, there was no significant attempt to provide a means of accurately calculating parameters that correspond to a real tire. Kindt, et al. [6] developed a similar two-dimensional analytical model that is compared with a finite element model evidencing a strong correlation. The parameters for this model were calculated using modal analysis of experimental data. From this, it may be observed that the tire can be accurately modeled in these situations with linear radial and circumferential springs representing the carcass of the tire. The analytical model developed by Soedel and Prasad [7] allows the natural frequencies and mode shapes of a tire in contact with the ground to be determined from those found either experimentally or theoretically for a tire not in contact with the road. Huang and Soedel [8] compare the natural frequencies and mode shapes for both extensible and inextensible rolling rings. Additionally, the effect of the Coriolis forces that arise from a rolling ring as opposed to a stationary ring with a moving load is analyzed. These models are important for determining such things as stability at high speeds.

All of these models, with the exception of [7] neglect shear deformation due to making Euler-Bernoulli beam approximations, and assume a linear radial stiffness of the sidewall.

Brush models, represent a tire as a ring with a "tread" made of bristles that represents the combined spring of the actual tread, the belts, and the carcass. Pacejka [9], Chapter 3, gives an extensive literature review of the method as well as an extensive description of how the model is generally used. Velenis, et al. [10] develop a friction model for use in a brush model, which gives accurate analytical predictions of the force response and less accurate results for the aligning moment. The suggested likely cause of the reduced accuracy for the aligning moment is the approximation used to describe the contact pressure distribution. Gim and Nikravesh [11] accurately predicted the tire's lateral force using a model similar to the brush model but the model fails to produce accurate results for the predicted self-aligning torque. Shifrin [12] improved on Gim and Nikravesh's model and found that the discrepancy between the actual and theoretically predicted values for the self-aligning torque was due to assuming that the contact pressure was symmetric about the center of contact. In all of these models, the length of the contact patch is either used as an input parameter or approximated with the assumption that the tire behaves as a thin membrane.

Pacejka's "Magic Formula," extensively described in Pacejka [9], Chapter 4, is a semi-empirical model that allows accurate fitting of data from the tire's force and moment response, and is the accepted standard for empirically predicting the force and moment response of the tire.

Determining the rolling resistance of a tire is often done either empirically or computationally, due to the coupling of, among other things, internal pressure, temperature, loading, and velocity. Grover [13] fit rolling resistance test data in terms of a realistic fitting

equation dependent on inflation pressure, vertical load, and velocity. This fitting equation is now the standard in the industry (see SAE J2452). Nielsen and Sandberg [14] assume that the curve relating steady-state velocity to internal tire temperature is already known and present a dynamic model of rolling resistance based on that curve and a time constant to account for how the rolling resistance coefficient changes due to relatively quick changes in velocity. Hall and Moreland [15] give an extensive literature review on the study of rolling resistance. To the best knowledge of the author, there has not been any analytical examination of the effect of the tire's structural parameters on the rolling resistance.

Hydroplaning is a complex phenomenon resulting from the fluid-structural coupling of the tire and water. Sinnamon and Tielking [16] summarize the existing analytical analysis that has been done on the topic. The most important characteristics of a tire that determine the speed at which it hydroplanes are its inflation pressure and tread pattern. Since the publication of that paper, a significant amount of work has been done to predict the hydroplaning speed of a particular tire by numerical simulation in order to determine the effectiveness of the tread pattern. Oh, et al. [17] and Seta, et al. [18] are examples of some simulations that have been developed.

Koutný [19] and Rhyne [20] found the vertical stiffness of the tire in terms of air pressure, tire diameter, and tire width, with the assumption that the tire behaves as a membrane. Since finite element modeling has allowed such precise predictions of the tire's complex behavior, most of the analytical models of the tire considering the tire's structural aspects are from early literature. For example, Clark [21] attempts to predict the contact patch area of a rolling tire by modeling the tire's belts as an Euler-Bernoulli beam and its sidewall as a radial linear spring-damper. However, due to not accounting for a circumferential stiffness or

shear deformation, which are known to play significant roles in the deformation of the tire, it is unclear how useful this model is in representing a real tire. Gasmi, et al. [22] uses Timoshenko assumptions in a two-dimensional model of a ring in contact and applied that model to a non-pneumatic tire [23] and validated both models for small deflections with a finite element model. This model did not account for an internal pressure or the possibility of the spokes possessing any pre-tensioning, compressive stiffness, or shear stiffness. Furthermore, the use of linear geometry prevented the model from being valid for large deflections. Finally, when comparing the governing differential equations for the ring derived by Gasmi [22] for the Euler-Bernoulli case to those derived by Clark, it should be noted that significant differences exist. Furthermore, Gasmi [22] shows that for an Euler-Bernoulli beam, the pressure distribution should be characterized by spikes in pressure at the edge of contact. This characterization is not consistent with the depictions of the contact pressure profile shown by Clark. The source of this problem is difficult to pinpoint because although Gasmi clearly showed the derivation of his equations, Clark did not.

In many of these models, either the contact pressure profile or the relationship between contact pressure and vertical deflection (or contact length) is of vital importance. To find this relationship, the tire is often assumed to behave as either a thin membrane or an Euler-Bernoulli curved beam. The membrane approximation has been found to predict contact pressures that are between 85 and 90 percent of the actual contact pressures when the tire is inflated to a normal air pressure (see Gent and Walter [3], page 192) with lower accuracy at lower pressures. This suggests that a significant portion of the load is being supported by the structure of the tire. Additionally, it is known that the shearing mechanism plays a significant role in rubber deformation [24], and that the shear modulus can have a strong impact on the

contact pressure [25]. Furthermore, knowing the effect the structure of the tire has on its stiffness and shape could be beneficial for improving tire design in the future. This research presents an application of Gasmi's ring model to the pneumatic tire with the assumption that the sidewall can be modeled as a bi-linear spring with pre-tensioning in the radial direction and a linear spring in the circumferential direction.

WORKS CITED

[1] E. S. Tompkins, The History of the Pneumatic Tyre, Seattle: Eastland Press, 1981.

[2] S. K. Clark, Ed., Mechanics of Pneumatic Tires, 2nd ed., Washington, D.C.: National Highway Traffic Safety Administration, 1981.

[3] A. N. Gent and J. D. Walter, Eds., The Pnuematic Tire, Washington DC: National Highway Traffic Safety Administration, 2005.

[4] M. Ghoreishy, "A State of the Art Review of the Finite Element Modelling of Rolling Tyres," *Iranian Polymer Journal,* vol. 17, no. 8, pp. 571-597, August 2008.

[5] L. E. Kung, W. Soedel and T. Y. Yang, "Free Vibration of a Pneumatic Tire-Wheel Unit Using a Ring on an Elastic Foundation and a Finite Element Model," *Journal of Sound and Vibration,* vol. 107, no. 2, pp. 181-194, June 1986.

[6] P. Kindt, P. Sas and W. Desmet, "Development and Validation of a Three-Dimensional Ring-Based Structural Tyre Model," *Journal of Sound and Vibration,* vol. 326, no. 3-5, pp. 852-869, October 2009.

[7] W. Soedel and M. G. Prasad, "Calculation of Natural Frequencies and Modes of Tires in Road Contact by Utilizing Eigenvalues of the Axisymmetric Non-Contacting Tire," *Journal of Sound and Vibration,* vol. 70, no. 4, pp. 573-584, June 1980.

[8] S. C. Huang and W. Soedel, "Effects of Coriolis Acceleration on the Free and Forced In-Plane Vibrations of Rotating Rings on Elastic Foundation," *Journal of Sound and Vibration,* vol. 115, no. 2, pp. 253-274, June 1987.

[9] H. B. Pacejka, Tyre and Vehicle Dynamics, 2nd ed., Burlington: Butterworth-Heinemann, 2006.

[10] E. Velenis, P. Tsiotras, C. Canudas-de-Wit and M. Sorine, "Dynamic Tire Friction Models for Combined Longitudinal and Lateral Vehicle Motion," *Vehicle System Dynamics,* vol. 43, no. 1, pp. 3-29, January 2005.

[11] G. H. Gim and P. E. Nikravesh, "An Analytic Model of Pneumatic Tires for Vehicle Dynamic Simulations," *International Journal of Vehicle Design,* Vols. 11-12, no. 6, 1-2, 1990-1991.

[12] B. M. Shifrin, "An Analytical Model of a Rolling Pneumatic Tire," *International Applied Mechanics,* vol. 42, no. 4, pp. 479-485, August 2006.

[13] P. S. Grover, "Modeling of Rolling Resistance Test Data," *SAE Technical Papers,* February 1998, doi: 10.4271/980251.

[14] L. Nielsen and T. Sandberg, "A New Model for Rolling Resistance of Pneumatic Tires," *SAE Technical Papers,* March 2002, doi:10.4271/2002-01-1200.

[15] D. E. Hall and J. C. Moreland, "Fundamentals of Rolling Resistance," *Rubber Chemistry and Technology,* vol. 74, no. 3, pp. 525-539, July 2001.

[16] J. F. Sinnamon and J. T. Tielking, "Hydroplaning and Tread Pattern Hydrodynamics," Ann Arbor, Michigan, 1974.

[17] C. W. Oh, T. W. Kim, H. Y. Jeong, K. S. Park and S. N. Kim, "Hydroplaning Simulation for a Straight-Grooved Tire by Using FDM, FEM and an Asymptotic Method," *Journal of Mechanical Science and Technology,* vol. 22, no. 1, pp. 34-40, April 2008.

[18] E. Seta, Y. Nakajima, T. Kamegawa and H. Ogawa, "Hydroplaning Analysis by FEM and FVM: Effect of Tire Rolling and Tire Pattern on Hydroplaning," *Tire Science and Technology,* vol. 28, no. 3, pp. 140-156, July 2000.

[19] F. Koutný, Geometry and Mechanics of Pneumatic Tires, Zlín, 1997.

[20] T. B. Rhyne, "Development of a Verticle Stiffness Relationship for Belted Radial Tires," *Tire Science and Technology,* vol. 33, no. 3, pp. 136-155, 20 July-September 2005.

[21] S. K. Clark, "The Rolling Tire Under Load," *SAE Technical Paper,* February 1965, doi: 10.4271/650493.

[22] A. Gasmi, P. F. Joseph, T. B. Rhyne and S. M. Cron, "Closed-Form Solution of a Shear Deformable, Extensional Ring in Contact Between Two Rigid Surfaces," *International Journal of Solids and Structures,* vol. 48, no. 5, p. 843–853, March 2011.

[23] A. Gasmi, P. F. Joseph, T. B. Rhyne and S. M. Cron, "Development of a Two-Dimensional Model of a Compliant Non-Pneumatic Tire," *International Journal of Solids and Structures,* 2012.

[24] C. B. Bucknall, "Applications of Microscopy to the Deformation and Fracture of Rubber-Toughened Polymers," *Journal of Microscopy,* vol. 201, no. 2, pp. 221-229, February 2001.

[25] T. B. Rhyne and S. M. Cron, "Development of a Non-Pneumatic Wheel," *Tire Science and Technology,* vol. 34, no. 3, pp. 150-169, July 2006.

[26] T.-s. Song, J.-W. Lee and H.-J. Yu, "Rolling Resistance of Tires - An Analysis of Heat," *SAE Technical Papers,* February 1998, doi:10.4271/980255.

CHAPTER 2
–
THEORETICAL DEVELOPMENT

2.1. Sidewall Characterization

The model of the non-pneumatic tire developed by Gasmi represented the tire with a ring supported by spokes that buckled under a compressive load and did not produce a circumferential load in response to rotation. These assumptions were valid for the particular non-pneumatic tire being studied, but they are not valid for a pneumatic tire. Therefore, in order to determine how the sidewall should be modeled, its behavior in the radial and circumferential directions is described below.

2.1.1. Sidewall Behavior in the Radial Direction

The key to understanding the behavior of the sidewall in the radial direction is to know its shape before and after deformation. Koutný showed that the inflated shape of the tire can be accurately calculated based on inextensible membrane assumptions [1]. Therefore, in order to gain a general understanding of the behavior of the sidewall in the radial direction, the shape of the sidewall is approximated as an inextensible membrane that is fully described by either R and θ or L and W, as defined in the figure below.

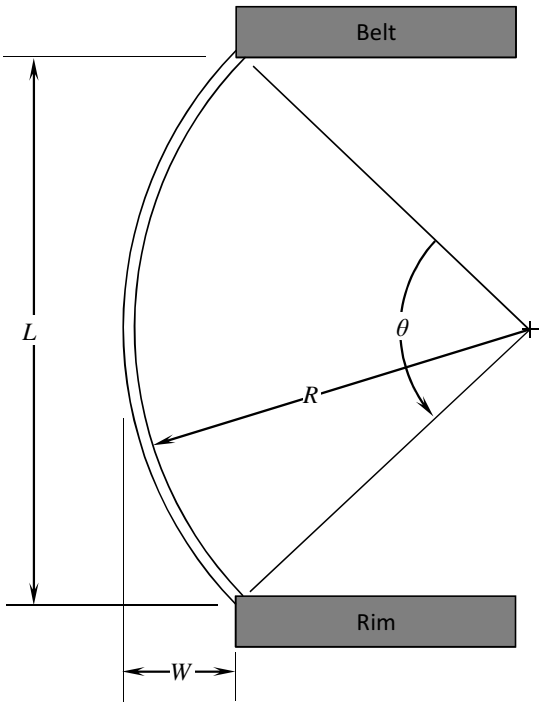

Figure 2.1. Tire sidewall dimensions

Assuming that the cords in the carcass are inextensible results in the following relationship that must be enforced:

$$\theta_0 R_0 = \theta_1 R_1 \tag{2.1.1}$$

where the subscripts represent dimensions in the original (0) and deformed (1) positions. Geometry of a circular segment gives expressions for R and θ in terms of L and W as

$$\begin{aligned} R &= \frac{L^2 + 4W^2}{8W} \\ \theta &= 2\cos^{-1}\left(\frac{L^2 - 4W^2}{L^2 + 4W^2}\right) \end{aligned} \tag{2.1.2}$$

Since only the radial stiffness of the sidewall is being considered here, it is reasonable to assume that the ends of the sidewall cords remain aligned before and after deformation (radial

deformation for the tire being in the vertical direction for Figure 2.1). Additionally, the following relationship is known:

$$L_1 = L_0 + u_r - u_{r0} \tag{2.1.3}$$

where $u_r - u_{r0}$ is the known radial deformation of the tire's belt from its inflated position.

The deformed width, W_1, that preserves the sidewall length is unknown and is therefore related to the original width W_0 by

$$W_1 = W_0 + \Delta W \tag{2.1.4}$$

Substituting the known relationships into (2.1.1) gives

$$\begin{aligned} &\frac{L_0^{\,2} + 4W_0^{\,2}}{W_0} \cos^{-1}\left(\frac{L_0^{\,2} - 4W_0^{\,2}}{L_0^{\,2} + 4W_0^{\,2}}\right) \\ &\quad = \frac{\left(L_0 + u_r - u_{r0}\right)^2 + 4\left(W_0 + \Delta W\right)^2}{\left(W_0 + \Delta W\right)} \cos^{-1}\left(\frac{\left(L_0 + u_r - u_{r0}\right)^2 - 4\left(W_0 + \Delta W\right)^2}{\left(L_0 + u_r - u_{r0}\right)^2 + 4\left(W_0 + \Delta W\right)^2}\right) \end{aligned} \tag{2.1.5}$$

The equation (2.1.5) is one equation in the single unknown, ΔW, which can be easily solved for using a non-linear equation solver.

Since circumferential tension in a pressurized membrane can be approximated to be

$$T = P R_1 \tag{2.1.6}$$

and the radial load (i.e. the vertical load in Figure 2.1) exerted by the sidewall on the tire's belts can be written as

$$q_r b = -T \cos\left(\frac{\theta_1}{2}\right) \tag{2.1.7}$$

where b is the width of the tire, a numerical relationship between the radial load and the radial deformation can be obtained.

A reference tire's dimensions are known to be

$$L = 90\,\text{mm}$$
$$W = 20\,\text{mm} \tag{2.1.8}$$

Using these inputs, the normalized radial load can be plotted as a function of radial displacement as shown in Figure 2.2.

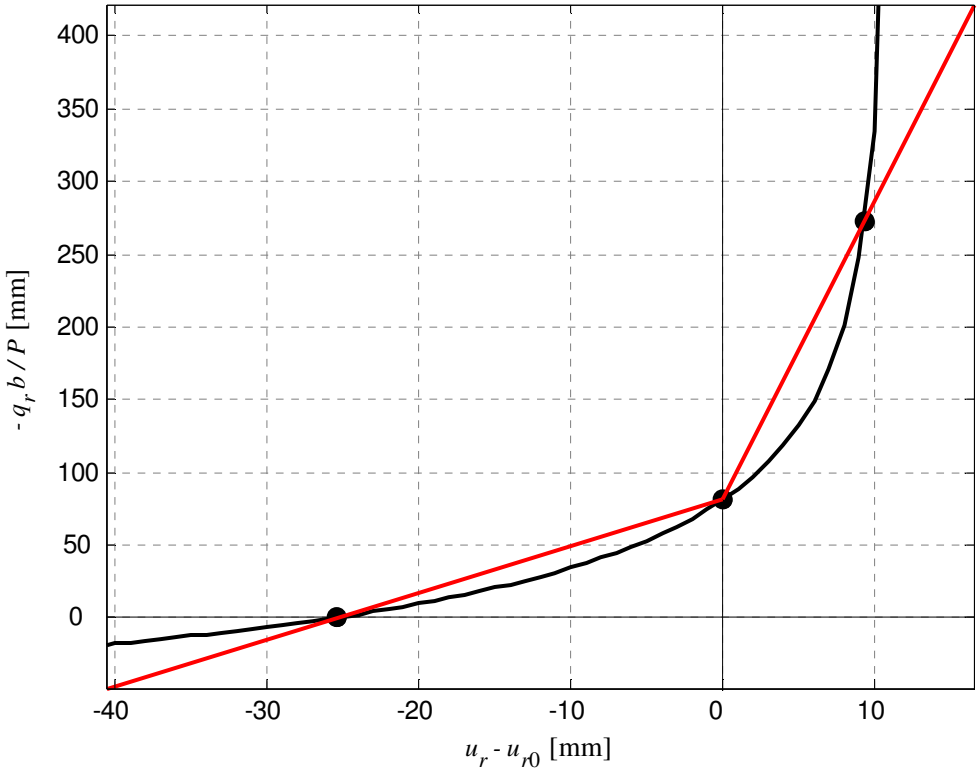

Figure 2.2. Membrane force vs. displacement

First, it should be noted from the figure above that the significance of the load crossing the horizontal axis is that this is where the top of the sidewall is parallel to the belts. Because of the assumptions made here, this occurs when $L = 2\ W$ (i.e. when the sidewall is in the shape of a half-circle).

From this plot, it is quite apparent that radial sidewall stiffness can be modeled adequately by a bi-linear spring. That is to say, the difference in accuracy between a linear and bi-linear spring would be significant due to the sidewall being significantly stiffer in tension than in compression. Furthermore, it is noteworthy that there is a non-zero positive load at zero displacement, indicating that pressurizing the sidewall causes the sidewall cords to be in tension and places a non-zero load on the belts. These two observations imply that the load on the belts due to the sidewall can be approximated with (2.1.9).

$$q_r = \begin{cases} -\dfrac{K_r^{\,T} u_r}{b}, & u_r > u_{r0} \\ -\dfrac{F_P}{b}, & u_r = u_{r0} \\ -\dfrac{K_r^{\,C} u_r}{b}, & u_r < u_{r0} \end{cases} \tag{2.1.9}$$

where F_P is the tension in the cords produced as a result of inflation pressure, $K_r^{\,T}$ is the stiffness of the sidewall in tension, and $K_r^{\,C}$ is the stiffness of the sidewall in compression.

Using $F_P = F_P^{\,*} + K_r^{\,C} u_{r0}$, (2.1.9) could also be written as

$$q_r = \begin{cases} -\dfrac{F_P^{\,*}}{b} - \dfrac{K_r^{\,T} u_r}{b}, & u_r > u_{r0} \\ -\dfrac{F_P^{\,*}}{b} - \dfrac{K_r^{\,C} u_r}{b}, & u_r \le u_{r0} \end{cases} \tag{2.1.10}$$

The difference between the two definitions is that in (2.1.9), F_P / P is the normalized radial load of the inflated sidewall at $u_r - u_{r0} = 0$ (i.e. the inflated position), and $F_P^{\,*} / P$ is the normalized radial load of the inflated sidewall at $u_r - u_{r0} = -u_{r0}$ (i.e. the uninflated position). Therefore, due to the tension in the sidewall created by inflation pressure, the pressure that

must be applied to the outside of the tire to compress the tire back to its uninflated radius is given by (2.1.11).

$$q_r = P - \frac{F_P^*}{b} \tag{2.1.11}$$

In fact, this is the effective inflation pressure seen by the belts of the tire.

2.1.2. Sidewall Behavior in the Circumferential Direction

The stiffness of the sidewall in the circumferential direction is due to two different parts of the tire. At 2 bar, the amount of torque required to rotate the belts of a normal tire a specific amount is slightly less than twice as much as is required in a deflated tire. This indicates that at 2 bar, approximately half of the circumferential stiffness is due to the tire's structure and half is due to membrane effects resulting from the inflation pressure.

Knowing that the sidewall is composed of nearly inextensible radial cords surrounded by rubber, the structural aspect of this stiffness is clearly due to the rubber between these cords resisting deformation. The effect of the inflation pressure on the stiffness is caused by a component of the cord tension becoming tangential to the belts after they are rotated. This effect can be calculated as explained below.

The spring equation in (2.1.12) describes the inflated tire's sidewall

$$\begin{Bmatrix} q_r \\ q_\theta \end{Bmatrix} = -\frac{1}{b}\begin{Bmatrix} F_P \\ 0 \end{Bmatrix} - \frac{1}{b}\begin{bmatrix} 0 & 0 \\ 0 & K_\theta \end{bmatrix}\begin{Bmatrix} u_{r0} \\ u_{\theta 0} \end{Bmatrix} \tag{2.1.12}$$

This spring equation can be expanded to obtain the expressions for q_r and q_θ.

$$\begin{aligned} q_r &= -\frac{F_P}{b} \\ q_\theta &= -\frac{K_\theta u_{\theta 0}}{b} \end{aligned} \tag{2.1.13}$$

It is important to determine the dependence of K_θ on inflation pressure. This effect is because as the belts rotate, the radial load becomes de-radialized and a component of it acts in the circumferential direction. The changes in the circumferential components of the tension in the cords will give rise to the dependence of K_θ on inflation pressure.

In order to obtain a better understanding of what is physically occurring in the tire's deformation, the belt and carcass structure are visualized using the following figure, where the "Undeformed" position is the position after inflation.

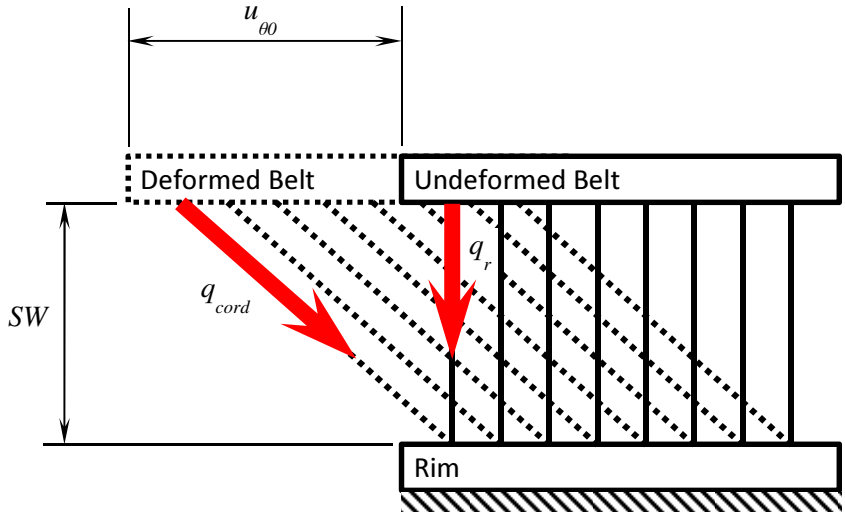

Figure 2.3. The de-radialization of the radial load produces a circumferential load

When the belts of the tire rotate, the distance between the two ends of the cords increases, thereby increasing their tension. Therefore, q_{cord} is given as

$$q_{cord} = -\frac{K_r^{\ T}}{b}\Delta SW - \frac{F_P}{b} \tag{2.1.14}$$

The change in the distance between the two ends of a cord, ΔSW, can be calculated using trigonometry to be

$$\Delta SW = \sqrt{{u_{\theta 0}}^2 + SW^2} - SW \tag{2.1.15}$$

Substituting (2.1.15) into (2.1.14) gives

$$q_{cord} = -\frac{{K_r}^T}{b}\left(\sqrt{{u_{\theta 0}}^2 + SW^2} - SW\right) - \frac{F_P}{b} \tag{2.1.16}$$

The radial and circumferential components of this load are

$$\begin{aligned} q_r' &= q_{cord}\frac{SW}{\sqrt{{u_{\theta 0}}^2 + SW^2}} \\ q_\theta &= q_{cord}\frac{u_{\theta 0}}{\sqrt{{u_{\theta 0}}^2 + SW^2}} \end{aligned} \tag{2.1.17}$$

where the prime notation on q_r distinguishes the load after deformation from the load before deformation. Substituting (2.1.16) gives

$$\begin{aligned} q_r' &= -\frac{{K_r}^T SW}{b}\left(\frac{\sqrt{{u_{\theta 0}}^2 + SW^2} - SW}{\sqrt{{u_{\theta 0}}^2 + SW^2}}\right) - \frac{F_P}{b}\frac{SW}{\sqrt{{u_{\theta 0}}^2 + SW^2}} \\ q_\theta &= -\frac{{K_r}^T u_{\theta 0}}{b}\left(\frac{\sqrt{{u_{\theta 0}}^2 + SW^2} - SW}{\sqrt{{u_{\theta 0}}^2 + SW^2}}\right) - \frac{F_P}{b}\frac{u_{\theta 0}}{\sqrt{{u_{\theta 0}}^2 + SW^2}} \end{aligned} \tag{2.1.18}$$

For small values of $u_{\theta 0}$ (i.e. $u_{\theta 0} << SW$), the leading order terms of (2.1.18) can be expressed as

$$\begin{aligned} q_r' = q_r &= -\frac{F_P}{b} + \left(\frac{F_P - {K_r}^T SW}{SW^2}\right)\frac{{u_{\theta 0}}^2}{2b} + O\left({u_{\theta 0}}^4\right) \\ q_\theta &= q_r\frac{u_{\theta 0}}{SW} = -\left(\frac{F_P}{SW}\right)\frac{u_{\theta 0}}{b} + O\left({u_{\theta 0}}^3\right) \end{aligned} \tag{2.1.19}$$

This reveals two things. First, q_r depends on the square of $u_{\theta 0}$, so that within a linear context, there is no variation of the radial load in response to circumferential deformation. Second, since the radial stiffness is predominantly due to the inflation pressure, the inflation pressure influences the circumferential load to first order in $u_{\theta 0}$, which requires K_θ to be

proportional to the pressure. Since the circumferential stiffness is already known to include a significant structural component, this is equivalent to having the torsional stiffness,

$$K_\theta = C\,P + D \tag{2.1.20}$$

where C is known to be given by

$$C = \frac{F_P}{P\,SW} \tag{2.1.21}$$

Equation (2.1.22) relates a torque, T, and the resulting rotation, $u_{\theta 0}$, to the circumferential stiffness, K_θ.

$$K_\theta = \frac{T}{2\pi R^2 u_{\theta 0}} \tag{2.1.22}$$

Therefore, having access to experimental data relating an applied torque to the circumferential rotation at various inflation pressures and knowing the physical dimensions of the tire, one can easily calculate the value of F_P.

2.1.3. Summary

A summary of the applied loads for the pneumatic and non-pneumatic tire is shown in Table 2.1 with the regions defined as in Figure 2.4. The angle θ_L is the angle between the center and the edge of contact, and the angle θ_S is the angle between the center of contact and the location where the radial deformation of the belts from the inflated position switches from negative to positive.

Table 2.1. Comparison of pneumatic and non-pneumatic tire loads

Region	Non-Pneumatic Tire	Pneumatic Tire
$\theta \le \theta_L$	$\begin{Bmatrix} q_r \\ q_\theta \end{Bmatrix} = \begin{Bmatrix} q_{gr} \\ q_{g\theta} \end{Bmatrix}$	$\begin{Bmatrix} q_r \\ q_\theta \end{Bmatrix} = \begin{Bmatrix} q_{gr} + P \\ q_{g\theta} \end{Bmatrix} - \frac{1}{b}\begin{bmatrix} K_r{}^C & 0 \\ 0 & K_\theta \end{bmatrix}\begin{Bmatrix} u_r \\ u_{\theta 0} \end{Bmatrix}$
$\theta_L \le \theta \le \theta_S$	$\begin{Bmatrix} q_r \\ q_\theta \end{Bmatrix} = \begin{Bmatrix} 0 \\ 0 \end{Bmatrix}$	$\begin{Bmatrix} q_r \\ q_\theta \end{Bmatrix} = \begin{Bmatrix} P \\ 0 \end{Bmatrix} - \frac{1}{b}\begin{bmatrix} K_r{}^C & 0 \\ 0 & K_\theta \end{bmatrix}\begin{Bmatrix} u_r \\ u_{\theta 0} \end{Bmatrix}$
$\theta = \theta_S$	$\begin{Bmatrix} q_r \\ q_\theta \end{Bmatrix} = \begin{Bmatrix} 0 \\ 0 \end{Bmatrix}$	$\begin{Bmatrix} q_r \\ q_\theta \end{Bmatrix} = \begin{Bmatrix} P \\ 0 \end{Bmatrix} - \frac{1}{b}\begin{Bmatrix} F_P \\ 0 \end{Bmatrix}$
$\theta_S \le \theta$	$\begin{Bmatrix} q_r \\ q_\theta \end{Bmatrix} = -\frac{1}{b}\begin{bmatrix} K_r & 0 \\ 0 & 0 \end{bmatrix}\begin{Bmatrix} u_r \\ u_{\theta 0} \end{Bmatrix}$	$\begin{Bmatrix} q_r \\ q_\theta \end{Bmatrix} = \begin{Bmatrix} P \\ 0 \end{Bmatrix} - \frac{1}{b}\begin{bmatrix} K_r{}^T & 0 \\ 0 & K_\theta \end{bmatrix}\begin{Bmatrix} u_r \\ u_{\theta 0} \end{Bmatrix}$

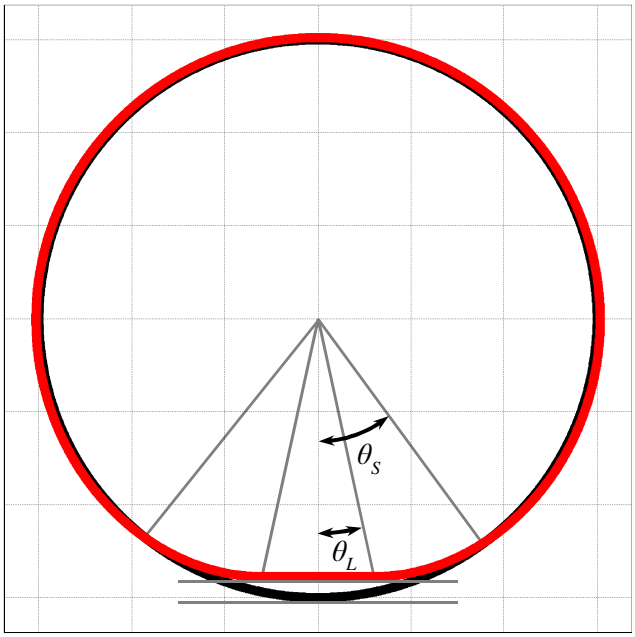

Figure 2.4. Regions defined in the pneumatic and non-pneumatic tire

2.2. Governing Differential Equations

In order to understand how applied loads deform the tire, the governing differential equations are developed by using Timoshenko beam theory to model the belt. This section follows Gasmi, et al. [2]. According to Timoshenko, the cross-section of a deformed beam can be approximated by a rotation from its original position, with shear correction factors used to compensate for the approximation. From this, equations describing the displacement field can be derived. First, it is assumed that the radial deformation of the ring, which is constant throughout the thickness of the ring, depends only on θ. Second, because cross-sections may rotate, it is assumed that the circumferential deformation changes linearly through the thickness of the ring. These assumptions result in deformations similar to those shown in Figure 2.5.

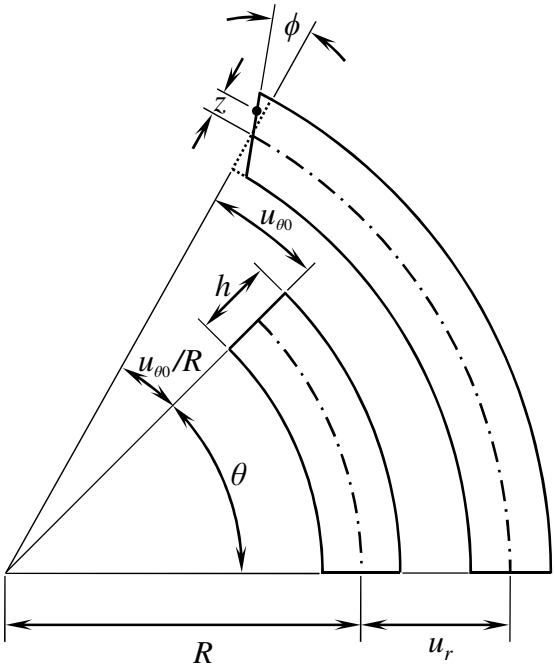

Figure 2.5. Depiction of deformations

Therefore, the radial and circumferential deformations can be written as

$$\begin{aligned} u_r(r,\theta) &= u_r(R,\theta) = u_r(\theta) \\ u_\theta(r,\theta) &= u_{\theta 0}(\theta) + z\phi(\theta) \end{aligned} \tag{2.2.1}$$

The standard expressions for strain in polar coordinates are

$$\begin{aligned} \varepsilon_{rr} &= \frac{\partial u_r}{\partial r} \\ \varepsilon_{\theta\theta} &= \frac{1}{r}\frac{\partial u_\theta}{\partial \theta} + \frac{u_r}{r} \\ \gamma_{r\theta} &= 2\varepsilon_{r\theta} = \frac{1}{r}\frac{\partial u_r}{\partial \theta} + \frac{\partial u_\theta}{\partial r} - \frac{u_\theta}{r} \end{aligned} \tag{2.2.2}$$

Substituting (2.2.1) into (2.2.2) and knowing that $z = r - R$ allows the strain to be written as

$$\begin{aligned} \varepsilon_{rr} &= 0 \\ \varepsilon_{\theta\theta} &= \frac{1}{R+z}\left(\frac{du_{\theta 0}}{d\theta} + u_r + z\frac{d\phi}{d\theta}\right) \\ \gamma_{r\theta} &= \frac{1}{R+z}\left(\frac{du_r}{d\theta} - u_{\theta 0} + R\phi\right) \end{aligned} \tag{2.2.3}$$

Assuming plane stress and linear, elastic material behavior, the constitutive relations are

$$\begin{aligned} \sigma_{\theta\theta} &= E\varepsilon_{\theta\theta} \\ \tau_{r\theta} &= G\gamma_{r\theta} \end{aligned} \tag{2.2.4}$$

Substituting (2.2.3) into (2.2.4) gives expressions for the stress in terms of the deformations.

$$\begin{aligned} \sigma_{\theta\theta} &= \frac{E}{R+z}\left(\frac{du_{\theta 0}}{d\theta} + u_r + z\frac{d\phi}{d\theta}\right) \\ \tau_{r\theta} &= \frac{G}{R+z}\left(\frac{du_r}{d\theta} - u_{\theta 0} + R\phi\right) \end{aligned} \tag{2.2.5}$$

The virtual strain energy of a deformed material is

$$\delta U = \int_{\Omega} \left(\sigma_{\theta\theta} \delta \varepsilon_{\theta\theta} + \tau_{r\theta} \delta \gamma_{r\theta} \right) d\Omega \tag{2.2.6}$$

Substituting (2.2.3) and (2.2.5) into (2.2.6)

$$\delta U = \int_{\Omega} \left(\begin{array}{l} \dfrac{E}{(R+z)^2} \left(\dfrac{du_{\theta 0}}{d\theta} + u_r + z \dfrac{d\phi}{d\theta} \right) \left(\dfrac{d\delta u_{\theta 0}}{d\theta} + \delta u_r + z \dfrac{d\delta\phi}{d\theta} \right) \\ + \dfrac{G}{(R+z)^2} \left(\dfrac{du_r}{d\theta} - u_{\theta 0} + R\phi \right) \left(\dfrac{d\delta u_r}{d\theta} - \delta u_{\theta 0} + R\delta\phi \right) \end{array} \right) d\Omega \tag{2.2.7}$$

Collecting the virtual displacements in (2.2.7)

$$\delta U = \int_{\Omega} \left(\frac{1}{(R+z)^2} \left(\begin{array}{l} G \left(\dfrac{du_r}{d\theta} - u_{\theta 0} + R\phi \right) \dfrac{d\delta u_r}{d\theta} + E \left(\dfrac{du_{\theta 0}}{d\theta} + u_r + z \dfrac{d\phi}{d\theta} \right) \delta u_r \\ + E \left(\dfrac{du_{\theta 0}}{d\theta} + u_r + z \dfrac{d\phi}{d\theta} \right) \dfrac{d\delta u_{\theta 0}}{d\theta} - G \left(\dfrac{du_r}{d\theta} - u_{\theta 0} + R\phi \right) \delta u_{\theta 0} \\ + E\, z \left(\dfrac{du_{\theta 0}}{d\theta} + u_r + z \dfrac{d\phi}{d\theta} \right) \dfrac{d\delta\phi}{d\theta} + G\, R \left(\dfrac{du_r}{d\theta} - u_{\theta 0} + R\phi \right) \delta\phi \end{array} \right) \right) d\Omega \tag{2.2.8}$$

The integral in (2.2.8) can be broken up into the double integral over the cross-sectional area, and over a piece of the ring from θ_1 to θ_2, as shown in (2.2.9).

$$\delta U = \int_{\theta_1}^{\theta_2} \int_A \frac{1}{(R+z)^2} \left(\begin{array}{l} G \left(\dfrac{du_r}{d\theta} - u_{\theta 0} + R\phi \right) \dfrac{d\delta u_r}{d\theta} + E \left(\dfrac{du_{\theta 0}}{d\theta} + u_r + z \dfrac{d\phi}{d\theta} \right) \delta u_r \\ + E \left(\dfrac{du_{\theta 0}}{d\theta} + u_r + z \dfrac{d\phi}{d\theta} \right) \dfrac{d\delta u_{\theta 0}}{d\theta} - G \left(\dfrac{du_r}{d\theta} - u_{\theta 0} + R\phi \right) \delta u_{\theta 0} \\ + E\, z \left(\dfrac{du_{\theta 0}}{d\theta} + u_r + z \dfrac{d\phi}{d\theta} \right) \dfrac{d\delta\phi}{d\theta} + G\, R \left(\dfrac{du_r}{d\theta} - u_{\theta 0} + R\phi \right) \delta\phi \end{array} \right) r\, dA\, d\theta \tag{2.2.9}$$

Using the relationship between *r*, *R*, and z, and distributing the area integral to all the terms gives (2.2.10).

$$\delta U = \int_{\theta_1}^{\theta_2} \left(\begin{array}{l} \left(\int_A \frac{G}{R+z} \frac{du_r}{d\theta} dA - \int_A \frac{G}{R+z} u_{\theta 0}\, dA + \int_A \frac{G\,R}{R+z} \phi\, dA \right) \frac{d\,\delta u_r}{d\theta} \\ \quad + \left(\int_A \frac{E}{R+z} \frac{du_{\theta 0}}{d\theta} dA + \int_A \frac{E}{R+z} u_r\, dA + \int_A \frac{E\,z}{R+z} \frac{d\phi}{d\theta} dA \right) \delta u_r \\ \quad + \left(\int_A \frac{E}{R+z} \frac{du_{\theta 0}}{d\theta} dA + \int_A \frac{E}{R+z} u_r\, dA + \int_A \frac{E\,z}{R+z} \frac{d\phi}{d\theta} dA \right) \frac{d\,\delta u_{\theta 0}}{d\theta} \\ \quad - \left(\int_A \frac{G}{R+z} \frac{du_r}{d\theta} dA - \int_A \frac{G}{R+z} u_{\theta 0}\, dA + \int_A \frac{G\,R}{R+z} \phi\, dA \right) \delta u_{\theta 0} \\ \quad + \left(\int_A \frac{E\,z}{R+z} \frac{du_{\theta 0}}{d\theta} dA + \int_A \frac{E\,z}{R+z} u_r\, dA + \int_A \frac{E\,z^2}{R+z} \frac{d\phi}{d\theta} dA \right) \frac{d\,\delta\phi}{d\theta} \\ \quad + \left(\int_A \frac{G\,R}{R+z} \frac{du_r}{d\theta} dA - \int_A \frac{G\,R}{R+z} u_{\theta 0}\, dA + \int_A \frac{G\,R^2}{R+z} \phi\, dA \right) \delta\phi \end{array} \right) d\theta \tag{2.2.10}$$

If the Young's modulus, E, and the cross-section are assumed symmetric about the centroid, the terms with the first power of z go to zero. Furthermore, assuming that R is much greater than z, allows (2.2.10) to be simplified to (2.2.11).

$$\delta U = \int_{\theta_1}^{\theta_2} \frac{1}{R} \left(\begin{array}{l} \left(GA \frac{du_r}{d\theta} - GA\, u_{\theta 0} + R\, GA\, \phi \right) \frac{d\,\delta u_r}{d\theta} + \left(EA \frac{du_{\theta 0}}{d\theta} + EA\, u_r \right) \delta u_r \\ \quad + \left(EA \frac{du_{\theta 0}}{d\theta} + EA\, u_r \right) \frac{d\,\delta u_{\theta 0}}{d\theta} - \left(GA \frac{du_r}{d\theta} - GA\, u_{\theta 0} + R\, GA\, \phi \right) \delta u_{\theta 0} \\ \quad + EI \frac{d\phi}{d\theta} \frac{d\,\delta\phi}{d\theta} + \left(R\, GA \frac{du_r}{d\theta} - R\, GA\, u_{\theta 0} + R^2\, GA\, \phi \right) \delta\phi \end{array} \right) d\theta \tag{2.2.11}$$

In the above expression, EA, EI, and GA for a general cross-section are defined by

$$\begin{aligned} EA &= \int_A E\, dA \\ EI &= \int_A E\, z^2\, dA \\ GA &= \int_A G\, dA \end{aligned} \tag{2.2.12}$$

Integration by parts of (2.2.11) removes the derivatives from terms with the variations of the displacements in them.

$$\delta U = \int_{\theta_1}^{\theta_2} \frac{1}{R} \left(\begin{array}{l} \left(-GA\frac{d^2u_r}{d\theta^2} + EA\,u_r + (GA+EA)\frac{du_{\theta 0}}{d\theta} - RGA\frac{d\phi}{d\theta} \right)\delta u_r \\ \quad + \left(-EA\frac{d^2u_{\theta 0}}{d\theta^2} + GA\,u_{\theta 0} - (EA+GA)\frac{du_r}{d\theta} - RGA\,\phi \right)\delta u_{\theta 0} \\ \quad + \left(-EI\frac{d^2\phi}{d\theta^2} + R^2\,GA\,\phi + RGA\frac{du_r}{d\theta} - RGA\,u_{\theta 0} \right)\delta\phi \end{array} \right) d\theta \\ + \frac{1}{R}\left[GA\left(\frac{du_r}{d\theta} - u_{\theta 0} + R\phi \right)\delta u_r + EA\left(\frac{du_{\theta 0}}{d\theta} + u_r \right)\delta u_{\theta 0} + EI\frac{d\phi}{d\theta}\delta\phi \right]_{\theta_1}^{\theta_2} \tag{2.2.13}$$

The virtual potential energy for a ring when loaded with arbitrary distributed loads of $q_r(\theta)$ in the radial direction and $q_\theta(\theta)$ in the circumferential direction is

$$\delta V = -\int_{\theta_1}^{\theta_2} \left(q_r\,\delta u_r + q_\theta\,\delta u_{\theta 0} \right) R\,b\,d\theta \tag{2.2.14}$$

When in equilibrium, the virtual work of a deformable elastic continuum is equal to zero, i.e.,

$$\delta W = \delta U + \delta V = 0 \tag{2.2.15}$$

Substituting (2.2.13) and (2.2.14) into (2.2.15) gives (2.2.16).

$$0 = \int_{\theta_1}^{\theta_2} \frac{1}{R} \left(\begin{array}{l} \left(-GA\frac{d^2u_r}{d\theta^2} + EA\,u_r + (GA+EA)\frac{du_{\theta 0}}{d\theta} - RGA\frac{d\phi}{d\theta} - R^2\,b\,q_r \right)\delta u_r \\ \quad + \left(-EA\frac{d^2u_{\theta 0}}{d\theta^2} + GA\,u_{\theta 0} - (EA+GA)\frac{du_r}{d\theta} - RGA\,\phi - R^2\,b\,q_\theta \right)\delta u_{\theta 0} \\ \quad + \left(-EI\frac{d^2\phi}{d\theta^2} + R^2\,GA\,\phi + RGA\frac{du_r}{d\theta} - RGA\,u_{\theta 0} \right)\delta\phi \end{array} \right) d\theta \\ + \frac{1}{R}\left[GA\left(\frac{du_r}{d\theta} - u_{\theta 0} + R\phi \right)\delta u_r + EA\left(\frac{du_{\theta 0}}{d\theta} + u_r \right)\delta u_{\theta 0} + EI\frac{d\phi}{d\theta}\delta\phi \right]_{\theta_1}^{\theta_2} \tag{2.2.16}$$

The internal forces and moments on a cross-section can be written as

$$
\begin{aligned}
M &= \int_A z\sigma_{\theta\theta} dA \\
N &= \int_A \sigma_{\theta\theta} dA \\
V &= \int_A \tau_{r\theta} dA
\end{aligned}
\tag{2.2.17}
$$

Using the same assumptions as above and (2.2.3) and (2.2.4) allows (2.2.17) to be expressed in terms of displacements.

$$
\begin{aligned}
M &= EI \frac{d\phi}{d\theta} \\
N &= EA\left(\frac{du_{\theta 0}}{d\theta} + u_r \right) \\
V &= \frac{GA}{R}\left(\frac{du_r}{d\theta} - u_{\theta 0} + R\phi \right)
\end{aligned}
\tag{2.2.18}
$$

Therefore, from (2.2.16) and (2.2.18), the governing differential equations for a circular beam can be written as

$$
\begin{aligned}
&EA\frac{d^2 u_{\theta 0}}{d\theta^2} - GAu_{\theta 0} + \left(EA + GA\right)\frac{du_r}{d\theta} + RGA\phi = -R^2 b\, q_\theta \\
&-GA\frac{d^2 u_r}{d\theta^2} + EAu_r + \left(EA + GA\right)\frac{du_{\theta 0}}{d\theta} - RGA\frac{d\phi}{d\theta} = R^2 b\, q_r \\
&EI\frac{d^2\phi}{d\theta^2} - R^2 GA\phi - RGA\frac{du_r}{d\theta} + RGAu_{\theta 0} = 0
\end{aligned}
\tag{2.2.19}
$$

with the boundary conditions

$$
\begin{aligned}
&u_r(\theta_i) \quad , \quad V(\theta_i) = \frac{GA}{R}\left(\frac{du_r}{d\theta} - u_{\theta 0} + R\phi \right)\Bigg|_{\theta_i} , \\
&u_{\theta 0}(\theta_i) \quad , \quad N(\theta_i) = \frac{EA}{R}\left(\frac{du_{\theta 0}}{d\theta} + u_r \right)\Bigg|_{\theta_i} , \\
&\phi\left(\theta_i\right) \quad , \quad M(\theta_i) = \frac{EI}{R}\frac{d\phi}{d\theta}\Bigg|_{\theta_i}
\end{aligned}
\tag{2.2.20}
$$

2.3. Decoupled Differential Equations

Solutions to these three differential equations can be found after decoupling them into three independent differential equations. However, because a pneumatic tire has both radial and circumferential stiffnesses, it is necessary to substitute the spring relationships into the governing differential equations before they are decoupled in order to ensure an accurate fully decoupled result. Therefore, the loads q_r and q_θ are defined as

$$\begin{aligned} q_r &= q_r^* - \frac{K_r u_r}{b} \\ q_\theta &= q_\theta^* - \frac{K_\theta u_{\theta 0}}{b} \end{aligned} \tag{2.3.1}$$

where q_r^* and q_θ^* are arbitrary loads independent of the displacements, and K_r can be the radial stiffness in either stiffness or compression. Note that the notation distinguishing the different stiffnesses in tension and compression for the carcass in the radial direction has been dropped since the stiffness is only discontinuous at θ_S. The governing differential equations then become (2.3.2).

$$\begin{aligned} &EA\frac{d^2u_{\theta 0}}{d\theta^2} - \left(GA + R^2K_\theta\right)u_{\theta 0} + \left(EA + GA\right)\frac{du_r}{d\theta} + RGA\phi = -R^2\, b\, q_\theta^* \\ &-GA\frac{d^2u_r}{d\theta^2} + \left(EA + R^2K_r\right)u_r + \left(EA + GA\right)\frac{du_{\theta 0}}{d\theta} - RGA\frac{d\phi}{d\theta} = R^2\, b\, q_r^* \\ &EI\frac{d^2\phi}{d\theta^2} - R^2GA\phi - RGA\frac{du_r}{d\theta} + RGAu_{\theta 0} = 0 \end{aligned} \tag{2.3.2}$$

Solving the $(2.3.2)_1$ for ϕ and $(2.3.2)_2$ for the derivative of ϕ gives

$$\begin{aligned} \phi &= \frac{1}{R}\left(u_{\theta 0} - \left(1 + \frac{EA}{GA}\right)\frac{du_r}{d\theta}\right) - \frac{EA}{RGA}\frac{d^2u_{\theta 0}}{d\theta^2} - \frac{Rb}{GA}\left(q_\theta^* - \frac{K_\theta u_{\theta 0}}{b}\right) \\ \frac{d\phi}{d\theta} &= -\frac{1}{R}\frac{d^2u_r}{d\theta^2} + \frac{EA + R^2K_r}{RGA}u_r + \frac{EA + GA}{RGA}\frac{du_{\theta 0}}{d\theta} - \frac{Rb}{GA}q_r^* \end{aligned} \tag{2.3.3}$$

After taking the derivative of $(2.3.2)_3$, $(2.3.3)_2$ can be substituted into it, and $(2.3.3)_1$ can be substituted into $(2.3.2)_2$. This leads to

$$\begin{aligned} D_1\left[u_{\theta 0}\right] &= -D_2\left[u_r\right] + R^2\, b\left(q_r^* - \frac{dq_\theta^*}{d\theta}\right) \\ D_3\left[u_{\theta 0}\right] &= D_4\left[u_r\right] + R^2\, b\, EI\frac{d^2 q_r^*}{d\theta^2} - R^4\, b\, GA\, q_r^* \end{aligned} \tag{2.3.4}$$

where the differential operators are

$$\begin{aligned} D_1 &= EA\frac{d^3}{d\theta^3} + \left(EA - R^2\, K_\theta\right)\frac{d}{d\theta} \\ D_2 &= EA\frac{d^2}{d\theta^2} + \left(EA + R^2 K_r\right) \\ D_3 &= EI\left(EA + GA\right)\frac{d^3}{d\theta^3} - R^2\, GA\, EA\frac{d}{d\theta} \\ D_4 &= GA\, EI\frac{d^4}{d\theta^4} - EI\left(EA + R^2 K_r\right)\frac{d^2}{d\theta^2} + R^2\, GA\left(EA + R^2 K_r\right) \end{aligned} \tag{2.3.5}$$

In order to obtain a single equation for u_r,

$$\begin{aligned} D_3\left[D_1\left[u_{\theta 0}\right]\right] &= D_3\left[R^2\, b\left(q_r^* - \frac{dq_\theta^*}{d\theta}\right) - D_2\left[u_r\right]\right] \\ &= D_1\left[D_3\left[u_{\theta 0}\right]\right] = D_1\left[D_4\left[u_r\right] + R^2\, b\, EI\frac{d^2 q_r^*}{d\theta^2} - R^4\, b\, GA\, q_r^*\right] \end{aligned} \tag{2.3.6}$$

Isolating u_r results in the differential equation

$$\left\{D_1 D_4 + D_3 D_2\right\}\left[u_r\right] = R^2\, b\left(D_3\left[q_r^* - \frac{dq_\theta^*}{d\theta}\right] - D_1\left[EI\frac{d^2 q_r^*}{d\theta^2} - R^2\, GA\, q_r^*\right]\right) \tag{2.3.7}$$

In expanded form this becomes (2.3.8).

$$\frac{d^6 u_r}{d\theta^6} + d_4\frac{d^4 u_r}{d\theta^4} + d_2\frac{d^2 u_r}{d\theta^2} + d_0 u_r = f + C \tag{2.3.8}$$

where d_0, d_2, d_4, and f are given by (2.3.9).

$$
\begin{aligned}
d_0 &= -\left(1+\frac{R^2\,K_r}{EA}\right)\frac{R^4\,K_\theta}{EI} \\
d_2 &= \left(1+\frac{R^2\,K_\theta}{GA}\right)\left(1+\frac{R^2\,K_r}{EA}\right)+\frac{R^4\,K_r}{EI} \\
d_4 &= 2-R^2\left(\frac{K_r}{GA}+\frac{K_\theta}{EA}\right) \\
f &= -\frac{R^2\,b}{GA}\frac{d^4q_r^*}{d\theta^4}+R^2\,b\left(\frac{R^2EI\,K_\theta+EI\,GA+R^2\,EAGA}{EA\,EI\,GA}\right)\frac{d^2q_r^*}{d\theta^2}-\frac{R^6\,b\,K_\theta\,q_r^*}{EA\,EI} \\
&\qquad -R^2\,b\left(\frac{EA+GA}{GA\,EA}\right)\frac{d^3q_\theta^*}{d\theta^3}+\frac{R^4\,b}{EI}\frac{dq_\theta^*}{d\theta}
\end{aligned}
\tag{2.3.9}
$$

The integration constant, C in (2.3.8), is due to integrating both sides to reduce the overall order of the differential equation. However, note that in order to obtain $(2.3.4)_2$, the derivative of $(2.3.2)_3$ was taken arbitrarily. While this made it possible to decouple the differential equations, it also added a non-physical degree of freedom to the system. Therefore, when C is carried through to the solution and substituted back into the coupled differential equations, it is observed that C must be zero for the equations to be satisfied.

To obtain the simplest possible equation for $u_{\theta 0}$, (2.3.4) are combined to eliminate the higher order derivatives in D_1 and D_3.

$$
\begin{aligned}
\frac{du_{\theta 0}}{d\theta} &= -Q_1\left(\frac{d^4u_r}{d\theta^4}+\frac{d^2u_r}{d\theta^2}\right)-Q_2EA\,u_r+Q_2R^2\,b\left(\frac{K_ru_r}{b}+q_r^*\right) \\
&\qquad -Q_1\frac{R^2\,b}{GA}\frac{d^2}{d\theta^2}\left(\frac{K_ru_r}{b}+q_r^*\right)-Q_1\frac{R^2\,b\left(EA+GA\right)}{EA\,GA}\frac{dq_\theta^*}{d\theta}
\end{aligned}
\tag{2.3.10}
$$

where Q_1 and Q_2 are

$$
\begin{aligned}
Q_1 &= \frac{EA\,GA\,EI}{EA\left(EA\,EI+GA\,EI+R^2EA\,GA\right)-\left(EA+GA\right)R^2EI\,K_\theta} \\
Q_2 &= \frac{EA\,EI+GA\,EI+R^2EA\,GA}{EA\left(EA\,EI+GA\,EI+R^2EA\,GA\right)-\left(EA+GA\right)R^2EI\,K_\theta}
\end{aligned}
\tag{2.3.11}
$$

Therefore, the decoupled governing differential equations are (2.3.12).

$$\begin{aligned}
&\frac{d^6u_r}{d\theta^6}+d_4\frac{d^4u_r}{d\theta^4}+d_2\frac{d^2u_r}{d\theta^2}+d_0u_r=f\\
&\frac{du_{\theta 0}}{d\theta}=-Q_1\left(\frac{d^4u_r}{d\theta^4}+\frac{d^2u_r}{d\theta^2}\right)-Q_2\,EA\,u_r+Q_2\,R^2\,b\left(\frac{K_r\,u_r}{b}+q_r^*\right)\\
&\qquad\qquad -Q_1\frac{R^2\,b}{GA}\frac{d^2}{d\theta^2}\left(\frac{K_r\,u_r}{b}+q_r^*\right)-Q_1\frac{R^2\,b\left(EA+GA\right)}{EA\,GA}\frac{dq_\theta^*}{d\theta}\\
&\phi=\frac{1}{R}\left(u_{\theta 0}-\left(1+\frac{EA}{GA}\right)\frac{du_r}{d\theta}\right)-\frac{EA}{RGA}\frac{d^2u_{\theta 0}}{d\theta^2}-\frac{Rb}{GA}\left(q_\theta^*-\frac{K_\theta u_{\theta 0}}{b}\right)
\end{aligned}\tag{2.3.12}$$

2.4. Solution

2.4.1. Inflation Pressure Solution

Because the sidewall springs are defined relative to the inflated position of the tire, u_{r0}, it is important to first derive this solution before obtaining the solution for the loaded tire. Following the loads described in Table 2.1, the particular solution for the inflated tire can be found by using the pressures,

$$\begin{aligned}
&q_r^*\left(\theta\right)=P-\frac{F_P}{b}=P-\frac{F_P^{\,*}}{b}-\frac{K_r^{\,C}\,u_{r0}}{b}\\
&q_\theta^*\left(\theta\right)=0
\end{aligned}\tag{2.4.1}$$

Since setting the radial stiffness equal to zero does not change the decoupled differential equations, the solution may be obtained by directly substituting (2.4.1) into $(2.3.9)_4$ with $K_r=0$. This gives

$$f\left(\theta\right)=-\frac{R^6\,K_\theta\left(Pb-F_P\right)}{EA\,EI}=-\frac{R^6\,K_\theta\left(Pb-F_P^{\,*}-K_r^{\,C}\,u_{r0}\right)}{EA\,EI}\tag{2.4.2}$$

Using the method of undetermined coefficients, the particular solution can be found to be

$$u_{r0} = \frac{R^2\left(Pb - F_P\right)}{EA} = \frac{R^2\left(Pb - F_P^{\,*}\right)}{EA + R^2\,K_r^{\,C}} \tag{2.4.3}$$

2.4.2. Non-Contact Solution in the Tension Support Region

In order to find the homogeneous solution for u_r, the terms $q_r^{\,*}$ and $q_\theta^{\,*}$ are set to zero (which makes f equal to zero) and the trial solution for u_r is used:

$$u_r^{\,T}\left(\theta\right) = e^{\lambda\theta} \tag{2.4.4}$$

Note here that because u_{r0} consists of material properties and applied loads, it is associated with the particular solution. Therefore, substituting (2.4.4) into the governing equation for u_r (i.e. $(2.3.12)_1$) allows the characteristic equation to be written as

$$\lambda^6 + d_4^{\,T}\,\lambda^4 + d_2^{\,T}\,\lambda^2 + d_0^{\,T} = 0 \tag{2.4.5}$$

where the T-superscript denotes that d_4, d_2, and d_0 were calculated using the radial carcass stiffness for when the carcass is in tension. Solving for λ

$$\lambda = \pm\sqrt{\frac{\left(r_1^T - 2d_4^{\,T}\right)^2 + 2d_4^{\,T} r_1^T - 12\,d_2^{\,T}}{6\,r_1^T}}, \quad \pm\sqrt{\frac{\left(12\,d_2^{\,T} - \left(r_1^T + 2d_4^{\,T}\right)^2\right) \pm I\sqrt{3}\left(\left(r_1^T\right)^2 + 12\,d_2^{\,T} - 4\left(d_4^T\right)^2\right)}{12\,r_1^T}} \tag{2.4.6}$$

where $r_1^{\,T}$ is

$$r_1^T = \sqrt[3]{\begin{array}{l} 36d_2^{\,T}d_4^{\,T} - 108\,d_0^{\,T} - 8\left(d_4^T\right)^3 \\ \quad +12\sqrt{12\left(d_2^T\right)^3 - 3\left(d_2^T d_4^T\right)^2 - 54\,d_2^{\,T}\,d_4^{\,T}\,d_0^{\,T} + 81\left(d_0^T\right)^2 + 12d_0^{\,T}\left(d_4^T\right)^3} \end{array}} \tag{2.4.7}$$

Substituting (2.4.6) into (2.4.4) allows the homogeneous solution to be written as

$$
\begin{aligned}
u_r{}^T(\theta) = {} & c_2\, e^{\sqrt{\frac{\left(r_1{}^T - 2d_4{}^T\right)^2 + 2d_4{}^T r_1{}^T - 12\, d_2{}^T}{6\, r_1{}^T}}\theta} \\
& + c_3\, e^{-\sqrt{\frac{\left(r_1{}^T - 2d_4{}^T\right)^2 + 2d_4{}^T r_1{}^T - 12\, d_2{}^T}{6\, r_1{}^T}}\theta} \\
& + c_4\, e^{\sqrt{\frac{\left(12\, d_2{}^T - \left(r_1{}^T + 2d_4{}^T\right)^2\right) + I\sqrt{3}\left(\left(r_1{}^T\right)^2 + 12\, d_2{}^T - 4\left(d_4^T\right)^2\right)}{12\, r_1{}^T}}\theta} \\
& + c_5\, e^{\sqrt{\frac{\left(12\, d_2{}^T - \left(r_1{}^T + 2d_4{}^T\right)^2\right) - I\sqrt{3}\left(\left(r_1{}^T\right)^2 + 12\, d_2{}^T - 4\left(d_4^T\right)^2\right)}{12\, r_1}}\theta} \\
& + c_6\, e^{-\sqrt{\frac{\left(12\, d_2{}^T - \left(r_1{}^T + 2d_4{}^T\right)^2\right) + I\sqrt{3}\left(\left(r_1{}^T\right)^2 + 12\, d_2{}^T - 4\left(d_4^T\right)^2\right)}{12\, r_1{}^T}}\theta} \\
& + c_7\, e^{-\sqrt{\frac{\left(12\, d_2{}^T - \left(r_1{}^T + 2d_4{}^T\right)^2\right) - I\sqrt{3}\left(\left(r_1{}^T\right)^2 + 12\, d_2{}^T - 4\left(d_4^T\right)^2\right)}{12\, r_1{}^T}}\theta}
\end{aligned}
\tag{2.4.8}
$$

Using Euler's formula, (2.4.8) may also be written in the form

$$
\begin{aligned}
u_r{}^T(\theta) = {} & c_2 \cos\left(A_2{}^T\,\theta\right) - c_3 \sin\left(A_2{}^T\,\theta\right) \\
& + c_4 \cos\left(\theta\left(A_3{}^T + A_4{}^T\right)\right) - c_5 \sin\left(\theta\left(A_3{}^T + A_4{}^T\right)\right) \\
& + c_6 \cos\left(\theta\left(A_3{}^T - A_4{}^T\right)\right) - c_7 \sin\left(\theta\left(A_3{}^T - A_4{}^T\right)\right)
\end{aligned}
\tag{2.4.9}
$$

where $A_2{}^T$ through $A_4{}^T$ are given by (2.4.10).

$$
\begin{aligned}
A_2 &= \sqrt{\frac{12\, d_2{}^T - \left(2\, d_4{}^T - r_1^T\right)^2 - 2\, r_1^T\, d_4{}^T}{6\, r_1^T}} \\
A_3 &= \sqrt{\frac{1}{24\, r_1^T}\left(\begin{array}{l}\left(2\, d_4{}^T + r_1^T\right)^2 - 12\, d_2{}^T \\ \qquad -\sqrt{\left(12\, d_2{}^T - \left(2\, d_4{}^T + r_1^T\right)^2\right)^2 + 3\left(\left(r_1^T\right)^2 - 4\left(d_4^T\right)^2 + 12\, d_2{}^T\right)^2}\end{array}\right)} \\
A_4 &= \sqrt{\frac{1}{24\, r_1^T}\left(\begin{array}{l}\left(2\, d_4{}^T + r_1^T\right)^2 - 12\, d_2{}^T \\ \qquad +\sqrt{\left(12\, d_2{}^T - \left(2\, d_4{}^T + r_1^T\right)^2\right)^2 + 3\left(\left(r_1^T\right)^2 - 4\left(d_4^T\right)^2 + 12\, d_2{}^T\right)^2}\end{array}\right)}
\end{aligned}
\tag{2.4.10}
$$

Because (2.4.9) is the homogeneous solution independent of the inflation pressure, the particular solution for the inflation pressure must be added to it. Therefore, the full solution for the support region is

$$\begin{aligned} u_r{}^T(\theta) = u_{r0} &+ c_2\cos\left(A_2{}^T\theta\right) + c_3\sin\left(A_2{}^T\theta\right) \\ &+ c_4\cos\left(\theta\left(A_3{}^T + A_4{}^T\right)\right) + c_5\sin\left(\theta\left(A_3{}^T + A_4{}^T\right)\right) \\ &+ c_6\cos\left(\theta\left(A_3{}^T - A_4{}^T\right)\right) + c_7\sin\left(\theta\left(A_3{}^T - A_4{}^T\right)\right) \end{aligned} \tag{2.4.11}$$

Substituting (2.4.11) into $(2.3.12)_{2\text{-}3}$ allows the circumferential deformation and cross-sectional rotation to be determined as

$$\begin{aligned} u_{\theta 0}^T(\theta) &= c_1 + B_2{}^T\left(c_2\sin\left(A_2{}^T\theta\right) - c_3\cos\left(A_2{}^T\theta\right)\right) \\ &\quad + B_3{}^T\left(c_4\sin\left(\theta\left(A_3{}^T + A_4{}^T\right)\right) - c_5\cos\left(\theta\left(A_3{}^T + A_4{}^T\right)\right)\right) \\ &\quad + B_4{}^T\left(c_6\sin\left(\theta\left(A_3{}^T - A_4{}^T\right)\right) - c_7\cos\left(\theta\left(A_3{}^T - A_4{}^T\right)\right)\right) \\ \phi^T(\theta) &= c_1 C_1{}^T + C_2{}^T\left(c_2\sin\left(A_2{}^T\theta\right) + c_3\cos\left(A_2{}^T\theta\right)\right) \\ &\quad + C_3{}^T\left(c_4\sin\left(\theta\left(A_3{}^T + A_4{}^T\right)\right) + c_5\cos\left(\theta\left(A_3{}^T + A_4{}^T\right)\right)\right) \\ &\quad + C_4{}^T\left(c_6\sin\left(\theta\left(A_3{}^T - A_4{}^T\right)\right) + c_7\cos\left(\theta\left(A_3{}^T - A_4{}^T\right)\right)\right) \end{aligned} \tag{2.4.12}$$

where $B_2{}^T$ through $B_4{}^T$ and $C_1{}^T$ through $C_4{}^T$ are

$$B_2^{\,T} = -\frac{\left(A_2^T\right)^2 Q_1\left(\left(\left(A_2^T\right)^2 - 1\right)GA + R^2 K_r^{\,T}\right) + GA\,Q_2\left(EA + R^2 K_r^{\,T}\right)}{GA\,A_2^{\,T}}$$

$$B_3 = -\frac{\left(A_3^{\,T} + A_4^{\,T}\right)^2 Q_1\left(\left(\left(A_3^{\,T} + A_4^{\,T}\right)^2 - 1\right)GA + R^2 K_r^{\,T}\right) + GA\,Q_2\left(EA + R^2 K_r^{\,T}\right)}{GA\left(A_3^{\,T} + A_4^{\,T}\right)}$$

$$B_4 = -\frac{\left(A_3^{\,T} - A_4^{\,T}\right)^2 Q_1\left(\left(\left(A_3^{\,T} - A_4^{\,T}\right)^2 - 1\right)GA + R^2 K_r^{\,T}\right) + GA\,Q_2\left(EA + R^2 K_r^{\,T}\right)}{GA\left(A_3^{\,T} - A_4^{\,T}\right)}$$

$$C_1 = \frac{GA + R^2 K_\theta}{R\,GA}$$

$$C_2^{\,T} = \frac{A_2^{\,T}\left(EA + GA\right) + B_2^{\,T}\left(\left(A_2^T\right)^2 EA + GA + R^2 K_\theta\right)}{R\,GA}$$

$$C_3^{\,T} = \frac{\left(A_3^{\,T} + A_4^{\,T}\right)\left(EA + GA\right) + B_3^{\,T}\left(\left(A_3^{\,T} + A_4^{\,T}\right)^2 EA + GA + R^2 K_\theta\right)}{R\,GA}$$

$$C_4^{\,T} = \frac{\left(A_3^{\,T} - A_4^{\,T}\right)\left(EA + GA\right) + B_4^{\,T}\left(\left(A_3^{\,T} - A_4^{\,T}\right)^2 EA + GA + R^2 K_\theta\right)}{R\,GA} \qquad (2.4.13)$$

The internal forces and moments in the support region are found by substituting (2.4.11) and (2.4.12) into (2.2.18) to obtain the expressions in (2.4.14).

$$
\begin{aligned}
V^T(\theta) = -\frac{GA}{R}\Bigg(& \left(1 - RC_1^T\right)c_1 + \left(A_2^T + B_2^T - RC_2^T\right)\begin{pmatrix} c_2\sin\left(A_2^T\theta\right) \\ -c_3\cos\left(A_2^T\theta\right)\end{pmatrix} \\
& + \left(A_3^T + A_4^T + B_3^T - RC_3^T\right)\begin{pmatrix} c_4\sin\left(\theta\left(A_3^T + A_4^T\right)\right) \\ -c_5\cos\left(\theta\left(A_3^T + A_4^T\right)\right)\end{pmatrix} \\
& + \left(A_3^T - A_4^T + B_4^T - RC_4^T\right)\begin{pmatrix} c_6\sin\left(\theta\left(A_3^T - A_4^T\right)\right) \\ -c_7\cos\left(\theta\left(A_3^T - A_4^T\right)\right)\end{pmatrix}\Bigg) \\
N^T(\theta) = \frac{EA}{R}\Bigg(& u_{r0} + \left(1 + A_2^T B_2^T\right)\begin{pmatrix} c_2\cos\left(A_2^T\theta\right) \\ +c_3\sin\left(A_2^T\theta\right)\end{pmatrix} \\
& + \left(1 + \left(A_3^T + A_4^T\right)B_3^T\right)\begin{pmatrix} c_4\cos\left(\theta\left(A_3^T + A_4^T\right)\right) \\ +c_5\sin\left(\theta\left(A_3^T + A_4^T\right)\right)\end{pmatrix} \\
& + \left(1 + \left(A_3^T - A_4^T\right)B_4^T\right)\begin{pmatrix} c_6\cos\left(\theta\left(A_3^T - A_4^T\right)\right) \\ +c_7\sin\left(\theta\left(A_3^T - A_4^T\right)\right)\end{pmatrix}\Bigg) \\
M^T(\theta) = \frac{EI}{R}\Bigg(& C_2^T A_2^T\begin{pmatrix} c_2\cos\left(A_2^T\theta\right) \\ +c_3\sin\left(A_2^T\theta\right)\end{pmatrix} \\
& + C_3^T\left(A_3^T + A_4^T\right)\begin{pmatrix} c_4\cos\left(\theta\left(A_3^T + A_4^T\right)\right) \\ +c_5\sin\left(\theta\left(A_3^T + A_4^T\right)\right)\end{pmatrix} \\
& + C_4^T\left(A_3^T - A_4^T\right)\begin{pmatrix} c_6\cos\left(\theta\left(A_3^T - A_4^T\right)\right) \\ +c_7\sin\left(\theta\left(A_3^T - A_4^T\right)\right)\end{pmatrix}\Bigg)
\end{aligned}
\tag{2.4.14}
$$

While manipulating the differential equations to decouple them, derivatives are sometimes taken that produce extraneous integration constants in the solution. The fact that this has occurred here is evidence that there are seven degrees of freedom in the solution for a six degree of freedom system of differential equations. In order to determine the constraint equation to be placed on this extra degree of freedom, the solution is substituted into the coupled differential equations. When this is done with the solution given in (2.4.11) and (2.4.12), the relation in (2.4.15) is obtained from $(2.2.19)_3$.

$$-R^3\ K_\theta\ c_1 = 0 \tag{2.4.15}$$

Therefore, c_1 is required to be zero. The physical meaning of this is that when the ring is constrained in both the radial and circumferential directions by springs, all rigid body motions are eliminated. Therefore, the condition in (2.4.15) is reasonable since it only appears when the circumferential stiffness is non-zero. The true solution for the support region is given by (2.4.16) and (2.4.17).

$$\begin{aligned}
u_r^{\ T}(\theta) &= u_{r0} + c_2\cos\left(A_2^{\ T}\theta\right) + c_3\sin\left(A_2^{\ T}\theta\right) \\
&\quad + c_4\cos\left(\theta\left(A_3^{\ T} + A_4^{\ T}\right)\right) + c_5\sin\left(\theta\left(A_3^{\ T} + A_4^{\ T}\right)\right) \\
&\quad + c_6\cos\left(\theta\left(A_3^{\ T} - A_4^{\ T}\right)\right) + c_7\sin\left(\theta\left(A_3^{\ T} - A_4^{\ T}\right)\right) \\
u_{\theta 0}^{T}(\theta) &= B_2^{\ T}\left(c_2\sin\left(A_2^{\ T}\theta\right) - c_3\cos\left(A_2^{\ T}\theta\right)\right) \\
&\quad + B_3^{\ T}\left(c_4\sin\left(\theta\left(A_3^{\ T} + A_4^{\ T}\right)\right) - c_5\cos\left(\theta\left(A_3^{\ T} + A_4^{\ T}\right)\right)\right) \\
&\quad + B_4^{\ T}\left(c_6\sin\left(\theta\left(A_3^{\ T} - A_4^{\ T}\right)\right) - c_7\cos\left(\theta\left(A_3^{\ T} - A_4^{\ T}\right)\right)\right) \\
\phi^T(\theta) &= C_2^{\ T}\left(c_2\sin\left(A_2^{\ T}\theta\right) + c_3\cos\left(A_2^{\ T}\theta\right)\right) \\
&\quad + C_3^{\ T}\left(c_4\sin\left(\theta\left(A_3^{\ T} + A_4^{\ T}\right)\right) + c_5\cos\left(\theta\left(A_3^{\ T} + A_4^{\ T}\right)\right)\right) \\
&\quad + C_4^{\ T}\left(c_6\sin\left(\theta\left(A_3^{\ T} - A_4^{\ T}\right)\right) + c_7\cos\left(\theta\left(A_3^{\ T} - A_4^{\ T}\right)\right)\right)
\end{aligned} \tag{2.4.16}$$

$$
\begin{aligned}
V^T(\theta) &= -\frac{GA}{R}\left(\begin{array}{l}
\left(A_2^T + B_2^T - RC_2^T\right)\left(\begin{array}{l} c_2\sin\left(A_2^T\theta\right) \\ \quad -c_3\cos\left(A_2^T\theta\right)\end{array}\right) \\
\quad +\left(A_3^T + A_4^T + B_3^T - RC_3^T\right)\left(\begin{array}{l} c_4\sin\left(\theta\left(A_3^T + A_4^T\right)\right) \\ \quad -c_5\cos\left(\theta\left(A_3^T + A_4^T\right)\right)\end{array}\right) \\
\quad +\left(A_3^T - A_4^T + B_4^T - RC_4^T\right)\left(\begin{array}{l} c_6\sin\left(\theta\left(A_3^T - A_4^T\right)\right) \\ \quad -c_7\cos\left(\theta\left(A_3^T - A_4^T\right)\right)\end{array}\right)
\end{array}\right) \\
N^T(\theta) &= \frac{EA}{R}\left(\begin{array}{l}
u_{r0} + \left(1 + A_2^T B_2^T\right)\left(\begin{array}{l} c_2\cos\left(A_2^T\theta\right) \\ \quad +c_3\sin\left(A_2^T\theta\right)\end{array}\right) \\
\quad +\left(1 + \left(A_3^T + A_4^T\right)B_3^T\right)\left(\begin{array}{l} c_4\cos\left(\theta\left(A_3^T + A_4^T\right)\right) \\ \quad +c_5\sin\left(\theta\left(A_3^T + A_4^T\right)\right)\end{array}\right) \\
\quad +\left(1 + \left(A_3^T - A_4^T\right)B_4^T\right)\left(\begin{array}{l} c_6\cos\left(\theta\left(A_3^T - A_4^T\right)\right) \\ \quad +c_7\sin\left(\theta\left(A_3^T - A_4^T\right)\right)\end{array}\right)
\end{array}\right) \\
M^T(\theta) &= \frac{EI}{R}\left(\begin{array}{l}
C_2^T A_2^T\left(\begin{array}{l} c_2\cos\left(A_2^T\theta\right) \\ \quad +c_3\sin\left(A_2^T\theta\right)\end{array}\right) \\
\quad +C_3^T\left(A_3^T + A_4^T\right)\left(\begin{array}{l} c_4\cos\left(\theta\left(A_3^T + A_4^T\right)\right) \\ \quad +c_5\sin\left(\theta\left(A_3^T + A_4^T\right)\right)\end{array}\right) \\
\quad +C_4^T\left(A_3^T - A_4^T\right)\left(\begin{array}{l} c_6\cos\left(\theta\left(A_3^T - A_4^T\right)\right) \\ \quad +c_7\sin\left(\theta\left(A_3^T - A_4^T\right)\right)\end{array}\right)
\end{array}\right)
\end{aligned}
\tag{2.4.17}
$$

2.4.3. Non-Contact Solution in the Compression Support Region

Since the only difference between the non-contact tension ($u_r > u_{r0}$) and compression ($u_r < u_{r0}$) solutions is the magnitude of the radial carcass stiffness, the form of the solution is the same and can be expressed as

$$
\begin{aligned}
u_r{}^C(\theta) &= u_{r0} + c_9\cos\left(A_2{}^C\theta\right) + c_{10}\sin\left(A_2{}^C\theta\right) \\
&\quad + c_{11}\cos\left(\theta\left(A_3{}^C + A_4{}^C\right)\right) + c_{12}\sin\left(\theta\left(A_3{}^C + A_4{}^C\right)\right) \\
&\quad + c_{13}\cos\left(\theta\left(A_3{}^C - A_4{}^C\right)\right) + c_{14}\sin\left(\theta\left(A_3{}^C - A_4{}^C\right)\right) \\
u_{\theta 0}^C(\theta) &= B_2{}^C\left(c_9\sin\left(A_2{}^C\theta\right) - c_{10}\cos\left(A_2{}^C\theta\right)\right) \\
&\quad + B_3{}^C\left(c_{11}\sin\left(\theta\left(A_3{}^C + A_4{}^C\right)\right) - c_{12}\cos\left(\theta\left(A_3{}^C + A_4{}^C\right)\right)\right) \\
&\quad + B_4{}^C\left(c_{13}\sin\left(\theta\left(A_3{}^C - A_4{}^C\right)\right) - c_{14}\cos\left(\theta\left(A_3{}^C - A_4{}^C\right)\right)\right) \\
\phi^C(\theta) &= C_2{}^C\left(c_9\sin\left(A_2{}^C\theta\right) + c_{10}\cos\left(A_2{}^C\theta\right)\right) \\
&\quad + C_3{}^C\left(c_{11}\sin\left(\theta\left(A_3{}^C + A_4{}^C\right)\right) + c_{12}\cos\left(\theta\left(A_3{}^C + A_4{}^C\right)\right)\right) \\
&\quad + C_4{}^C\left(c_{13}\sin\left(\theta\left(A_3{}^C - A_4{}^C\right)\right) + c_{14}\cos\left(\theta\left(A_3{}^C - A_4{}^C\right)\right)\right)
\end{aligned}
\tag{2.4.18}
$$

$$
\begin{aligned}
V^C(\theta) &= -\frac{GA}{R}\left(\begin{array}{l}
\left(A_2{}^C + B_2{}^C - RC_2{}^C\right)\left(\begin{array}{l} c_9\sin\left(A_2{}^C\theta\right) \\ \qquad -c_{10}\cos\left(A_2{}^C\theta\right)\end{array}\right) \\
\quad +\left(A_3{}^C + A_4{}^C + B_3{}^C - RC_3{}^C\right)\left(\begin{array}{l} c_{11}\sin\left(\theta\left(A_3{}^C + A_4{}^C\right)\right) \\ \qquad -c_{12}\cos\left(\theta\left(A_3{}^C + A_4{}^C\right)\right)\end{array}\right) \\
\quad +\left(A_3{}^C - A_4{}^C + B_4{}^C - RC_4{}^C\right)\left(\begin{array}{l} c_{13}\sin\left(\theta\left(A_3{}^C - A_4{}^C\right)\right) \\ \qquad -c_{14}\cos\left(\theta\left(A_3{}^C - A_4{}^C\right)\right)\end{array}\right)
\end{array}\right) \\
N^C(\theta) &= \frac{EA}{R}\left(\begin{array}{l}
u_{r0} + \left(1 + A_2{}^C B_2{}^C\right)\left(\begin{array}{l} c_9\cos\left(A_2{}^C\theta\right) \\ \qquad +c_{10}\sin\left(A_2{}^C\theta\right)\end{array}\right) \\
\quad +\left(1 + \left(A_3{}^C + A_4{}^C\right)B_3{}^C\right)\left(\begin{array}{l} c_{11}\cos\left(\theta\left(A_3{}^C + A_4{}^C\right)\right) \\ \qquad +c_{12}\sin\left(\theta\left(A_3{}^C + A_4{}^C\right)\right)\end{array}\right) \\
\quad +\left(1 + \left(A_3{}^C - A_4{}^C\right)B_4{}^C\right)\left(\begin{array}{l} c_{13}\cos\left(\theta\left(A_3{}^C - A_4{}^C\right)\right) \\ \qquad +c_{14}\sin\left(\theta\left(A_3{}^C - A_4{}^C\right)\right)\end{array}\right)
\end{array}\right) \\
M^C(\theta) &= \frac{EI}{R}\left(\begin{array}{l}
C_2{}^C A_2{}^C\left(\begin{array}{l} c_9\cos\left(A_2{}^C\theta\right) \\ \qquad +c_{10}\sin\left(A_2{}^C\theta\right)\end{array}\right) \\
\quad +C_3{}^C\left(A_3{}^C + A_4{}^C\right)\left(\begin{array}{l} c_{11}\cos\left(\theta\left(A_3{}^C + A_4{}^C\right)\right) \\ \qquad +c_{12}\sin\left(\theta\left(A_3{}^C + A_4{}^C\right)\right)\end{array}\right) \\
\quad +C_4{}^C\left(A_3{}^C - A_4{}^C\right)\left(\begin{array}{l} c_{13}\cos\left(\theta\left(A_3{}^C - A_4{}^C\right)\right) \\ \qquad +c_{14}\sin\left(\theta\left(A_3{}^C - A_4{}^C\right)\right)\end{array}\right)
\end{array}\right)
\end{aligned}
\tag{2.4.19}
$$

In these equations, the C-superscript denotes that the value is calculated using the radial carcass stiffness in compression instead of the radial carcass in tension.

2.4.4. Contact Solution

In this section, the approximate method proposed by Gasmi, et al. [2] is used to address the contact pressure. Assuming frictionless contact, the contact pressure is normal to the rigid, flat ground (e.g. vertical), which results in radial and circumferential pressure distributions of

$$
\begin{aligned}
q_{gr}(\theta) &= q_g(\theta)\cos(\theta) \\
q_{g\theta}(\theta) &= -q_g(\theta)\sin(\theta)
\end{aligned}
\tag{2.4.20}
$$

Since the ground pressure is symmetric about the center of contact, it can be approximated by a series of cosines.

$$q_g(\theta) = \sum_{n=0}^{\infty} q_n \cos(n\theta) \cong \sum_{n=0}^{m} q_n \cos(n\theta) \tag{2.4.21}$$

The particular solution for the n^{th} pressure term is determined using the method of undetermined coefficients and is given by (2.4.22).

$$\begin{aligned} u_r^{(n)}(\theta) &= q_n \left(D_{1n} \cos\left(\theta(n+1)\right) + D_{2n} \cos\left(\theta(n-1)\right)\right) \\ u_{\theta 0}^{(n)}(\theta) &= q_n \left(E_{1n} \sin\left(\theta(n+1)\right) + E_{2n} \sin\left(\theta(n-1)\right)\right) \\ \phi^{(n)}(\theta) &= q_n \left(F_{1n} \sin\left(\theta(n+1)\right) + F_{2n} \sin\left(\theta(n-1)\right)\right) \end{aligned} \tag{2.4.22}$$

The internal forces and moments due to the n^{th} contact pressure term are found by substituting (2.4.22) into (2.2.18) to obtain the expressions in (2.4.23).

$$\begin{aligned} V^{(n)}(\theta) &= -q_n \frac{GA}{R} \begin{pmatrix} \left(D_{1n}(n+1) + E_{1n} - R F_{1n}\right) \sin\left(\theta(n+1)\right) \\ + \left(D_{2n}(n-1) + E_{2n} - R F_{2n}\right) \sin\left(\theta(n-1)\right) \end{pmatrix} \\ N^{(n)}(\theta) &= q_n \frac{EA}{R} \begin{pmatrix} \left(D_{1n} + E_{1n}(n+1)\right) \cos\left(\theta(n+1)\right) \\ + \left(D_{2n} + E_{2n}(n-1)\right) \cos\left(\theta(n-1)\right) \end{pmatrix} \\ M^{(n)}(\theta) &= q_n \frac{EI}{R} \begin{pmatrix} F_{1n}(n+1) \cos\left(\theta(n+1)\right) \\ + F_{2n}(n-1) \cos\left(\theta(n-1)\right) \end{pmatrix} \end{aligned} \tag{2.4.23}$$

The particular solutions given in (2.4.22) and (2.4.23) are used with (2.4.18) and (2.4.19) to obtain the full solution for the contact region given in (2.4.24).

$$\begin{aligned} u_r{}^G &= u_r{}^C + \sum_{n=0}^{m} u_r^{(n)}; \quad u_{\theta 0}^G = u_{\theta 0}^C + \sum_{n=0}^{m} u_\theta^{(n)}; \quad \phi^G = \phi^C + \sum_{n=0}^{m} \phi^{(n)} \\ V^G &= V^C + \sum_{n=0}^{m} V^{(n)}; \quad N^G = N^C + \sum_{n=0}^{m} N^{(n)}; \quad M^G = M^C + \sum_{n=0}^{m} M^{(n)} \end{aligned} \tag{2.4.24}$$

The constants introduced in (2.4.22) and (2.4.23) are

$$
\begin{aligned}
D_{1n} &= \frac{\left(EA\,EI\,(n+1)^2 + EI\,GA(n+1) + R^2\,GA\,EA\right)(n+1)(n+2) + R^2 K_\theta\left(R^2\,GA + EI\,(n+1)^2\right)}{GA\,EA\,EI\,n^2(n+2)^2(n+1)^2 + R^2\left(\begin{array}{l} EI\,GA(n+1)^2\left(K_0(n+1)^2 + K_r{}^C\right) \\ \quad +\left(EI\,(n+1)^2 + R^2\,GA\right)\left(K_0\left(R^2\,K_r{}^C + EA\right) + EA\,K_r{}^C(n+1)^2\right)\end{array}\right)}\frac{R^2 b}{2} \\
D_{2n} &= \frac{\left(EA\,EI\,(n-1)^2 - EI\,GA(n-1) + R^2\,GA\,EA\right)(n-1)(n-2) + R^2\,K_\theta\left(R^2\,GA + EI\,(n-1)^2\right)}{GA\,EA\,EI\,n^2(n-2)^2(n-1)^2 + R^2\left(\begin{array}{l} EI\,GA(n-1)^2\left(K_\theta(n-1)^2 + K_r{}^C\right) \\ \quad +\left(EI\,(n-1)^2 + R^2\,GA\right)\left(K_\theta\left(R^2\,K_r{}^C + EA\right) + EA\,K_r{}^C(n-1)^2\right)\end{array}\right)}\frac{R^2 b}{2} \\
E_{1n} &= -\frac{\left(\begin{array}{l} EA\left(GA\,EI\left(n(n+2)(n+1)^2+1\right) + EA\,R^2\,GA + EA\,EI\right) \\ \quad +R^2\,K_r{}^C\left(EA\,R^2\,GA + EA\,EI\left(n(n+2)+2\right) + GA\,EI\right)\end{array}\right)}{EA\left(EA\,EI + GA\,EI + EA\,R^2\,GA\right) - (EA+GA)\,EI\,R^2\,K_\theta}\frac{D_{1n}}{(n+1)} \\
&\quad + \frac{EA\,R^2\,GA + EA\,EI\left(n(n+3)+3\right) + GA\,EI\,(n+2)}{EA\left(EA\,EI + GA\,EI + EA\,R^2\,GA\right) - (EA+GA)\,EI\,R^2\,K_\theta}\frac{R^2 b}{2(n+1)} \\
E_{2n} &= -\frac{\left(\begin{array}{l} EA\left(GA\,EI\left(n(n-2)(n-1)^2+1\right) + EA\,R^2\,GA + EA\,EI\right) \\ \quad +R^2\,K_r{}^C\left(EA\,R^2\,GA + EA\,EI\left(n(n-2)+2\right) + GA\,EI\right)\end{array}\right)}{EA\left(EA\,EI + GA\,EI + EA\,R^2\,GA\right) - (EA+GA)\,EI\,R^2\,K_\theta}\frac{D2_n}{(n-1)} \\
&\quad + \frac{EA\,R^2\,GA + EA\,EI\left(n(n-3)+3\right) - GA\,EI\,(n-2)}{EA\left(EA\,EI + GA\,EI + EA\,R^2\,GA\right) - (EA+GA)\,EI\,R^2\,K_\theta}\frac{R^2 b}{2(n-1)} \\
F_{1n} &= \frac{1}{R\,GA}\left((n+1)(EA+GA)D_{1n} + \left(GA + EA(n+1)^2 + K_\theta R^2\right)E_{1n} + \frac{R^2 b}{2}\right) \\
F_{2n} &= \frac{1}{R\,GA}\left((n-1)(EA+GA)D_{2n} + \left(GA + EA(n-1)^2 + K_\theta R^2\right)E_{2n} - \frac{R^2 b}{2}\right)
\end{aligned}
\tag{2.4.25}
$$

Noting that in (2.4.22) $n = 1$ is a special case that requires a different solution, the equations are re-solved for $n = 1$ which gives

$$
\begin{aligned}
u_r^{(1)}(\theta) &= q_1\left(D_{11}\cos(2\theta) + D_{21}\right) \\
u_{\theta 0}^{(1)}(\theta) &= q_1\left(E_{11}\sin(2\theta) + E_{21}\,\theta\right) \\
\phi^{(1)}(\theta) &= q_1\left(F_{11}\sin(2\theta) + F_{21}\,\theta\right)
\end{aligned}
\tag{2.4.26}
$$

Substituting (2.4.26) into (2.2.18)

$$
\begin{aligned}
V^{(1)}(\theta) &= -q_1\frac{GA}{R}\left(\left(2D_{11} + E_{11} - R\,F_{11}\right)\sin(2\theta) + \left(E_{21} - R\,F_{21}\right)\theta\right) \\
N^{(1)}(\theta) &= q_1\frac{EA}{R}\left(\left(D_{11} + 2E_{11}\right)\cos(2\theta) + D_{21} + E_{21}\right) \\
M^{(1)}(\theta) &= q_1\frac{EI}{R}\left(2F_{11}\cos(2\theta) + F_{21}\right)
\end{aligned}
\tag{2.4.27}
$$

where the constants in (2.4.26) and (2.4.27) are given in

$$
\begin{aligned}
D_{11} &= \frac{R^2 b\left(6\left(4\,EA\,EI + 2\,EI\,GA + R^2\,EA\,GA\right) + \left(GAR^2 + 4EI\right)R^2 K_\theta\right)}{72\,EA\,EI\,GA + 2R^2\left(4EI\,GA\left(4K_\theta + K_r{}^C\right) + \left(4\,EA\,EI + EAGAR^2\right)\left(K_\theta + 4K_r{}^C\right) + \left(GA\,R^2 + 4EI\right)R^2 K_\theta\,K_r{}^C\right)} \\
D_{21} &= \frac{R^2 b}{2\left(EA + R^2 K_r{}^C\right)} \\
E_{11} &= \left(\frac{7\,EA\,EI + 3GA\,EI + R^2\,EA\,GA}{EA\left(EA\,EI + GA\,EI + R^2\,EA\,GA\right) - \left(EA + GA\right)EI\,R^2\,K_\theta}\right)\frac{R^2 b}{4} \\
&\qquad - \left(\frac{EA\left(13GAEI + EAEI + R^2\,EAGA\right) + R^2\,K_r{}^C\left(EAR^2GA + 5\,EA\,EI + GA\,EI\right)}{EA\left(EA\,EI + GA\,EI + R^2\,EA\,GA\right) - \left(EA + GA\right)EI\,R^2\,K_\theta}\right)\frac{D_{11}}{2} \\
E_{21} &= \left(\frac{EA\,EI + GA\,EI + R^2\,EA\,GA}{EA\left(EA\,EI + GA\,EI + R^2\,EA\,GA\right) - \left(EA + GA\right)EI\,R^2 K_\theta}\right)\frac{R^2 b}{2} \\
&\qquad - \left(\frac{\left(EA + R^2 K_r{}^C\right)\left(EAEI + GAEI + EAR^2GA\right)}{EA\left(EA\,EI + GA\,EI + R^2\,EA\,GA\right) - \left(EA + GA\right)EI\,R^2 K_\theta}\right)D_{21} \\
F_{11} &= \frac{1}{RGA}\left(2\left(EA + GA\right)D_{11} + \left(GA + 4EA + R^2 K_\theta\right)E_{11} + \frac{R^2 b}{2}\right) \\
F_{21} &= \frac{\left(GA + R^2 K_\theta\right)E_{21}}{RGA}
\end{aligned}
\tag{2.4.28}
$$

2.5. Solving for the Unknowns

Three regions exist in a pneumatic tire: the contact region, the compressed support region, and the tensioned support region. The boundaries of these regions are defined to be the contact angle (θ_L) and the bifurcation (spoke) angle (θ_S). The solution to the governing differential equations gives the following expressions for each of these three separate regions of the tire.

For the support region in tension (i.e. $\theta \geq \theta_S$), the displacements, forces, and moments are given as

$$
\begin{aligned}
u_r{}^T(\theta) &= u_{r0} + c_2\cos\left(A_2{}^T\theta\right) + c_3\sin\left(A_2{}^T\theta\right) \\
&\quad + c_4\cos\left(\theta\left(A_3{}^T + A_4{}^T\right)\right) + c_5\sin\left(\theta\left(A_3{}^T + A_4{}^T\right)\right) \\
&\quad + c_6\cos\left(\theta\left(A_3{}^T - A_4{}^T\right)\right) + c_7\sin\left(\theta\left(A_3{}^T - A_4{}^T\right)\right) \\
u_{\theta 0}{}^T(\theta) &= B_2{}^T\left(c_2\sin\left(A_2{}^T\theta\right) - c_3\cos\left(A_2{}^T\theta\right)\right) \\
&\quad + B_3{}^T\left(c_4\sin\left(\theta\left(A_3{}^T + A_4{}^T\right)\right) - c_5\cos\left(\theta\left(A_3{}^T + A_4{}^T\right)\right)\right) \\
&\quad + B_4{}^T\left(c_6\sin\left(\theta\left(A_3{}^T - A_4{}^T\right)\right) - c_7\cos\left(\theta\left(A_3{}^T - A_4{}^T\right)\right)\right) \\
\phi^T(\theta) &= C_2{}^T\left(c_2\sin\left(A_2{}^T\theta\right) + c_3\cos\left(A_2{}^T\theta\right)\right) \\
&\quad + C_3{}^T\left(c_4\sin\left(\theta\left(A_3{}^T + A_4{}^T\right)\right) + c_5\cos\left(\theta\left(A_3{}^T + A_4{}^T\right)\right)\right) \\
&\quad + C_4{}^T\left(c_6\sin\left(\theta\left(A_3{}^T - A_4{}^T\right)\right) + c_7\cos\left(\theta\left(A_3{}^T - A_4{}^T\right)\right)\right) \\
V^T(\theta) &= -\frac{GA}{R}\left(\begin{array}{l}
\left(A_2{}^T + B_2{}^T - RC_2{}^T\right)\left(\begin{array}{r} c_2\sin\left(A_2{}^T\theta\right) \\ -c_3\cos\left(A_2{}^T\theta\right)\end{array}\right) \\
\quad + \left(A_3{}^T + A_4{}^T + B_3{}^T - RC_3{}^T\right)\left(\begin{array}{r} c_4\sin\left(\theta\left(A_3{}^T + A_4{}^T\right)\right) \\ -c_5\cos\left(\theta\left(A_3{}^T + A_4{}^T\right)\right)\end{array}\right) \\
\quad + \left(A_3{}^T - A_4{}^T + B_4{}^T - RC_4{}^T\right)\left(\begin{array}{r} c_6\sin\left(\theta\left(A_3{}^T - A_4{}^T\right)\right) \\ -c_7\cos\left(\theta\left(A_3{}^T - A_4{}^T\right)\right)\end{array}\right)
\end{array}\right) \\
N^T(\theta) &= \frac{EA}{R}\left(\begin{array}{l}
u_{r0} + \left(1 + A_2{}^T B_2{}^T\right)\left(\begin{array}{r} c_2\cos\left(A_2{}^T\theta\right) \\ +c_3\sin\left(A_2{}^T\theta\right)\end{array}\right) \\
\quad + \left(1 + \left(A_3{}^T + A_4{}^T\right)B_3{}^T\right)\left(\begin{array}{r} c_4\cos\left(\theta\left(A_3{}^T + A_4{}^T\right)\right) \\ +c_5\sin\left(\theta\left(A_3{}^T + A_4{}^T\right)\right)\end{array}\right) \\
\quad + \left(1 + \left(A_3{}^T - A_4{}^T\right)B_4{}^T\right)\left(\begin{array}{r} c_6\cos\left(\theta\left(A_3{}^T - A_4{}^T\right)\right) \\ +c_7\sin\left(\theta\left(A_3{}^T - A_4{}^T\right)\right)\end{array}\right)
\end{array}\right) \\
M^T(\theta) &= \frac{EI}{R}\left(\begin{array}{l}
C_2{}^T A_2{}^T\left(\begin{array}{r} c_2\cos\left(A_2{}^T\theta\right) \\ +c_3\sin\left(A_2{}^T\theta\right)\end{array}\right) \\
\quad + C_3{}^T\left(A_3{}^T + A_4{}^T\right)\left(\begin{array}{r} c_4\cos\left(\theta\left(A_3{}^T + A_4{}^T\right)\right) \\ +c_5\sin\left(\theta\left(A_3{}^T + A_4{}^T\right)\right)\end{array}\right) \\
\quad + C_4{}^T\left(A_3{}^T - A_4{}^T\right)\left(\begin{array}{r} c_6\cos\left(\theta\left(A_3{}^T - A_4{}^T\right)\right) \\ +c_7\sin\left(\theta\left(A_3{}^T - A_4{}^T\right)\right)\end{array}\right)
\end{array}\right)
\end{aligned}
\tag{2.5.1}
$$

For the support region in compression (i.e. $\theta_L \le \theta \le \theta_S$), the displacements, forces, and moments are given as

$$
\begin{aligned}
u_r{}^C(\theta) &= u_{r0} + c_9\cos\left(A_2{}^C\theta\right) + c_{10}\sin\left(A_2{}^C\theta\right) \\
&\quad + c_{11}\cos\left(\theta\left(A_3{}^C + A_4{}^C\right)\right) + c_{12}\sin\left(\theta\left(A_3{}^C + A_4{}^C\right)\right) \\
&\quad + c_{13}\cos\left(\theta\left(A_3{}^C - A_4{}^C\right)\right) + c_{14}\sin\left(\theta\left(A_3{}^C - A_4{}^C\right)\right) \\
u_{\theta 0}{}^C(\theta) &= B_2{}^C\left(c_9\sin\left(A_2{}^C\theta\right) - c_{10}\cos\left(A_2{}^C\theta\right)\right) \\
&\quad + B_3{}^C\left(c_{11}\sin\left(\theta\left(A_3{}^C + A_4{}^C\right)\right) - c_{12}\cos\left(\theta\left(A_3{}^C + A_4{}^C\right)\right)\right) \\
&\quad + B_4{}^C\left(c_{13}\sin\left(\theta\left(A_3{}^C - A_4{}^C\right)\right) - c_{14}\cos\left(\theta\left(A_3{}^C - A_4{}^C\right)\right)\right) \\
\phi^C(\theta) &= C_2{}^C\left(c_9\sin\left(A_2{}^C\theta\right) + c_{10}\cos\left(A_2{}^C\theta\right)\right) \\
&\quad + C_3{}^C\left(c_{11}\sin\left(\theta\left(A_3{}^C + A_4{}^C\right)\right) + c_{12}\cos\left(\theta\left(A_3{}^C + A_4{}^C\right)\right)\right) \\
&\quad + C_4{}^C\left(c_{13}\sin\left(\theta\left(A_3{}^C - A_4{}^C\right)\right) + c_{14}\cos\left(\theta\left(A_3{}^C - A_4{}^C\right)\right)\right) \\
V^C(\theta) &= -\frac{GA}{R}\left(\begin{array}{l}
\left(A_2{}^C + B_2{}^C - RC_2{}^C\right)\left(\begin{array}{r} c_9\sin\left(A_2{}^C\theta\right) \\ -c_{10}\cos\left(A_2{}^C\theta\right)\end{array}\right) \\
\quad + \left(A_3{}^C + A_4{}^C + B_3{}^C - RC_3{}^C\right)\left(\begin{array}{r} c_{11}\sin\left(\theta\left(A_3{}^C + A_4{}^C\right)\right) \\ -c_{12}\cos\left(\theta\left(A_3{}^C + A_4{}^C\right)\right)\end{array}\right) \\
\quad + \left(A_3{}^C - A_4{}^C + B_4{}^C - RC_4{}^C\right)\left(\begin{array}{r} c_{13}\sin\left(\theta\left(A_3{}^C - A_4{}^C\right)\right) \\ -c_{14}\cos\left(\theta\left(A_3{}^C - A_4{}^C\right)\right)\end{array}\right)
\end{array}\right) \\
N^C(\theta) &= \frac{EA}{R}\left(\begin{array}{l}
u_{r0} + \left(1 + A_2{}^C B_2{}^C\right)\left(\begin{array}{r} c_9\cos\left(A_2{}^C\theta\right) \\ +c_{10}\sin\left(A_2{}^C\theta\right)\end{array}\right) \\
\quad + \left(1 + \left(A_3{}^C + A_4{}^C\right)B_3{}^C\right)\left(\begin{array}{r} c_{11}\cos\left(\theta\left(A_3{}^C + A_4{}^C\right)\right) \\ +c_{12}\sin\left(\theta\left(A_3{}^C + A_4{}^C\right)\right)\end{array}\right) \\
\quad + \left(1 + \left(A_3{}^C - A_4{}^C\right)B_4{}^C\right)\left(\begin{array}{r} c_{13}\cos\left(\theta\left(A_3{}^C - A_4{}^C\right)\right) \\ +c_{14}\sin\left(\theta\left(A_3{}^C - A_4{}^C\right)\right)\end{array}\right)
\end{array}\right) \\
M^C(\theta) &= \frac{EI}{R}\left(\begin{array}{l}
C_2{}^C A_2{}^C\left(\begin{array}{r} c_9\cos\left(A_2{}^C\theta\right) \\ +c_{10}\sin\left(A_2{}^C\theta\right)\end{array}\right) \\
\quad + C_3{}^C\left(A_3{}^C + A_4{}^C\right)\left(\begin{array}{r} c_{11}\cos\left(\theta\left(A_3{}^C + A_4{}^C\right)\right) \\ +c_{12}\sin\left(\theta\left(A_3{}^C + A_4{}^C\right)\right)\end{array}\right) \\
\quad + C_4{}^C\left(A_3{}^C - A_4{}^C\right)\left(\begin{array}{r} c_{13}\cos\left(\theta\left(A_3{}^C - A_4{}^C\right)\right) \\ +c_{14}\sin\left(\theta\left(A_3{}^C - A_4{}^C\right)\right)\end{array}\right)
\end{array}\right)
\end{aligned}
\tag{2.5.2}
$$

For the contact region in compression (i.e. $\theta \le \theta_L$), the displacements, forces, and moments are given as

$$
\begin{aligned}
u_r{}^G(\theta) &= u_{r0} + c_{16}\cos\left(A_2{}^C\theta\right) + c_{17}\sin\left(A_2{}^C\theta\right) \\
&\quad + c_{18}\cos\left(\theta\left(A_3{}^C + A_4{}^C\right)\right) + c_{19}\sin\left(\theta\left(A_3{}^C + A_4{}^C\right)\right) \\
&\quad + c_{20}\cos\left(\theta\left(A_3{}^C - A_4{}^C\right)\right) + c_{21}\sin\left(\theta\left(A_3{}^C - A_4{}^C\right)\right) \\
&\quad + q_1\left(D_{11}\cos(2\theta) + D_{21}\right) + \sum_{\substack{n=0\\ n\neq 1}}^{m} q_n\left(D_{1n}\cos\left(\theta(\alpha n+1)\right) + D_{2n}\cos\left(\theta(\alpha n-1)\right)\right) \\
u_{\theta 0}{}^G(\theta) &= B_2{}^C\left(c_{16}\sin\left(A_2{}^C\theta\right) - c_{17}\cos\left(A_2{}^C\theta\right)\right) \\
&\quad + B_3{}^C\left(c_{18}\sin\left(\theta\left(A_3{}^C + A_4{}^C\right)\right) - c_{19}\cos\left(\theta\left(A_3{}^C + A_4{}^C\right)\right)\right) \\
&\quad + B_4{}^C\left(c_{20}\sin\left(\theta\left(A_3{}^C - A_4{}^C\right)\right) - c_{21}\cos\left(\theta\left(A_3{}^C - A_4{}^C\right)\right)\right) \\
&\quad + q_1\left(E_{11}\sin(2\theta) + E_{21}\theta\right) + \sum_{\substack{n=0\\ n\neq 1}}^{m} q_n\left(E_{1n}\sin\left(\theta(\alpha n+1)\right) + E_{2n}\sin\left(\theta(\alpha n-1)\right)\right) \\
\phi^G(\theta) &= C_2{}^C\left(c_{16}\sin\left(A_2{}^C\theta\right) + c_{17}\cos\left(A_2{}^C\theta\right)\right) \\
&\quad + C_3{}^C\left(c_{18}\sin\left(\theta\left(A_3{}^C + A_4{}^C\right)\right) + c_{19}\cos\left(\theta\left(A_3{}^C + A_4{}^C\right)\right)\right) \\
&\quad + C_4{}^C\left(c_{20}\sin\left(\theta\left(A_3{}^C - A_4{}^C\right)\right) + c_{21}\cos\left(\theta\left(A_3{}^C - A_4{}^C\right)\right)\right) \\
&\quad + q_1\left(F_{11}\sin(2\theta) + F_{21}\theta\right) + \sum_{\substack{n=0\\ n\neq 1}}^{m} q_n\left(F_{1n}\sin\left(\theta(\alpha n+1)\right) + F_{2n}\sin\left(\theta(\alpha n-1)\right)\right) \\
V^G(\theta) &= -\frac{GA}{R}\left(\begin{array}{l}
\left(A_2{}^C + B_2{}^C - RC_2{}^C\right)\left(\begin{array}{l} c_{16}\sin\left(A_2{}^C\theta\right) \\ \quad -c_{17}\cos\left(A_2{}^C\theta\right)\end{array}\right) \\
\quad + \left(A_3{}^C + A_4{}^C + B_3{}^C - RC_3{}^C\right)\left(\begin{array}{l} c_{18}\sin\left(\theta\left(A_3{}^C + A_4{}^C\right)\right) \\ \quad -c_{19}\cos\left(\theta\left(A_3{}^C + A_4{}^C\right)\right)\end{array}\right) \\
\quad + \left(A_3{}^C - A_4{}^C + B_4{}^C - RC_4{}^C\right)\left(\begin{array}{l} c_{20}\sin\left(\theta\left(A_3{}^C - A_4{}^C\right)\right) \\ \quad -c_{21}\cos\left(\theta\left(A_3{}^C - A_4{}^C\right)\right)\end{array}\right) \\
\quad + q_1\left(\left(2D_{11} + E_{11} - RF_{11}\right)\sin(2\theta) + \left(E_{21} - RF_{21}\right)\theta\right) \\
\quad + \sum_{\substack{n=0\\ n\neq 1}}^{m} q_n\left(\begin{array}{l}\left(D_{1n}(\alpha n+1) + E_{1n} - RF_{1n}\right)\sin\left(\theta(\alpha n+1)\right) \\ \quad + \left(D_{2n}(\alpha n-1) + E_{2n} - RF_{2n}\right)\sin\left(\theta(\alpha n-1)\right)\end{array}\right)
\end{array}\right) \\
N^G(\theta) &= \frac{EA}{R}\left(\begin{array}{l}
u_{r0} + \left(1 + A_2{}^C B_2{}^C\right)\left(\begin{array}{l} c_{16}\cos\left(A_2{}^C\theta\right) \\ \quad + c_{17}\sin\left(A_2{}^C\theta\right)\end{array}\right) \\
\quad + \left(1 + \left(A_3{}^C + A_4{}^C\right)B_3{}^C\right)\left(\begin{array}{l} c_{18}\cos\left(\theta\left(A_3{}^C + A_4{}^C\right)\right) \\ \quad + c_{19}\sin\left(\theta\left(A_3{}^C + A_4{}^C\right)\right)\end{array}\right) \\
\quad + \left(1 + \left(A_3{}^C - A_4{}^C\right)B_4{}^C\right)\left(\begin{array}{l} c_{20}\cos\left(\theta\left(A_3{}^C - A_4{}^C\right)\right) \\ \quad + c_{21}\sin\left(\theta\left(A_3{}^C - A_4{}^C\right)\right)\end{array}\right) \\
\quad + q_1\left(\left(D_{11} + 2E_{11}\right)\cos(2\theta) + D_{21} + E_{21}\right) + \sum_{\substack{n=0\\ n\neq 1}}^{m} q_n\left(\begin{array}{l}\left(D_{1n} + E_{1n}(\alpha n+1)\right)\cos\left(\theta(\alpha n+1)\right) \\ \quad + \left(D_{2n} + E_{2n}(\alpha n-1)\right)\cos\left(\theta(\alpha n-1)\right)\end{array}\right)
\end{array}\right) \\
M^G(\theta) &= \frac{EI}{R}\left(\begin{array}{l}
C_2{}^C A_2{}^C\left(\begin{array}{l} c_{16}\cos\left(A_2{}^C\theta\right) \\ \quad + c_{17}\sin\left(A_2{}^C\theta\right)\end{array}\right) \\
\quad + C_3{}^C\left(A_3{}^C + A_4{}^C\right)\left(\begin{array}{l} c_{18}\cos\left(\theta\left(A_3{}^C + A_4{}^C\right)\right) \\ \quad + c_{19}\sin\left(\theta\left(A_3{}^C + A_4{}^C\right)\right)\end{array}\right) \\
\quad + C_4{}^C\left(A_3{}^C - A_4{}^C\right)\left(\begin{array}{l} c_{20}\cos\left(\theta\left(A_3{}^C - A_4{}^C\right)\right) \\ \quad + c_{21}\sin\left(\theta\left(A_3{}^C - A_4{}^C\right)\right)\end{array}\right) \\
\quad + q_1\left(2F_{11}\cos(2\theta) + F_{21}\right) + \sum_{\substack{n=0\\ n\neq 1}}^{m} q_n\left(\begin{array}{l}F_{1n}(\alpha n+1)\cos\left(\theta(\alpha n+1)\right) \\ \quad + F_{2n}(\alpha n-1)\cos\left(\theta(\alpha n-1)\right)\end{array}\right)
\end{array}\right)
\end{aligned}
\tag{2.5.3}
$$

From these equations, it is apparent that there are 18 unknown integration constants (c_1 has been eliminated to satisfy the coupled governing differential equations) and $m + 1$ unknown pressure coefficients. Additionally, the amount of vertical deflection and the value of the bifurcation angle (the angle at which the sidewall switches from compression to tension) for the specified contact angle are unknowns. This gives $21 + m$ unknowns.

The following symmetry conditions,

$$\begin{aligned} u_r^T(\theta) &= u_r^T(\pi - \theta) \\ u_r^G(\theta) &= u_r^G(-\theta) \end{aligned} \tag{2.5.4}$$

allow the three asymmetric integration constants in the contact and tensioned support regions to be eliminated. This leaves 12 integration constants that must be found using the 12 continuity equations given below.

$$\begin{aligned} u_r^T(\theta_S) &= u_r^C(\theta_S) & u_r^C(\theta_L) &= u_r^G(\theta_L) \\ u_{\theta 0}^T(\theta_S) &= u_{\theta 0}^C(\theta_S) & u_{\theta 0}^C(\theta_L) &= u_{\theta 0}^G(\theta_L) \\ \phi^T(\theta_S) &= \phi^C(\theta_S) & \phi^C(\theta_L) &= \phi^G(\theta_L) \\ N^T(\theta_S) &= N^C(\theta_S) & N^C(\theta_L) &= N^G(\theta_L) \\ V^T(\theta_S) &= V^C(\theta_S) & V^C(\theta_L) &= V^G(\theta_L) \\ M^T(\theta_S) &= M^C(\theta_S) & M^C(\theta_L) &= M^G(\theta_L) \end{aligned} \tag{2.5.5}$$

In order to determine the relationship between the coefficients of pressure in (2.4.21), the vertical displacement of the ground, δ, and the known contact angle, θ_L, the kinematic relationship between the vertical displacement of the tire, $v(\theta)$, the vertical displacement of the ground, and u_r and $u_{\theta 0}$ is used.

$$v(\theta) = \delta - R\left(1 - \cos(\theta)\right) = u_{\theta 0}\sin(\theta) - u_r\cos(\theta) \tag{2.5.6}$$

For $m < \infty$, (2.4.21) is an approximation. In order to determine the values of the pressure coefficients in (2.4.21) and the amount of vertical deflection, a Taylor series expansion

of (2.5.6) is taken. The number of coefficients in (2.4.21) limits the number of terms that can be matched from the Taylor series expansion. The vertical displacement of the ground and the m + 1 pressure coefficients make for a total of $m + 2$ unknowns. After the Taylor series expansion has been performed, (2.5.7) is obtained.

$$\delta + \sum_{i=1}^{p} \frac{(-1)^i}{(2i)!} R\theta^{2i} = a_0 + \sum_{i=1}^{p} \frac{(-1)^i}{(2i)!} a_{2i}\,\theta^{2i} \tag{2.5.7}$$

where the constants, a_0 and a_{2i}, are known in terms of derivatives of $u_r(0)$ and $u_\theta(0)$. Therefore, matching coefficients on θ^{2i} gives (2.5.8).

$$\delta = a_0, \;\; R = a_{2i} \qquad\qquad i = 1 \ldots p \tag{2.5.8}$$

Equation (2.5.8) is $p + 1$ equations for $m + 2$ unknowns. Therefore, in order to have an equal number of equations and unknowns, p must be equal to $m + 1$, and the total number of terms that can be satisfied in the Taylor series is $m + 2$. This allows (2.5.6) to be satisfied to order $2\,(m + 1)$ with an error on the order of $\theta^{2\,(m\,+\,1)}$. Since the contact angle is much smaller than unity, the solution typically converges with $m \leq 12$.

Equations (2.5.5) and (2.5.8) give a $14 + m$ by $14 + m$ linear system of equations for a specified contact and bifurcation angle. This system can be visualized below.

$$
[G] = \left[\begin{array}{c|c|ccc|c|c}
\multicolumn{3}{c|}{\text{Integration Constants}} & & & \text{Pressure Coefficients} & \\
\theta_S \le \theta & \theta_L \le \theta \le \theta_S & \theta \le \theta_L & \delta & \theta \le \theta_L & & \\
\hline
\multicolumn{2}{c|}{\begin{matrix} G_{1,1} \\ (6\times 3) \end{matrix}} & \multicolumn{2}{c|}{\begin{matrix} G_{1,2} \\ (6\times 6) \end{matrix}} & \begin{matrix} 0&0&0 \\ 0&0&0 \\ 0&0&0 \\ 0&0&0 \\ 0&0&0 \\ 0&0&0 \end{matrix} & \begin{matrix} 0 \\ 0 \\ 0 \\ 0 \\ 0 \\ 0 \end{matrix} & \begin{matrix} 0&\cdots&0 \\ 0&\cdots&0 \\ 0&\cdots&0 \\ 0&\cdots&0 \\ 0&\cdots&0 \\ 0&\cdots&0 \end{matrix} & \begin{matrix} \text{Continuity} \\ \text{Equations} \\ \text{for } \theta_S \end{matrix} \\
\hline
\begin{matrix} 0&0&0 \\ 0&0&0 \\ 0&0&0 \\ 0&0&0 \\ 0&0&0 \\ 0&0&0 \end{matrix} & \multicolumn{2}{c|}{\begin{matrix} G_{2,2} \\ (6\times 6) \end{matrix}} & \begin{matrix} G_{2,3} \\ (6\times 3) \end{matrix} & \begin{matrix} 0 \\ 0 \\ 0 \\ 0 \\ 0 \\ 0 \end{matrix} & \begin{matrix} G_{2,5} \\ (6\times m+1) \end{matrix} & \begin{matrix} \text{Continuity} \\ \text{Equations} \\ \text{for } \theta_L \end{matrix} \\
\hline
\begin{matrix} 0&0&0 \\ 0&0&0 \\ \vdots&\vdots&\vdots \\ 0&0&0 \end{matrix} & \multicolumn{2}{c|}{\begin{matrix} 0&0&0&0&0&0 \\ 0&0&0&0&0&0 \\ \vdots&\vdots&\vdots&\vdots&\vdots&\vdots \\ 0&0&0&0&0&0 \end{matrix}} & \begin{matrix} G_{3,3} \\ (m+2\times 3) \end{matrix} & \begin{matrix} 1 \\ 0 \\ \vdots \\ 0 \end{matrix} & \begin{matrix} G_{3,5} \\ (m+2\times m+1) \end{matrix} & \begin{matrix} \text{Coefficients} \\ \text{on } \theta^0 \cdots \theta^{2(m+1)} \text{ from} \\ \text{Contact Condition} \end{matrix}
\end{array}\right] \tag{2.5.9}
$$

$$
\{H\} = \begin{Bmatrix} 0 \\ 0 \\ 0 \\ 0 \\ 0 \\ 0 \\ 0 \\ 0 \\ 0 \\ 0 \\ 0 \\ 0 \\ -u_{r0} \\ -R-u_{r0} \\ \vdots \\ -R-u_{r0} \end{Bmatrix}, \quad \{cq\} = \begin{Bmatrix} c_2 \\ c_4 \\ c_6 \\ c_9 \\ c_{10} \\ c_{11} \\ c_{12} \\ c_{13} \\ c_{14} \\ c_{16} \\ c_{18} \\ c_{20} \\ \delta \\ q_0 \\ \vdots \\ q_m \end{Bmatrix} \quad \Rightarrow \quad \{cq\} = [G]^{-1}\{H\} \tag{2.5.10}
$$

The bifurcation angle is defined as the angle at which there is zero radial displacement relative to the inflated position of the tire, i.e.,

$$u_r^{\,T}\left(\theta_S\right) = u_{r0} \tag{2.5.11}$$

Since the amount of radial displacement is a non-linear a function of the bifurcation angle (because the integration constants and pressure coefficients are determined in terms of the bifurcation angle), it is first beneficial to obtain an idea of the magnitude of radial displacement for different bifurcation angles. Therefore, plotting $u_r^{\,T}(\theta_S) - u_{r0}$ vs. θ_S with a reasonable set of inputs gives the following plot.

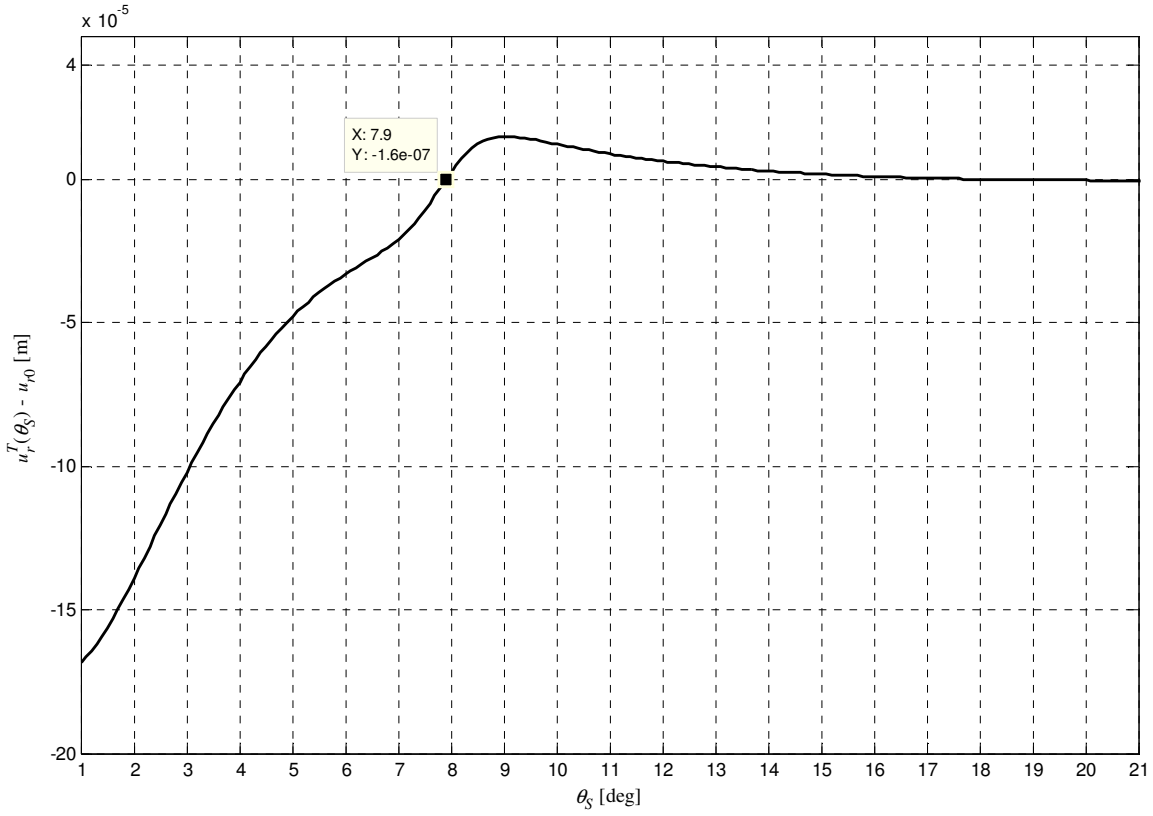

Figure 2.6. Radial deformation vs. prescribed bifurcation angles

From Figure 2.6 it is clear that, with these inputs, θ_S needs to be approximately 7.9° to satisfy (2.5.11). However, since Matlab's Symbolic Toolbox does not come with a function for finding

numerical roots of a user-defined function, a modified Brent algorithm was implemented that finds the root as follows:

1. Check that the root of the function is bracketed by the input range.
2. Evaluate the function at three points in the range (the two extremes and the midpoint).
3. Using the three points, estimate the root of the function with a quadratic approximation.
4. Determine which two of the four points bracket the root of the function.
5. Restart from Step #2 using the two new points as the input range.

Two iterations of this algorithm are illustrated in Figure 2.7.

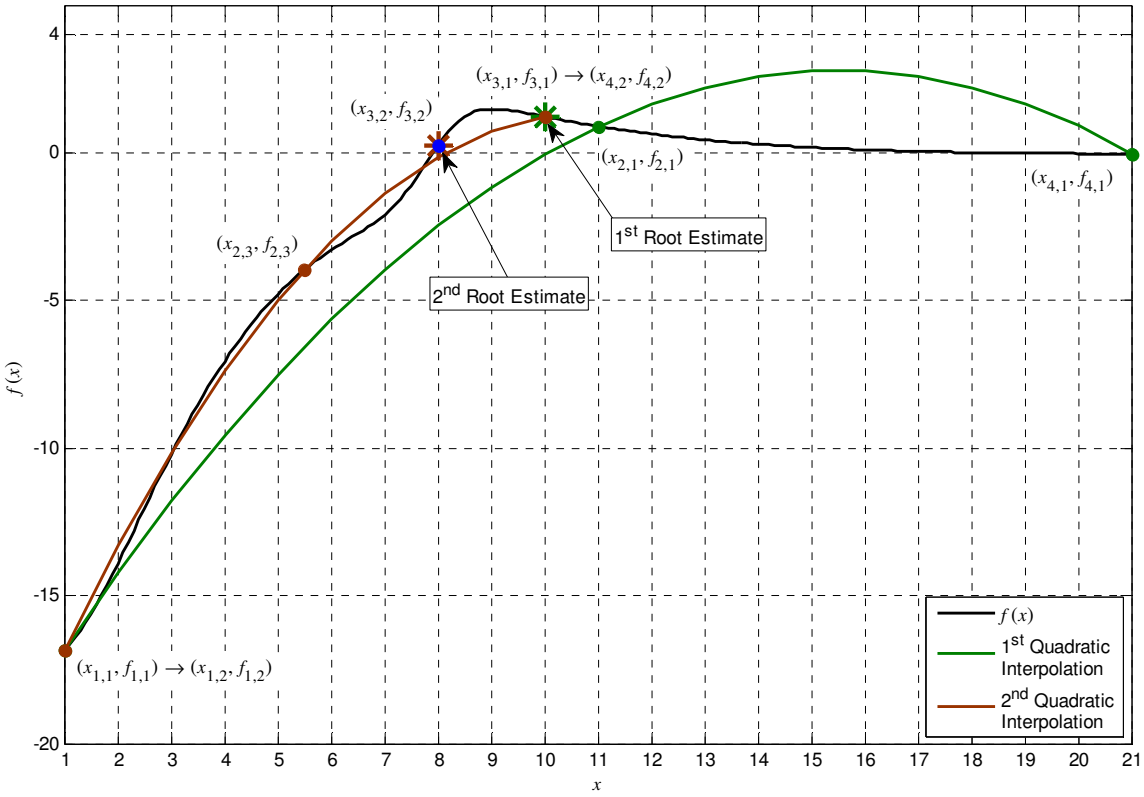

Figure 2.7. Two iterations of the root-finding algorithm

As long as there are no discontinuities in the function, the algorithm can converge reliably and quickly to the correct root.

2.6. Accounting for Non-linear Geometry

Obtaining the solution described above gives the straightforward linear solution to the problem. However, when this is done within a linear context, the normal force in the belts can introduce considerable error, especially for non-zero inflation pressures, since this increases the normal force. This can be observed by calculating the sum of the forces on the contact region. The loads on the contact region are depicted in the Figure 2.8.

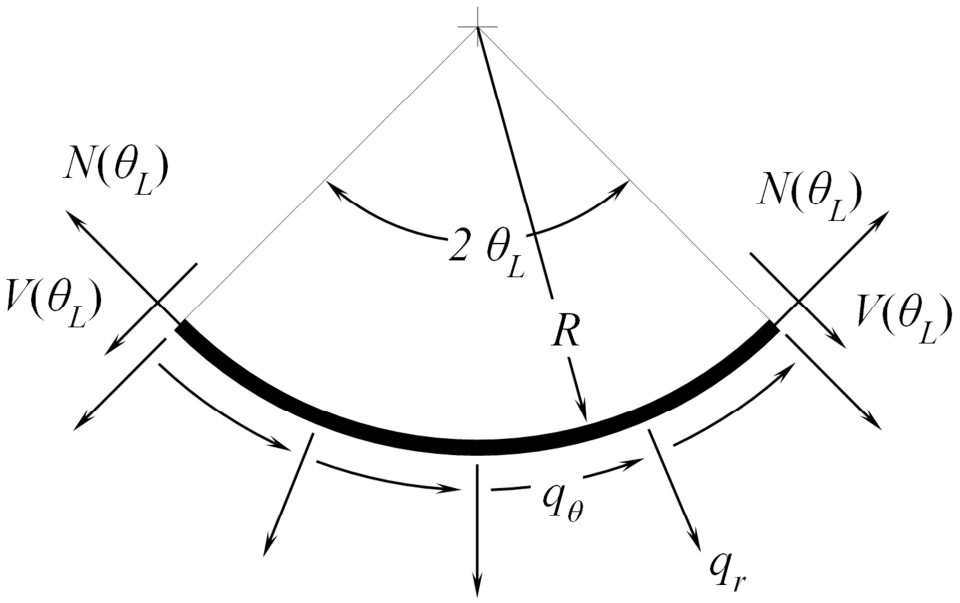

Figure 2.8. Contact region loads

The sum of the forces in the vertical direction on this section of the tire is therefore given by

$$+\uparrow \sum F_y = 0 = -F_r + F_\theta + 2N(\theta_L)\sin(\theta_L) - 2V(\theta_L)\cos(\theta_L) \tag{2.5.12}$$

where the radial load, F_r, and the circumferential load, F_θ, are calculated using (2.5.13).

$$\begin{aligned} F_r &= 2\int_0^{\theta_L} Rbq_r \cos(\theta)\,d\theta \\ F_\theta &= 2\int_0^{\theta_L} Rbq_\theta \sin(\theta)\,d\theta \end{aligned} \tag{2.5.13}$$

When the magnitude of the four force terms is compared for contact angles between 0 and 20 degrees, Figure 2.9 is obtained.

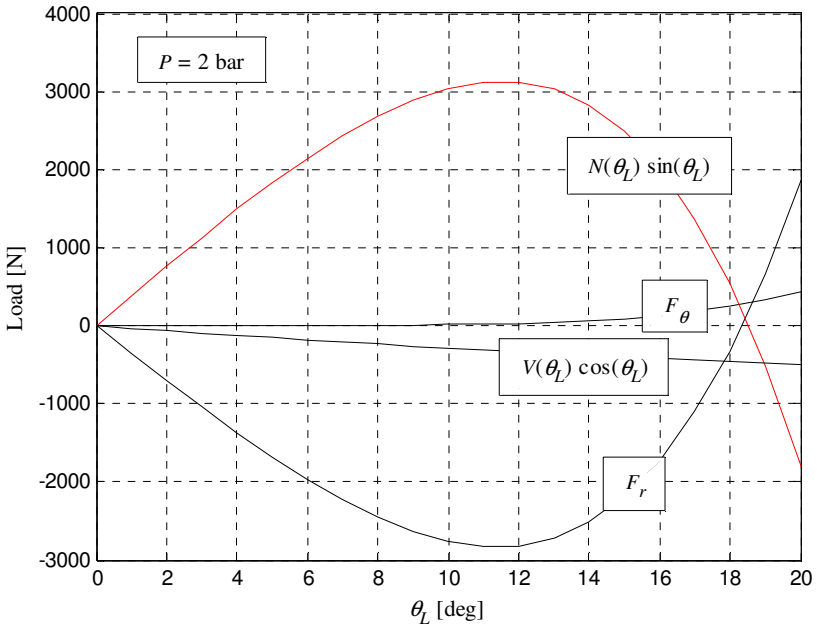

(a)

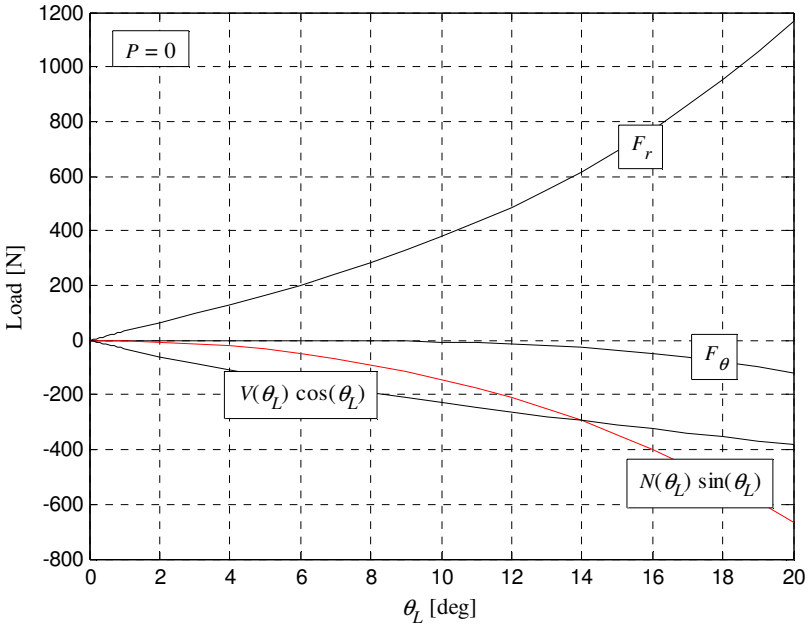

(b)

Figure 2.9. Vertical loads on the contact region for $P = 2$ bar (a) and 0 (b)

The results of Figure 2.9 show how the term coming from the normal force is excessively large in the linear theory. If large deformations were taken into account, the contribution from this term would be horizontal due to the large rotation at the edge of contact and the normal force would not contribute to vertical force equilibrium. As indicated in Figure 2.9, as the pressure increases the normal force in the belts of the tire increases, which increases the incorrect influence of this effect. This normal force can be easily approximated (neglecting the sidewall effect) using Figure 2.10.

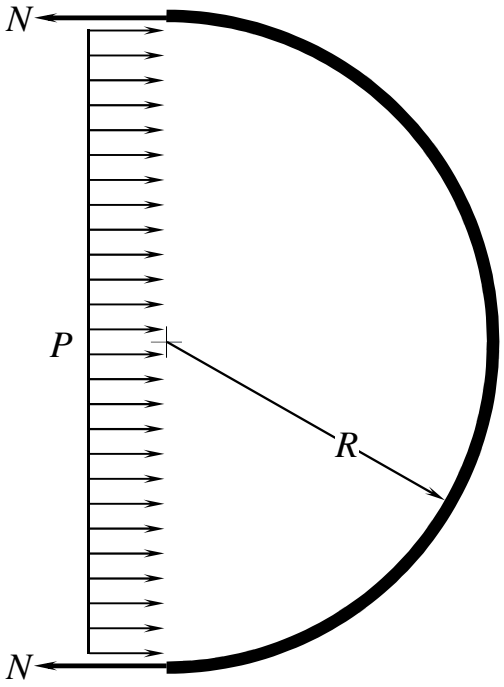

Figure 2.10. Normal force due to inflation pressure

Summing the forces in the horizontal direction in this figure gives

$$\underset{\rightarrow}{+}\sum F_x = 0 = 2RbP - 2N \Rightarrow N = RbP \tag{2.5.14}$$

Using dimensions of a standard reference tire and a typical inflation pressure, the normal force is then calculated to be

$$\left.\begin{array}{l} R = 326.3\,\mathrm{mm} \\ b = 182.9\,\mathrm{mm} \\ P = 2\,\mathrm{bar} \end{array}\right\} \Rightarrow N = 11.9\,\mathrm{kN} \tag{2.5.15}$$

In order to determine the location where a large normal force and a large rotation coincide in the tire, the normal force and cross-sectional rotation are plotted for a parameter set representing a normal tire.

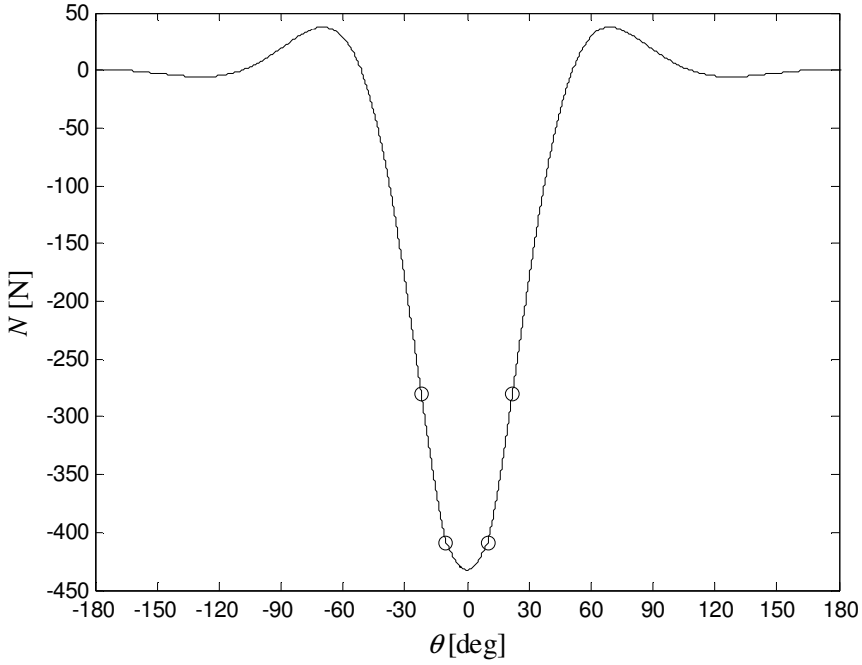

(a)

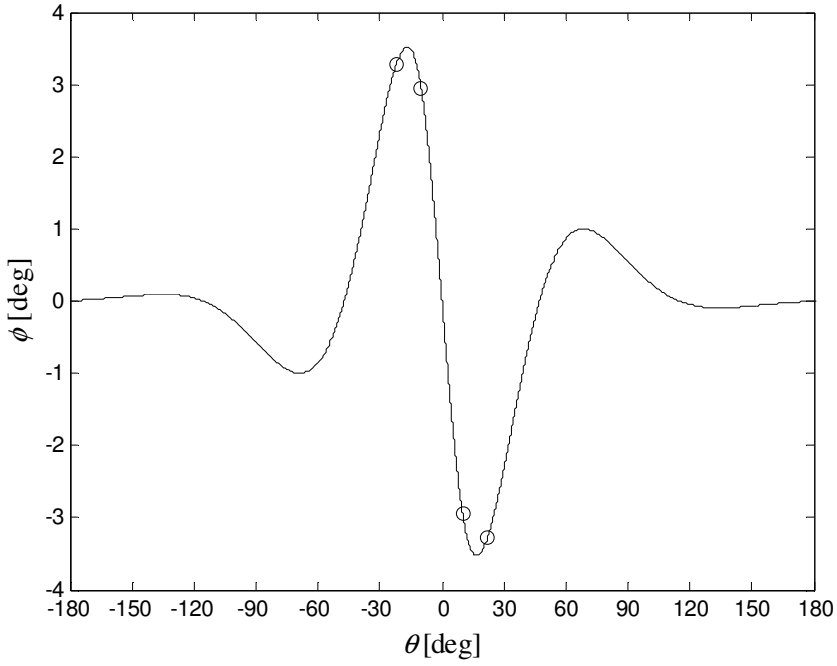

(b)

Figure 2.11. Normal force (a) and cross-sectional rotation (b)

The results in Figure 2.11 show that the normal force at the edge of contact is a maximum value and it occurs near the point of maximum rotation. As such, this will produce the most error in the geometrically linear solution. Therefore, it is proposed that an inflation pressure can be chosen that minimizes the error due to deformation in the linear solution of the tire. Since the primary motivation for using this inflation pressure is to obtain the correct magnitude of the load, Figure 2.8 shows that the inflation pressure that allows the most accuracy in the linear solution of the tire corresponds to the pressure that causes the normal force to be zero at the edge of contact. Figure 2.12 shows the relationship between the normal force in the belts and the inflation pressure for two contact angles. This plot shows that the best choice of a pressure is relatively small.

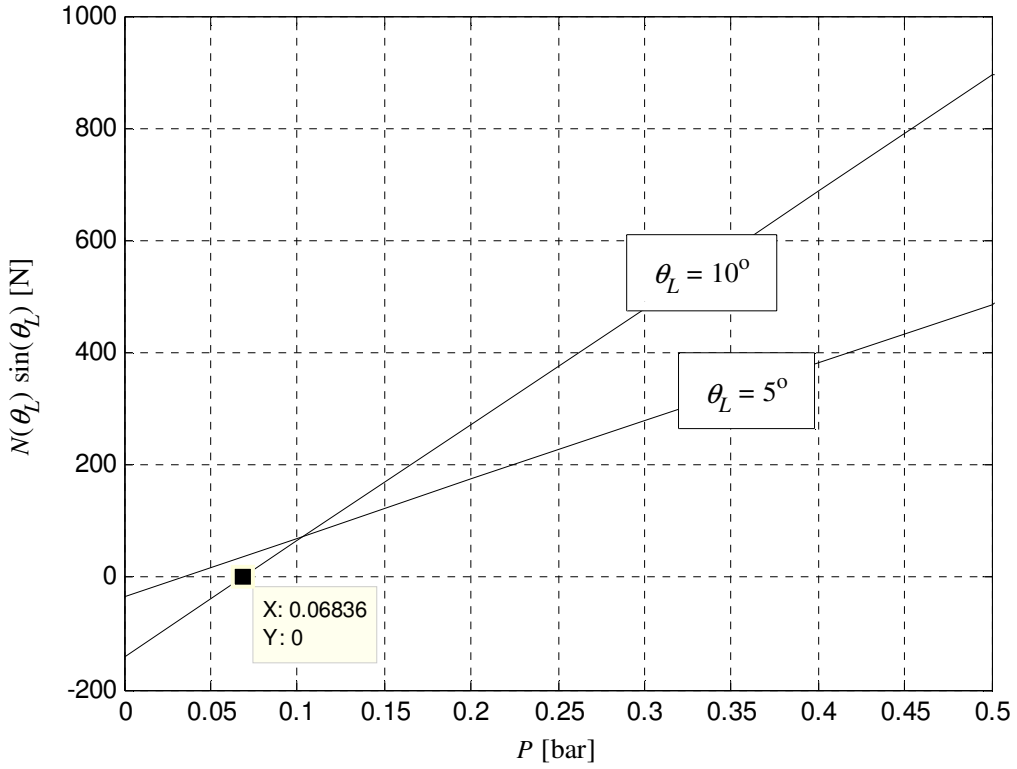

Figure 2.12. Normal force at the edge of contact for various inflation pressures and contact angles

From this figure, it is clear that the inflation pressure that produces zero normal force at the edge of contact for a given contact angle can be quickly and easily calculated as along as the normal force at the edge of contact is already known for two distinct inflation pressures.

In order to obtain the solution for inflation pressures other than P^*, the following solution procedure is followed:

1. Calculate the inflation pressure solution (i.e. $F = 0$) for an inflation pressure of $P - P^*$
2. Calculate the linear solution for the loaded tire for an inflation pressure of P^* with inputs calculated based on an inflation pressure of P

3. Obtain the full solution by adding the linear solution obtained in Step 2 to the non-linear inextensible membrane solution for an inflation pressure of $P - P^*$

Note that Step 3 only effects N and q_g, which means that it is assumes that any change in the solution for a loaded tire as it is inflated is entirely due to membrane behavior (i.e. stiffening of the sidewall, increase of the load at a given contact angle, etc.). While it is true that there would be some change in the internal moment and rotation of the belts at the edge of contact, it is believed that these effects are negligible for a typical tire. The accuracy that results from this linear model will be determined by comparing it to a non-linear finite element model in Chapter 3.

WORKS CITED

[1] F. Koutný, Geometry and Mechanics of Pneumatic Tires, Zlín, 1997.

[2] A. Gasmi, P. F. Joseph, T. B. Rhyne and S. M. Cron, "Closed-Form Solution of a Shear Deformable, Extensional Ring in Contact Between Two Rigid Surfaces," *International Journal of Solids and Structures,* vol. 48, no. 5, p. 843–853, March 2011.

CHAPTER 3
–
VALIDATION

3.1. Introduction

When the numerical solution is found using the procedure described in Chapter 2, it is necessary to ensure that the governing differential equations, as well as the symmetry, continuity, contact, and spoke angle equations are being satisfied. Evidence that these equations are being satisfied is given in the following sections.

3.2. Parameter Specification

Being able to determine the parameters that represent an actual tire is important for two reasons. First, without knowing how to determine what parameters allow the model to reproduce the behavior of the actual tire, it is impossible to confirm that the two-dimensional model accurately represents the behavior of the three dimensional tire. Second, the purpose of the model is to predict analytically the behavior of an actual tire to assist in the design and selection of its stiffness parameters. This can only be accomplished if the parameters that relate the model to a physical tire can be determined.

The radius and width of the tire can be easily found from the tire's size specification, and vehicle manufacturers typically specify that the tires should be inflated to approximately 2 bars (or 200 kPa) of inflation pressure.

The values used for EA, EI, and GA were provided by Dr. Tim Rhyne from the Michelin Americas Research and Development Corporation (MARC).

All the parameters describing the sidewall should be determined by finding values that allow the model to match experimental data provided by Michelin© for the load vs. deflection, load vs. counter-deflection, inflation pressure vs. expansion, and torque vs. rotation. Currently, the parameters that most closely approximate the experimental data for inflation pressures of both 0 and 2 bar are compared in Table 3.1. A more detailed explanation of how close these parameters approximate the experimental data is given in Section 3.5.

Table 3.1. Pneumatic tire base-case parameters

Parameter	$P = 0$	$P = 2$ bar	Units	Description
θ_L	10	10	deg	Contact Angle
m	12	12	Unitless	Precision
EA	8×10^5	1×10^7	N	Extensional Belt Stiffness
EI	15	6	N m^2	Bending Belt Stiffness
GA	923.45	800	N	Shear Belt Stiffness
K_θ	6.82×10^5	6×10^4	Pa	Circumferential Carcass Stiffness
K_r^T	1×10^5	1×10^5	Pa	Radial Carcass Stiffness in Tension
K_r^C	0	0	Pa	Radial Carcass Stiffness in Compression
F_P	0	0	N / m	Pre-tensioning Sensitivity
P	0	2	bar	Air Pressure
R	326.3	326.3	mm	Tire Outer Radius
b	182.9	182.9	mm	Tire Width

3.3. Numerical Validation

In this section four different aspects of the structural part of the pneumatic tire solution procedure are validated. These aspects include satisfaction of the governing equations, validation of the model for the case of a non-pneumatic tire, a presentation of results that show the overall symmetry and continuity of the solution is correct, and convergence of the pressure approximation. Unless otherwise noted, the results shown here are for the parameter set that allows the experimental data to be matched for an inflation pressure of 2 bar. The conclusions

concerning the accuracy of the model are the same no matter which set of parameters is used. The non-linear effects introduced at the end of Chapter 2 are validated in Section 3.4.

3.3.1. Governing Differential Equations

The purpose of this section is to validate mathematically that the governing differential equations for the belt have been satisfied for all values of the angular coordinate. This validation has nothing to do with the superposition procedure introduced at the end of Chapter 2. Rather, it focuses on the linear solution that accounts for the structural effects of the tire. The governing differential equations can be written in terms of both the forces and moments and the displacements in the belt of the tire as follows:

$$\left.\begin{aligned} &EA\frac{d^2u_{\theta 0}}{d\theta^2} - GAu_{\theta 0} + \left(EA+GA\right)\frac{du_r}{d\theta} + RGA\phi = -R^2\, b\, q_\theta \\ &-GA\frac{d^2u_r}{d\theta^2} + EAu_r + \left(EA+GA\right)\frac{du_{\theta 0}}{d\theta} - RGA\frac{d\phi}{d\theta} = R^2\, b\, q_r \\ &EI\frac{d^2\phi}{d\theta^2} - R^2GA\phi - RGA\frac{du_r}{d\theta} + RGAu_{\theta 0} = 0 \end{aligned}\right\} \Leftrightarrow \begin{cases} \dfrac{d\,N}{d\theta} + V = -R^2\, b\, q_\theta \\ N - \dfrac{d\,V}{d\theta} = R^2\, b\, q_r \\ \dfrac{d\,M}{d\theta} - RV = 0 \end{cases} \tag{3.2.1}$$

Moving all the right-hand sides of (3.2.1) to the left-hand side and plotting the results, which should be zero if the equations are satisfied, produces the following plots for the three regions.

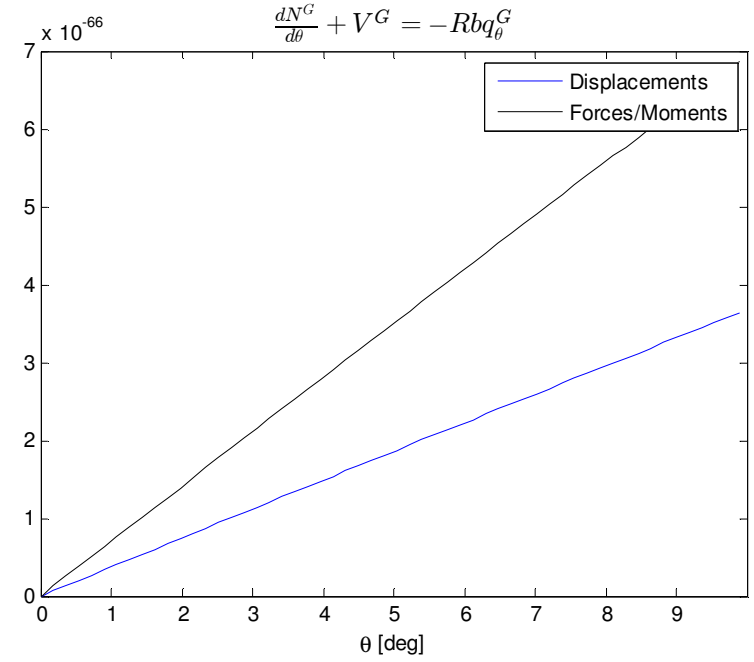
$\frac{dN^G}{d\theta} + V^G = -Rbq_\theta^G$
x 10^-66
Displacements
Forces/Moments
θ [deg]

(a)

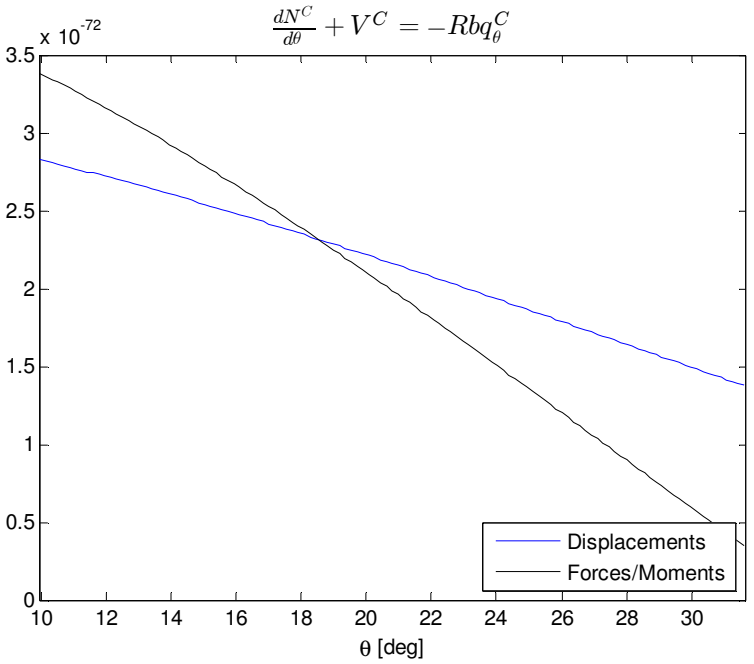
$\frac{dN^C}{d\theta} + V^C = -Rbq_\theta^C$
x 10^-72
Displacements
Forces/Moments
θ [deg]

(b)

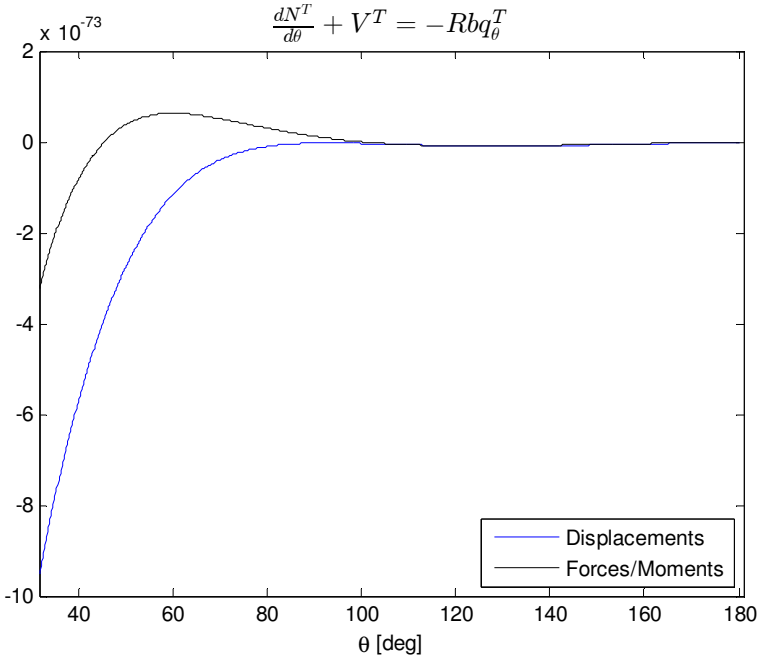

(c)

Figure 3.1. The first governing differential equation for the (a) contact, (b) compression-support, and (c) tension-support regions

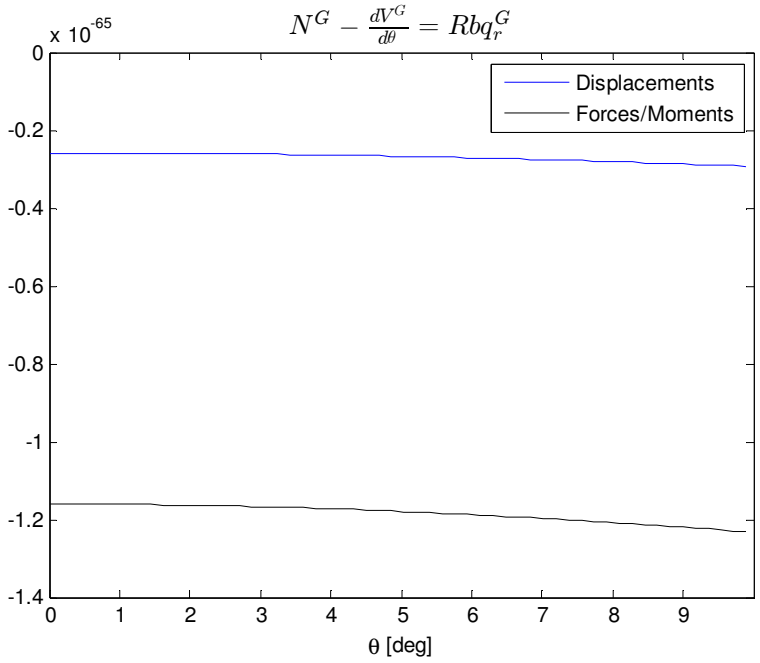

(a)

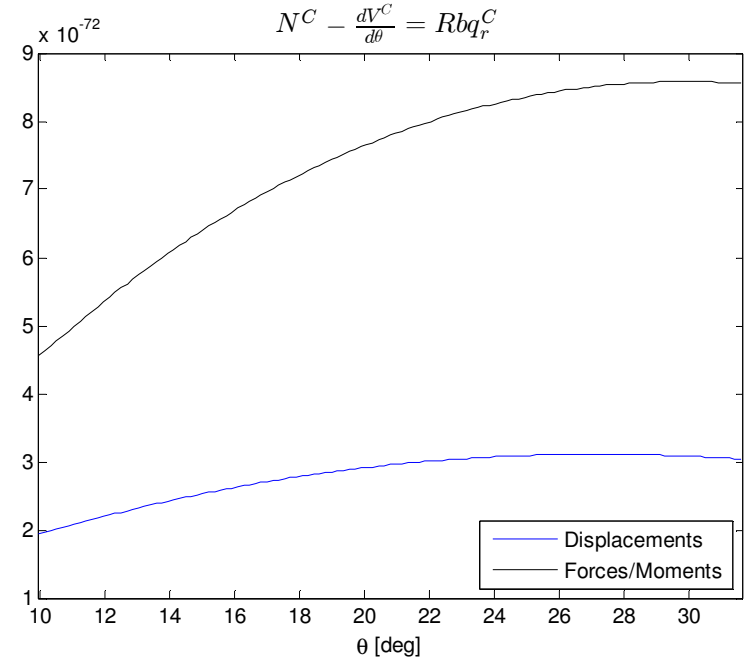

(b)

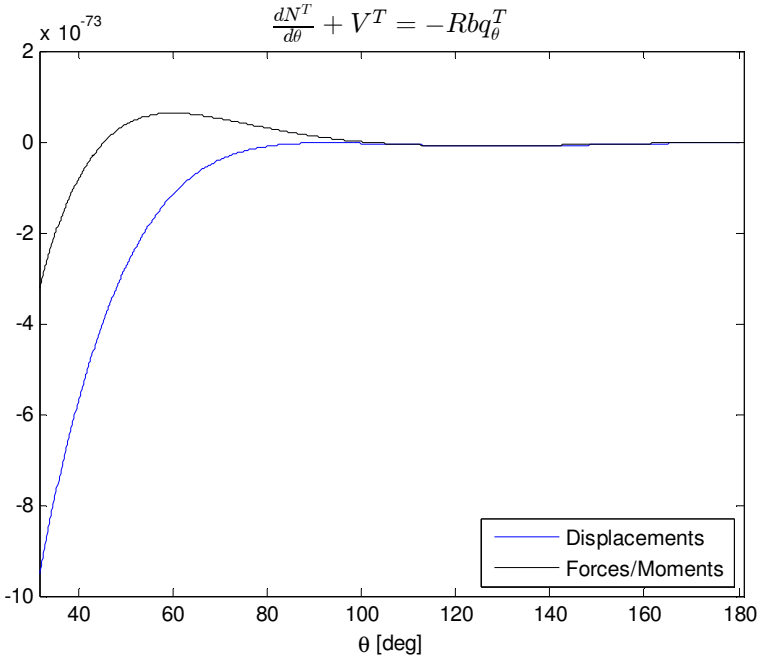

(c)

Figure 3.2. The second governing differential equation for the (a) contact, (b) compression-support, and (c) tension-support regions

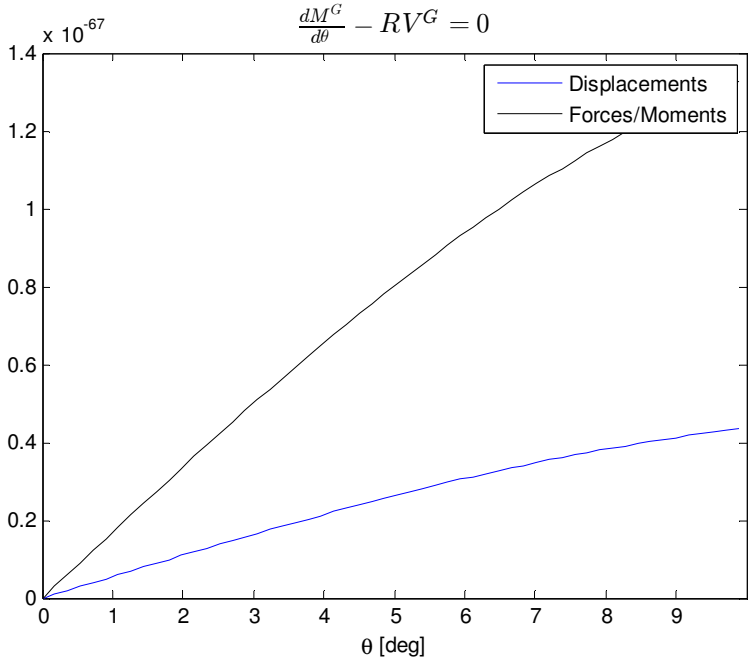
$\frac{dM^G}{d\theta} - RV^G = 0$
x 10^-67
1.4
1.2
1
0.8
0.6
0.4
0.2
0
0 1 2 3 4 5 6 7 8 9
θ [deg]
Displacements
Forces/Moments

(a)

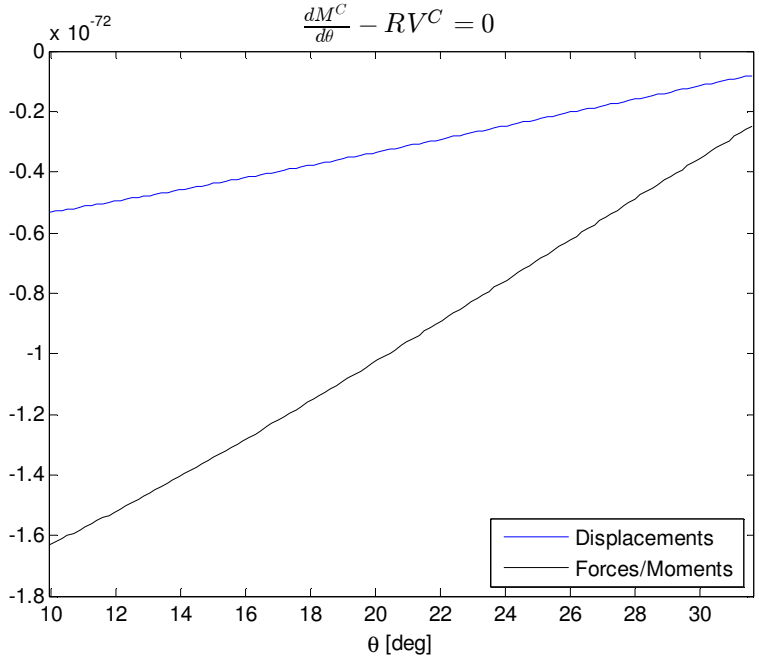
$\frac{dM^C}{d\theta} - RV^C = 0$
x 10^-72
0
-0.2
-0.4
-0.6
-0.8
-1
-1.2
-1.4
-1.6
-1.8
10 12 14 16 18 20 22 24 26 28 30
θ [deg]
Displacements
Forces/Moments

(b)

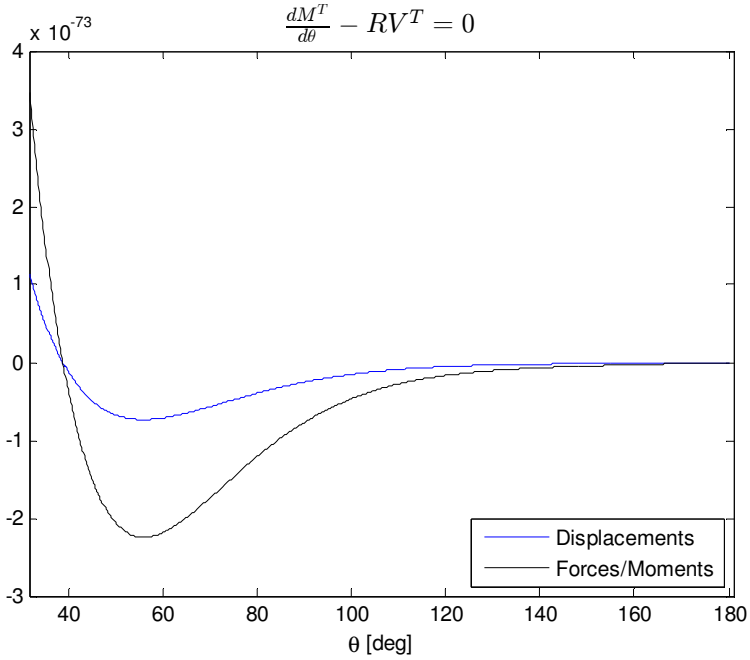

(c)

Figure 3.3. The third governing differential equation for the (a) contact, (b) compression-support, and (c) tension-support regions

Because all the calculations done to produce the above plots were done while carrying 70 digits of precision, it seems apparent that all the governing differential equations are being satisfied. The reason for the greater amount of error in the plots of the differential equations in the contact region is due to the larger numbers existing in the calculations from the contact pressure in that region. The scale on the plots for the contact region generally is always about 10^7 greater than the scale on the plots for the non-contact regions no matter how high of a precision was used in the calculations.

3.3.2. Non-pneumatic Tire Comparison

The results in the previous section show that the mathematical equations are satisfied. In this section the solution obtained by Gasmi, et al. [1] for a non-pneumatic tire can be used to provide a higher level validation, since the non-pneumatic tire in that study is a special case of

the pneumatic tire in this study. The principal differences are the pressure and the circumferential stiffness. While it is a simple matter to use a pressure of zero, it is nontrivial to use a very small circumferential stiffness since this significantly changes the decoupled governing differential equations. The parameters that define the base-case non-pneumatic tire studied by Gasmi, et al. [1], are shown in Table 3.2.

Table 3.2. Non-pneumatic tire parameters

Parameter	Tire Model	Tweel Model	Units	Description
θ_L	10	10	deg	Contact Angle
m	12	12	Unitless	Precision
EA	9×10^6	9×10^6	N	Extensional Belt Stiffness
EI	168.75	168.75	N m^2	Bending Belt Stiffness
GA	3,600	3,600	N	Shear Belt Stiffness
K_θ	Varies	0	Pa	Circumferential Carcass Stiffness
K_r^T	1×10^6	1×10^6	Pa	Radial Carcass Stiffness in Tension
K_r^C	0	0	Pa	Radial Carcass Stiffness in Compression
F_P	0	0	N / m	Pre-tensioning Sensitivity
P	0	0	Pa	Air Pressure
R	200	200	mm	Tire Outer Radius
b	60	60	mm	Tire Width

The comparison between the two models is shown in Figure 3.4 for the radial deformation and the contact pressure profile.

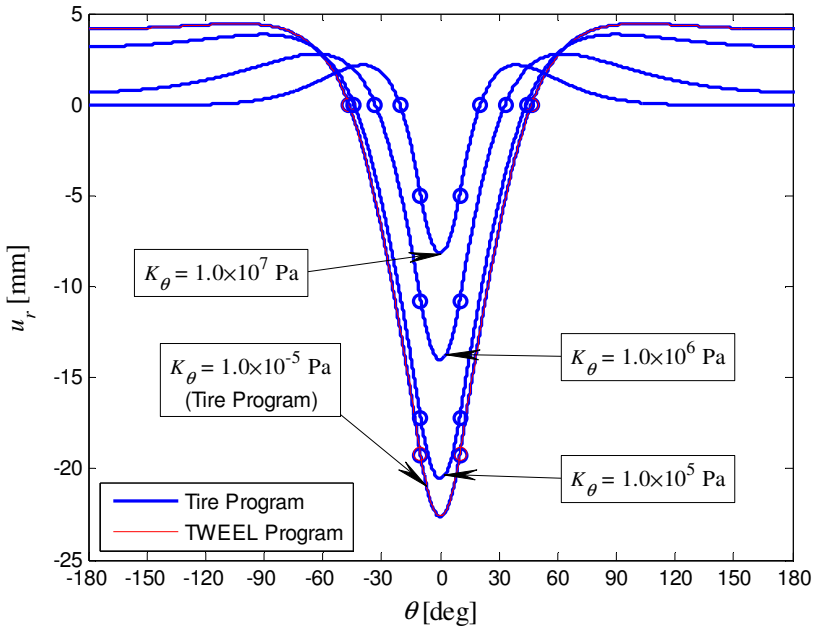

(a)

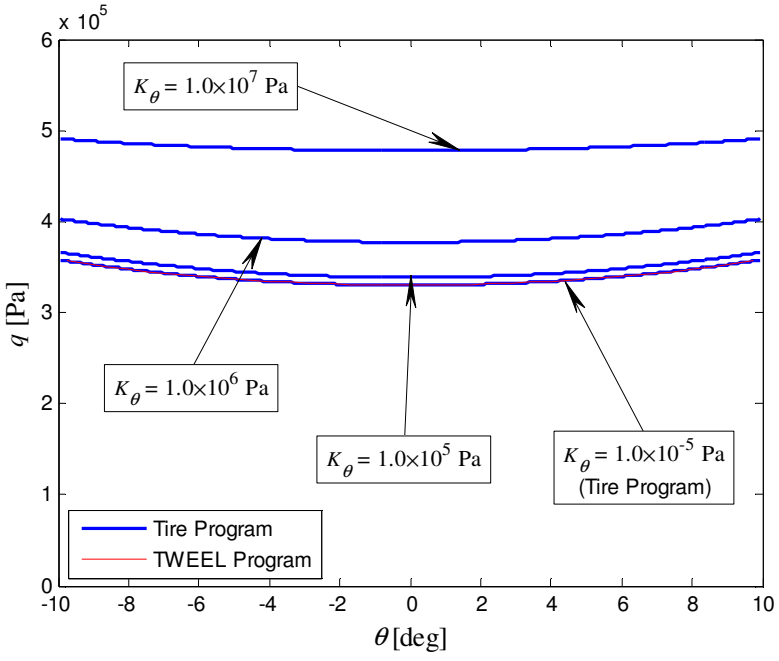

(b)

Figure 3.4. The radial deformation (a) and contact pressure profile (b) for several values of K_θ compared to the non-pneumatic tire (Tweel) model

The convergence of the current model to the non-pneumatic tire results confirms that the governing differential equations have been decoupled and solved correctly in this important limiting case.

3.3.3. Symmetry and Continuity of the Pneumatic Tire Solution

The symmetry of the pneumatic tire solution associated with the data in Table 3.1 and its continuity at the boundaries can be easily seen in the plot of the deformed shape shown below.

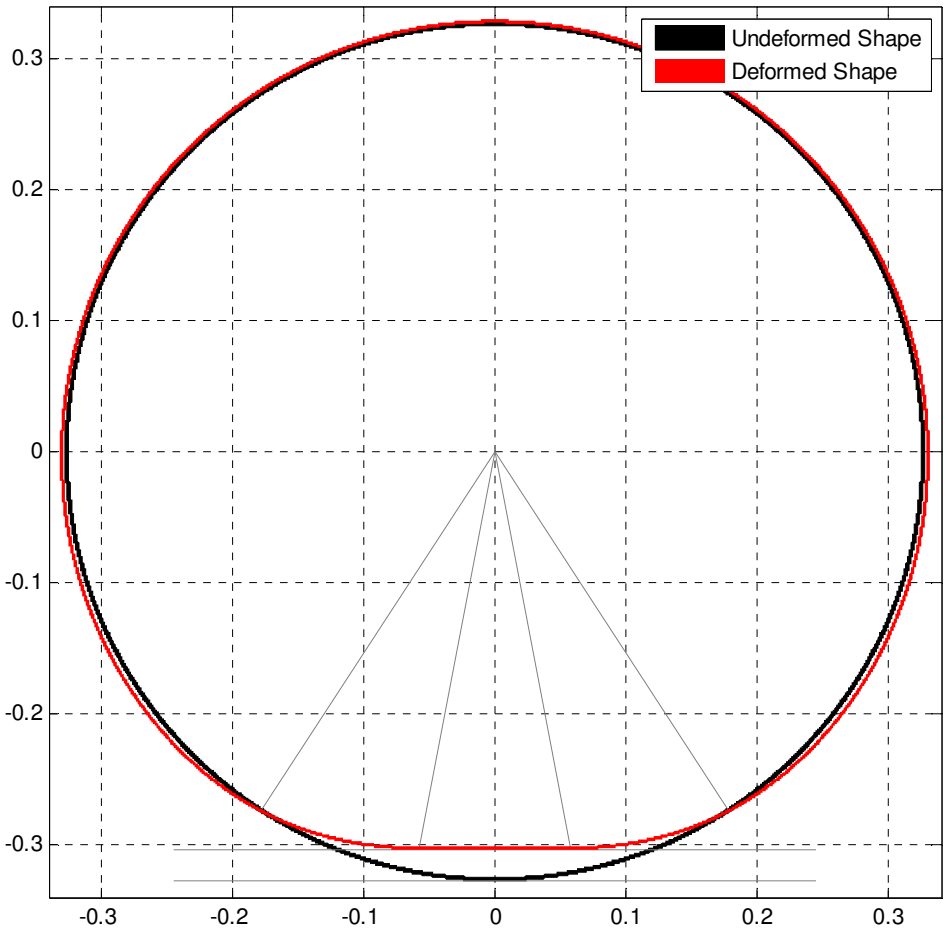

Figure 3.5. The deformed shape of the tire

This is evidenced further when the deformation, forces, and moments are plotted. Plots of the deformations are shown in Figure 3.6.

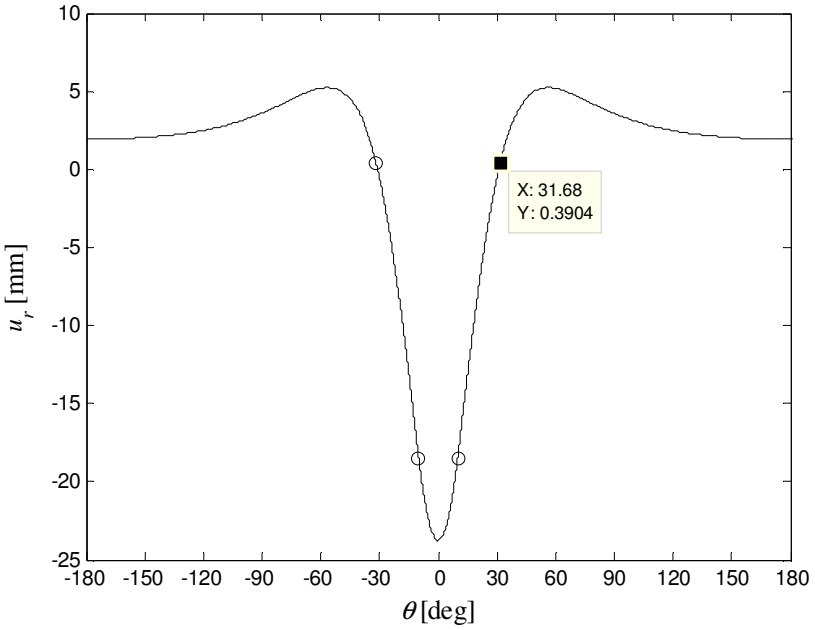

(a)

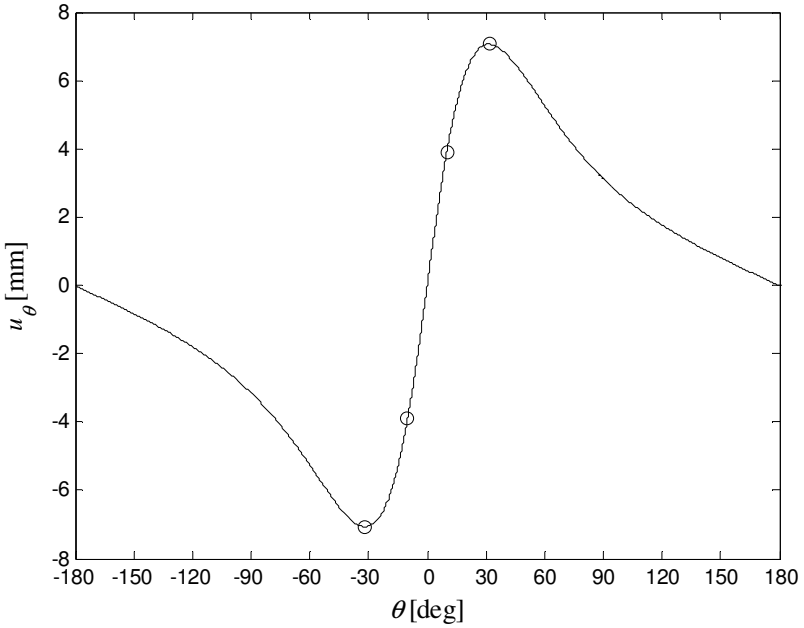

(b)

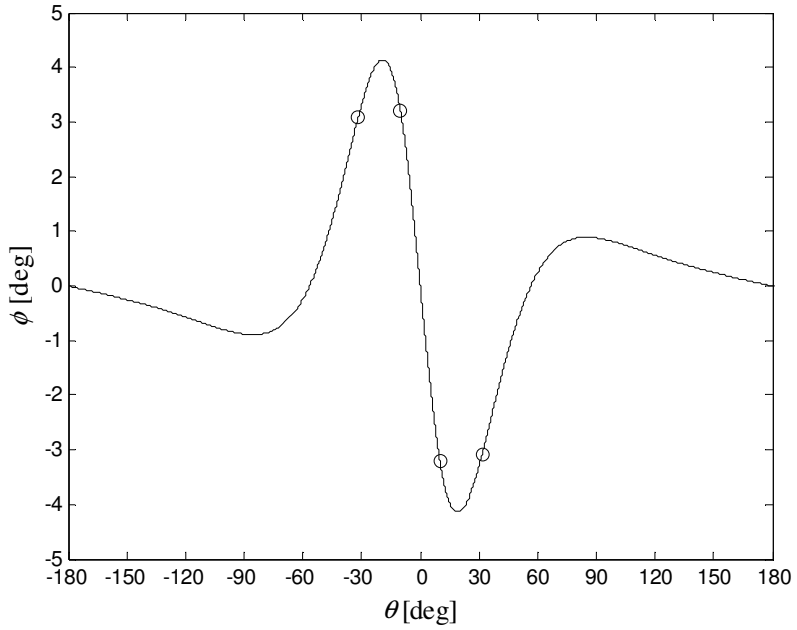

(c)

Figure 3.6. The radial (a) and circumferential (b) deformations and the cross-sectional rotation (c) in the tire

The plots above show that the displacements are C^1 continuous. Additionally, the plot of the radial deformation shows that, with the set of inputs used, the bifurcation angle is 31.68° and the radial displacement at the bifurcation angle is $0.3904\ \text{mm}$. When the amount of expansion due to the air pressure is subtracted from the radial displacement at the bifurcation angle with the full number of available digits, the difference is $5.626\ \text{nm}$. It is believed that this precision is entirely sufficient to model the tire accurately.

Plots of the forces and moments in the tire are shown in Figure 3.7.

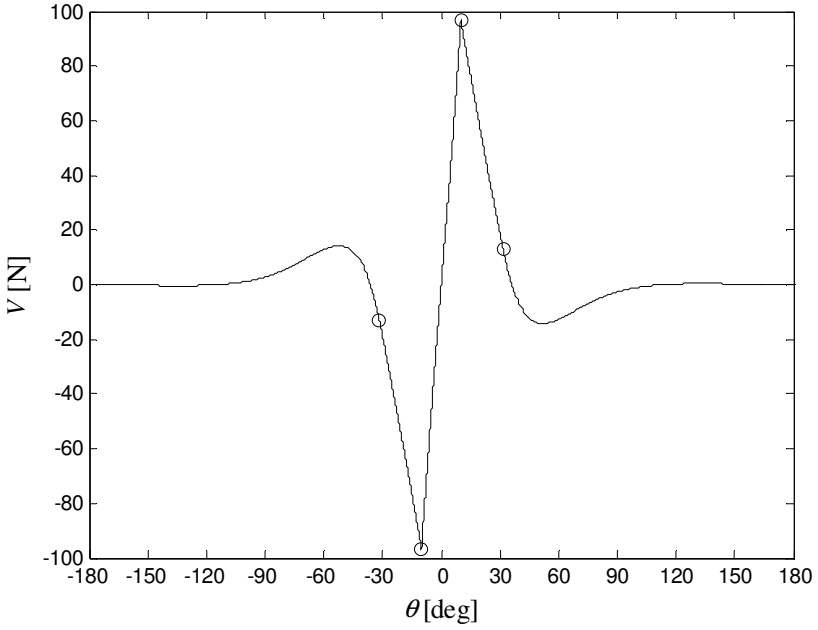
100
80
60
40
20
0
-20
-40
-60
-80
-100
V [N]
-180 -150 -120 -90 -60 -30 0 30 60 90 120 150 180
θ [deg]

(a)

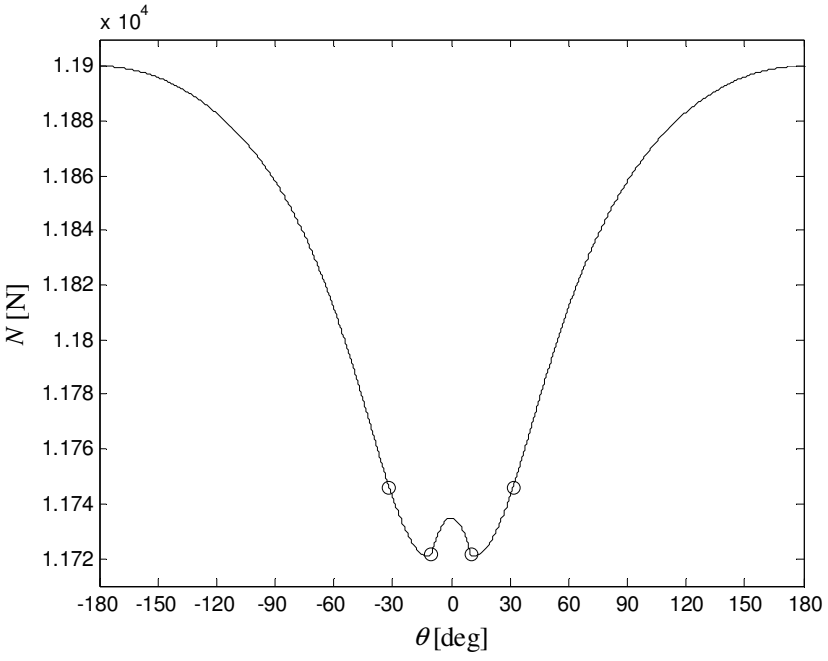
x 10^4
1.19
1.188
1.186
1.184
1.182
1.18
1.178
1.176
1.174
1.172
N [N]
-180 -150 -120 -90 -60 -30 0 30 60 90 120 150 180
θ [deg]

(b)

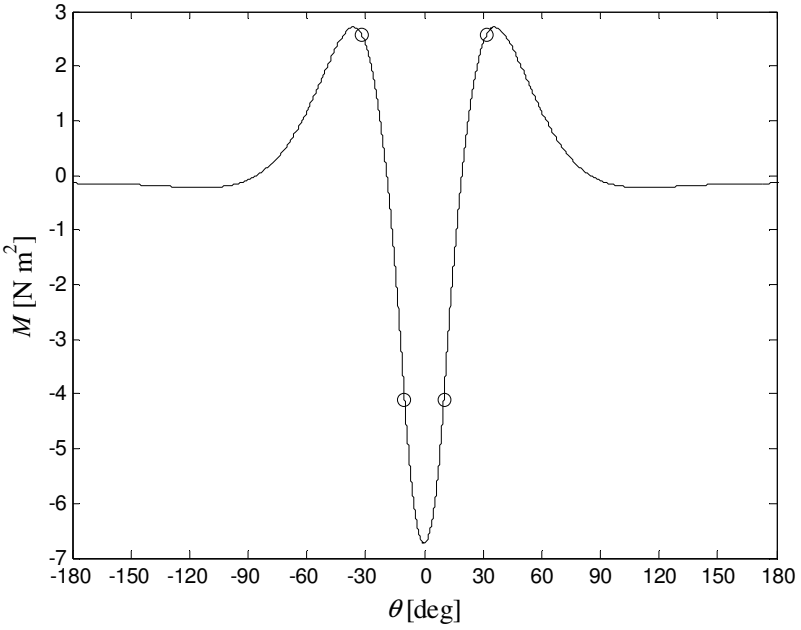

(c)

Figure 3.7. The shear (a) and normal (b) forces and the internal moment (c) in the tire

The plots above show that the forces and moments are C^0 continuous. Additionally, the normal force at the edge of contact in Figure 3.7b includes the superposition effect from the inflation pressure. Since the structural part of the problem required that $N(\theta_L) = 0$, which was satisfied to very high accuracy (~10^{-69}), the value of the normal force at the edge of contact in this figure corresponds to the effect of inflation pressure only.

3.3.4. Convergence with Respect to *m*

In the contact region ($-\theta_L \le \theta \le \theta_L$), the solution shown in Chapter 2 was derived in relation to the number of terms used in contact pressure profile, m. Because this number determines the precision of the results, it is essential to both confirm that the solution converges as m increases and to determine what value of m yields a converged solution. Three relationships quantify this convergence, namely, the contact condition itself, the curvature of

the tire in the contact region, and the contact pressure. In order to characterize these aspects adequately, plots are first qualitatively compared for various selected values of m to obtain an idea of the general behavior, and then a single characteristic value is plotted as m changes.

For these results, because the method to account for non-linear behavior described in Chapter 2 requires that certain aspects of the tire's behavior be modified from what is predicted, convergence of the solution can only be observed before this modification occurs.

3.3.4.1. Contact Condition

The contact condition was given in Chapter 2 as

$$v(\theta) = \delta - R\left(1-\cos(\theta)\right) = u_{\theta 0}\sin(\theta) - u_r\cos(\theta) \tag{3.5.1}$$

The left-hand side of (3.5.1) is known to be the exact displacement of the tire in the contact region, while the right-hand side is an approximation due to the approximation of the contact pressure profile. Therefore, the absolute value of the difference quantifies how precise the result is. When this difference is plotted as a function of θ, the result generally looks like those presented in Figure 3.8 for all values of m.

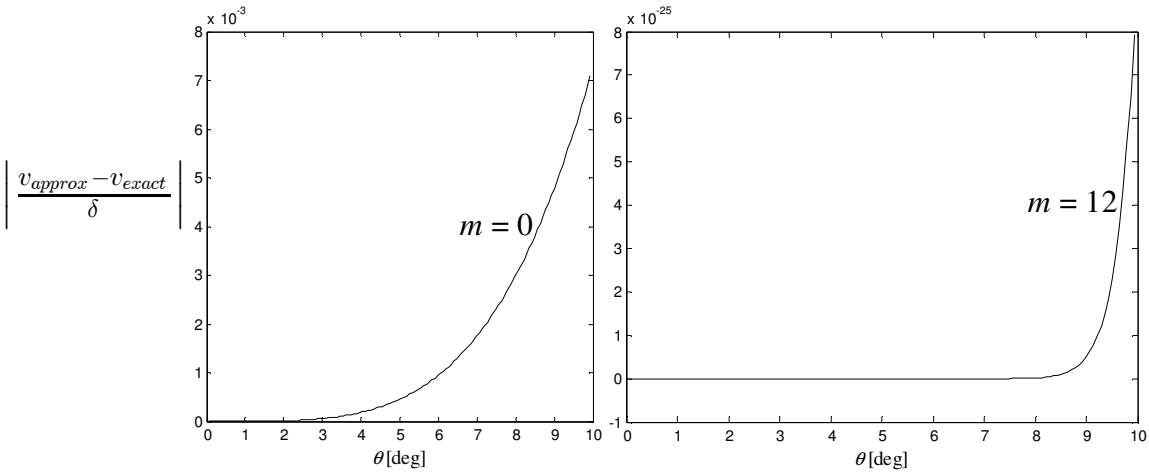

Figure 3.8. Relative error of the contact condition

Qualitatively, it is noted that the maximum error is at the edge of contact and that the values can be extremely small. Therefore, it is concluded that a good representation of the relationship between m and the relative error can be obtained by plotting the relationship between the maximum relative error and the value of m on a logarithmic vertical scale. Figure 3.9 shows this.

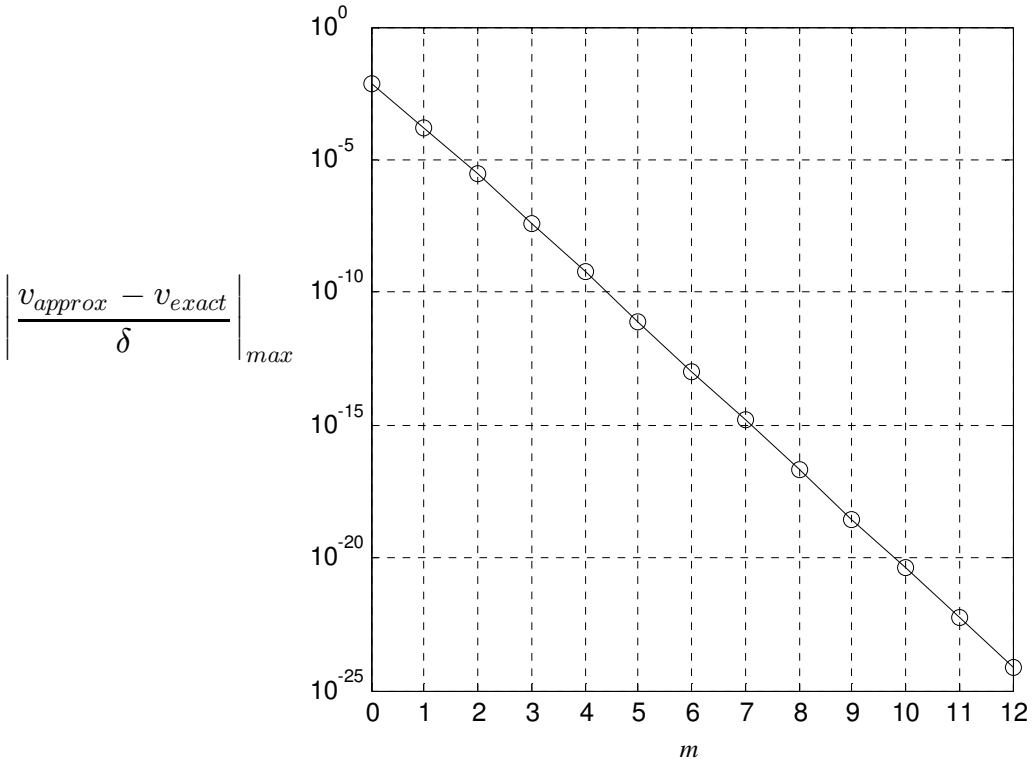

Figure 3.9. Maximum relative error in contact condition vs. *m*

Therefore, it is clear that convergence is observed in the contact condition, although it is impossible to determine how many terms are needed in order to obtain a "converged" solution. The following additional plots show how the necessary number of terms may be determined.

3.3.4.2. Curvature in the Contact Region

In order to satisfy the contact condition, the contact region is required to be flat. Therefore, quantifying how flat it actually is provides one more means of checking the precision of the results. This can be accomplished by plotting the curvature of the tire in the contact region which would be zero if the region were indeed flat.

Parametric equations of the deformed shape of the tire can be derived from Figure 2.4 as

$$\begin{aligned} x(\theta) &= \left(R + u_r(\theta)\right)\cos(\theta) - u_{\theta 0}(\theta)\sin(\theta) \\ y(\theta) &= \left(R + u_r(\theta)\right)\sin(\theta) + u_{\theta 0}(\theta)\cos(\theta) \end{aligned} \tag{3.5.2}$$

The curvature, κ, can be easily found using the typical curvature equation for a parametric curve given by

$$\kappa = \frac{\dot{x}\,\ddot{y} - \dot{y}\,\ddot{x}}{\left(\dot{x}^2 + \dot{y}^2\right)^{3/2}} \tag{3.5.3}$$

where

$$\dot{x} = \frac{dx}{d\theta} \text{ and } \ddot{x} = \frac{d^2x}{d\theta^2} \tag{3.5.4}$$

Plotting (3.5.3) in the contact region for $m = 0$ and 12 produces Figure 3.10.

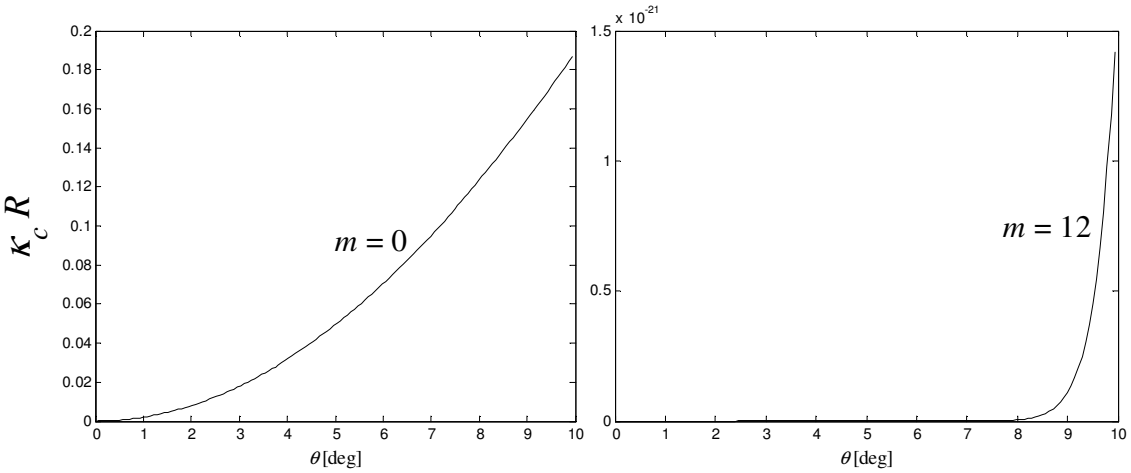

Figure 3.10. Relative curvature in the contact region for $m = 0$ and 12

These plots qualitatively show that the curvature of the tire does converge to zero as m increases. In order to examine the convergence more closely, the maximum relative curvature is plotted as m increases.

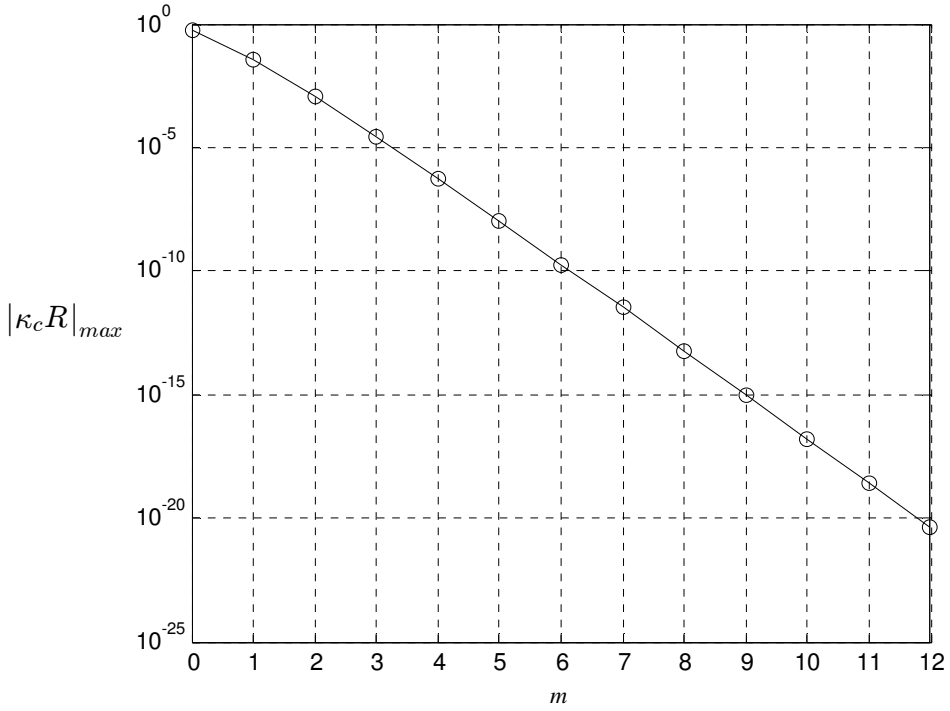

Figure 3.11. Maximum relative curvature vs. m

From this plot, it is apparent that the solution steadily converges to zero as m increases.

3.3.4.3. Contact Pressure

The expression in Chapter 2 that was used to represent the contact pressure was

$$q_g(\theta) = \sum_{n=0}^{m} q_n \cos(n\theta) \tag{3.5.5}$$

As more terms are used in the Taylor series expansion of the contact condition, more pressure coefficients can be used to describe the contact pressure profile. Therefore, using more terms from the expansion allows a more complicated contact pressure profile to be represented.

Plotting (3.5.5) for different values of m produces Figure 3.12, which shows that with the inputs used in this study, the contact pressure profile has pretty much converged when more than 8 terms ($m = 7$) have been used.

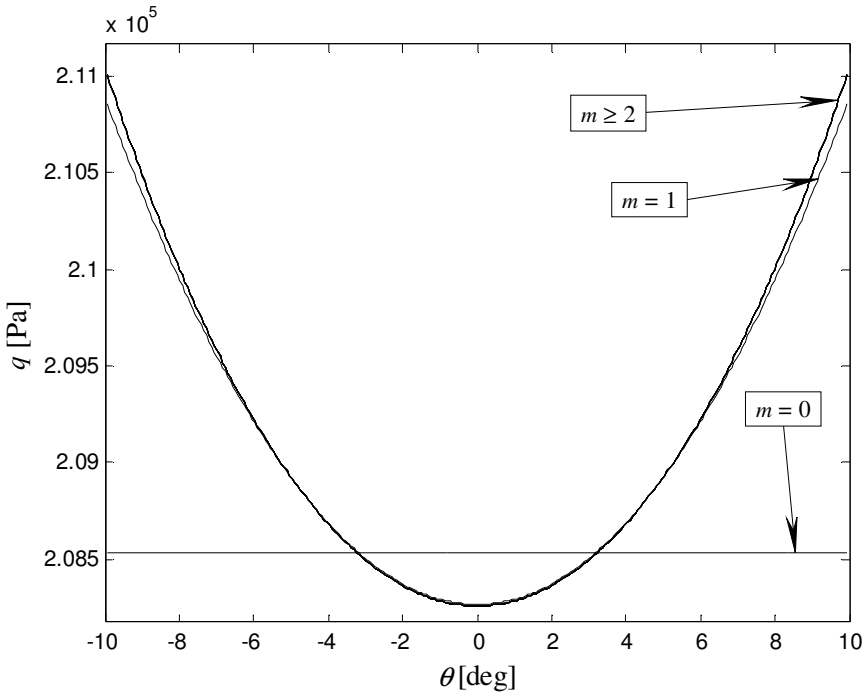

Figure 3.12. Contact pressure in the contact region

In order to quantify this convergence better, the percent deviation of the total vertical load at a given value of m from the total vertical load at $m = 12$ is plotted as m increases.

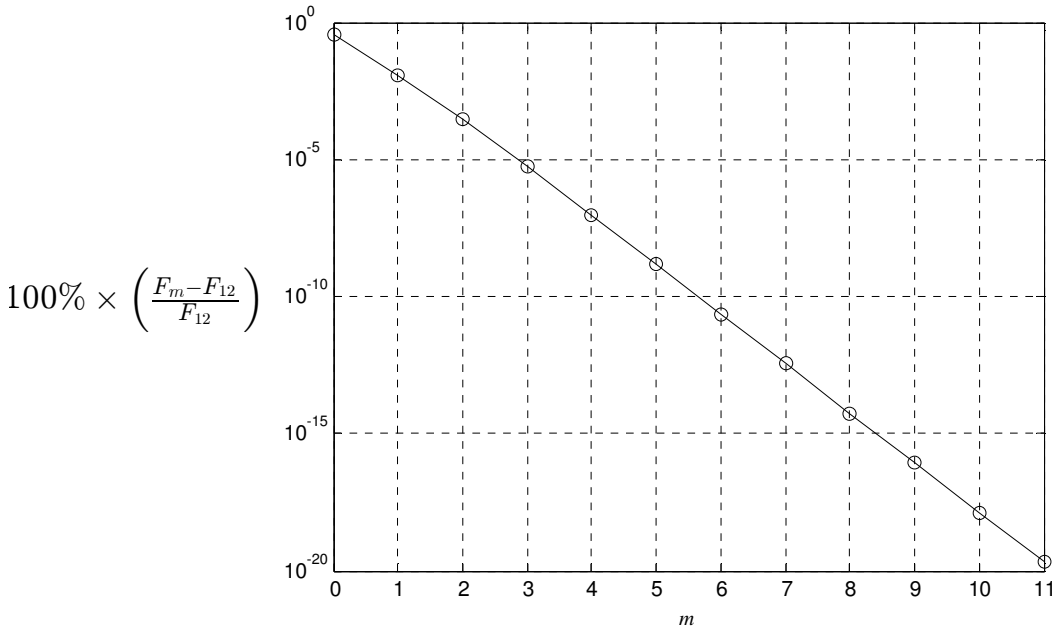

Figure 3.13. Percent error in the total vertical force

Ultimately, with these inputs, the total vertical load converges to $4.385\ \mathrm{kN}$.

3.3.4.4. Summary

From the evidence shown in the previous three sections, it is clear that the solution is converging and that using $m = 12$ produces an extremely accurate solution. This is useful when parameters producing more complicated pressure profiles are used.

3.4. Finite Element Validation

In order to determine the accuracy of the method to account for non-linear behavior described in Chapter 2, the load vs. deflection curve for both the linear and "non-linear" models are compared to the non-linear finite element model of a non-pneumatic tire, which was used by Gasmi, et al. [1]to validate the analytical model for the non-pneumatic tire for small deformations.

Using the method described in Chapter 2, the total vertical load is calculated using

$$F = F_S + (P - P^*)A \tag{3.5.6}$$

where F_S is the load applied to the tire when it is inflated with an inflation pressure of P^*, and A is the contact area. When F_S is plotted along with the linear solution and the Abaqus non-linear solution, Figure 3.14 is obtained.

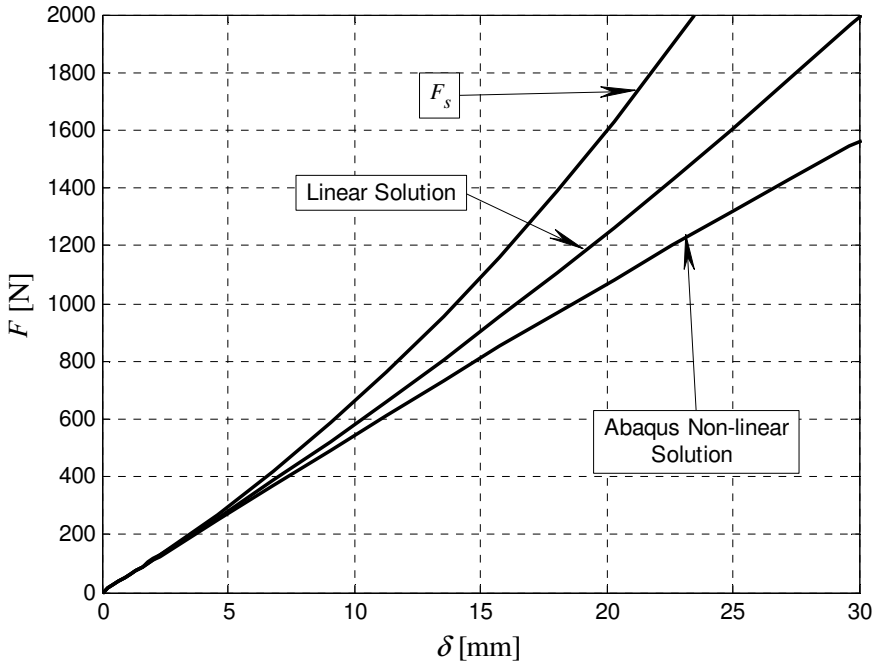

Figure 3.14. Comparison of the load vs. deflection curves for F_S, the linear solution, and the Abaqus non-linear solution

The load vs. deflection curve for F_S is proposed to be the most accurate loading combination for the linear model in terms of error induced by large deformations. As such, this load-deflection is proposed to be very close to what a finite element model would predict with non-linear geometry taken into account. The only approximation made in achieving this result was the approximation associated with a linear solution. When the inflation pressure term is

added to F_S, which does introduce an approximation since superposition does not apply in this contact problem, the total load vs. deflection curve softens to match the Abaqus non-linear solution as shown in Figure 3.15.

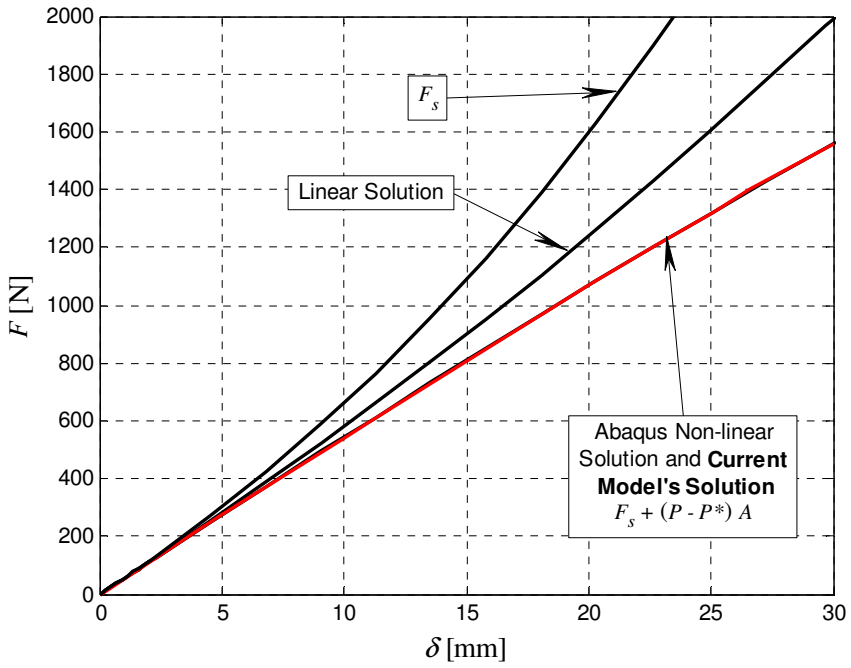

Figure 3.15. Comparison of the load vs. deflection curves for F_S, the linear solution, the Abaqus non-linear solution, and the current model's solution

From this, it is clear that the described solution procedure effectively allows the analytical model to account for the non-linear behavior present in the tire even for large deformations. The accuracy of these results is important to understand since it is unknown how significantly the assumptions affect other quantities such as the radius of curvature and internal moment of the belts entering the contact region. That is, while it is apparent that the assumptions made greatly increase the accuracy of the calculation of the vertical load, this may come at an undesirably high cost in the calculation of other results. Therefore, in order to

quantify the error present in the calculation, the quantity $N\sin(\phi)$ is presented in Figure 3.16 for both a non-pneumatic and a pneumatic tire. This quantity corresponds to the force component that is not taken into consideration when equilibrium is based in the undeformed position.

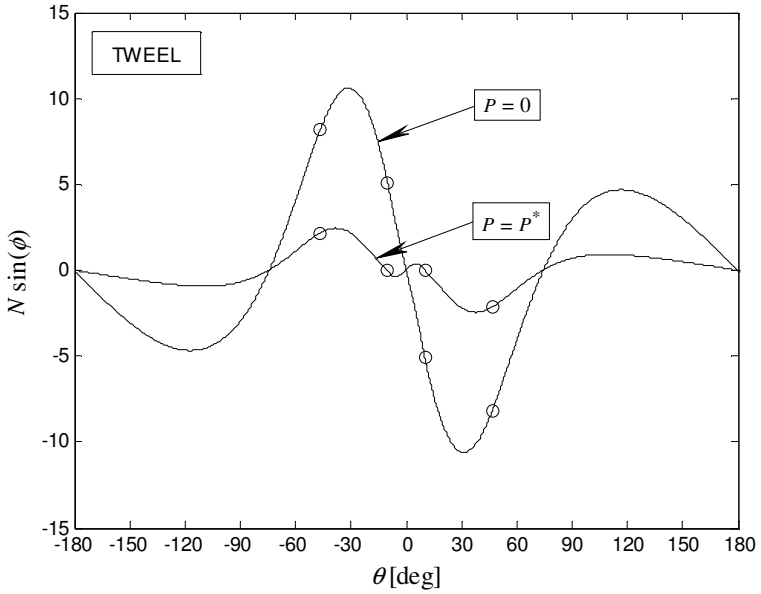

(a)

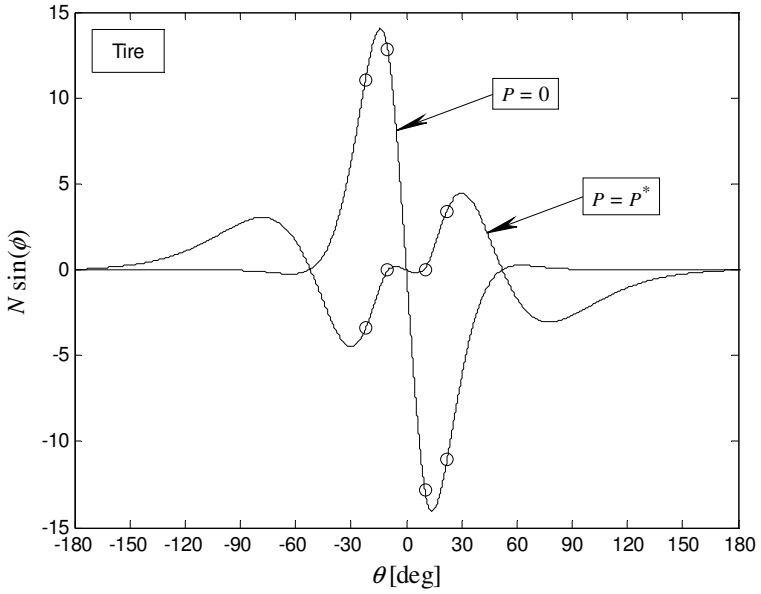

(b)

Figure 3.16. The force component $N\sin(\phi)$ that is not taken into account when equilibrium is considered in the undeformed position for (a) a non-pneumatic tire and (b) a pneumatic tire. In each case the $P = 0$ and $P = P^*$ cases are presented.

When the same quantity is plotted for both a non-pneumatic and pneumatic tire inflated to 2 bar, the results are similar to the $P = 0$ results for both tires except the maximum value for the non-pneumatic tire increases to about 21 N, and the maximum value for the pneumatic tire increases to about 850 N. This shows that inflating the tire to an inflation pressure of P^* can significantly increase the accuracy of the result. However, the results in Figure 3.16a raise the question of whether the solution could be improved further by choosing a different value of P^* such that, for example, it minimizes the maximum value of $N\sin(\phi)$ in the entire tire. Because the greatest concern at this point is that the vertical load is accurately calculated, in Figure 3.17 the magnitude of the vertical load from Figure 3.15 is plotted as a function of P^* for a given amount (22.6 mm) of vertical deflection. In this figure, the non-linear force from Figure 3.15 and the special value of $P^* = P^*_{\text{selected}}$ that corresponds to $N(\theta_L) = 0$ are indicted in the figure.

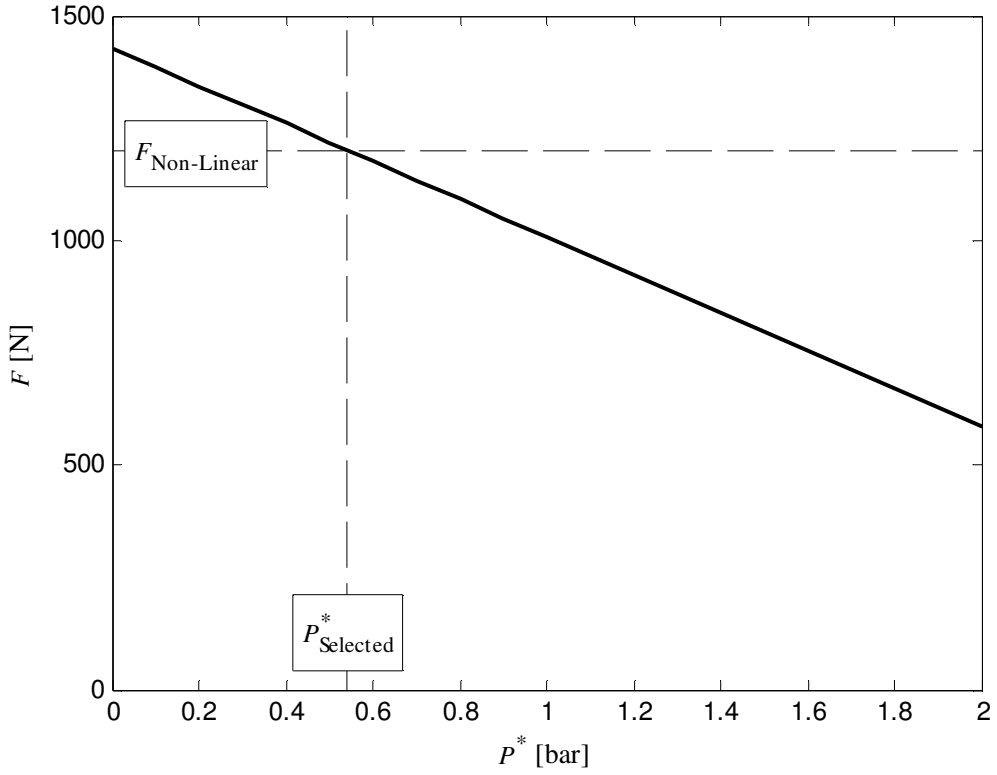

Figure 3.17. The calculated load for various magnitudes of the pressure, P^*, compared to the true value of $P^* = P^*_{selected}$.

From this figure, it is clear that the selected value of P^* that corresponds to $N(\theta_L)$ equal to zero is the best choice and allows the calculated vertical load to precisely match the load from the non-linear finite element model.

3.5. Experimental Validation

Based on the validations presented in the previous sections, given accurate input parameters, it is believed that the model should consistently be able to reproduce experimental results for a pneumatic tire. The figure below shows the comparison of the model's results using the parameters in Table 3.1 (which were assumed to be pressure independent) and

experimental data obtained from Michelin for a load vs. deflection test at various inflation pressures.

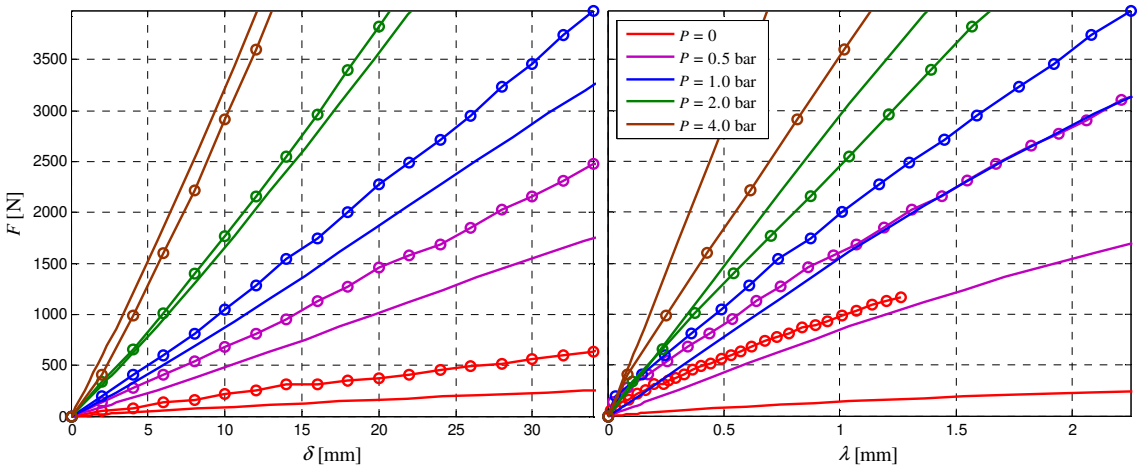

Figure 3.18. Comparison of the experimental data (-o-) and the theoretical prediction (—) for the load vs. deflection (left) and load vs. counter-deflection (right) results using the parameter set that allows the results to come closest to matching the data for $P = 2$ bar

These results show that the model gives a somewhat accurate prediction for an inflation pressure of 2 bar, but at lower pressures, the prediction is too soft and at higher pressures, the prediction is too stiff. Possible reasons for these discrepancies will be presented in Chapter 4, which will also include sensitivity analyses of the stiffness parameters. Additionally, these results are repeated for the set of parameters that allow the results to match the data for the uninflated tire. These are shown in

Figure 3.19.

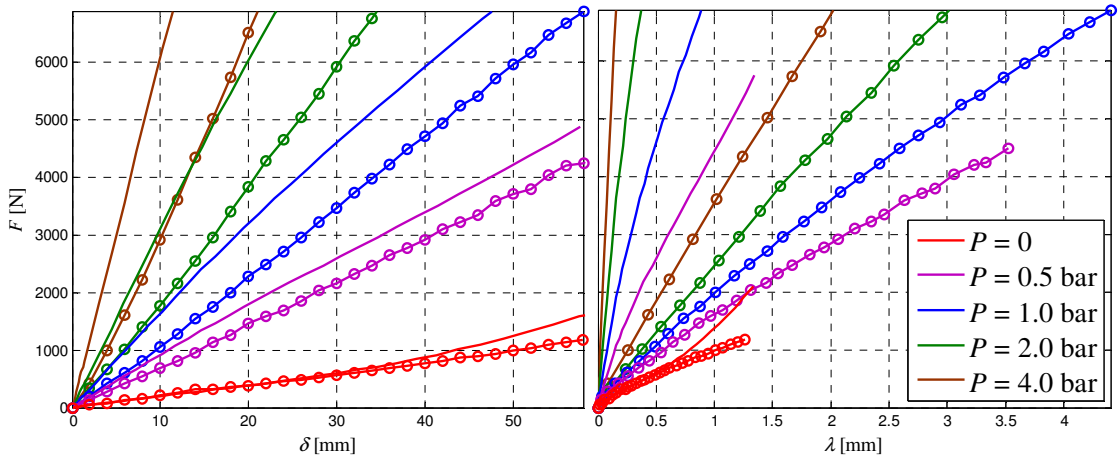

Figure 3.19. Comparison of the experimental data (-o-) and the theoretical prediction (—) for the load vs. deflection (left) and load vs. counter-deflection (right) results using the parameter set that allows the results to come closest to matching the data for $P = 0$

It should be noted here that while the results over the entire range of inflation pressures are not as close using this parameter set as they were for the parameter set used in Figure 3.18, they do match the experimental data for greater magnitudes of deformation.

An important requirement for any set of inputs is that they allow the contact pressure to be 10 percent higher than the inflation pressure for normal inflation pressures and contact lengths. This is because, at normal inflation pressures, the tire's behavior is primarily due to membrane behavior. Figure 3.20 shows the contact pressure for both the inflated and deflated tires compared to the inflation pressure for the case of a ten degree contact angle, which corresponds to a displacement of $\delta = 24.1$ mm for an inflated tire and $\delta = 14.6$ mm for a deflated tire.

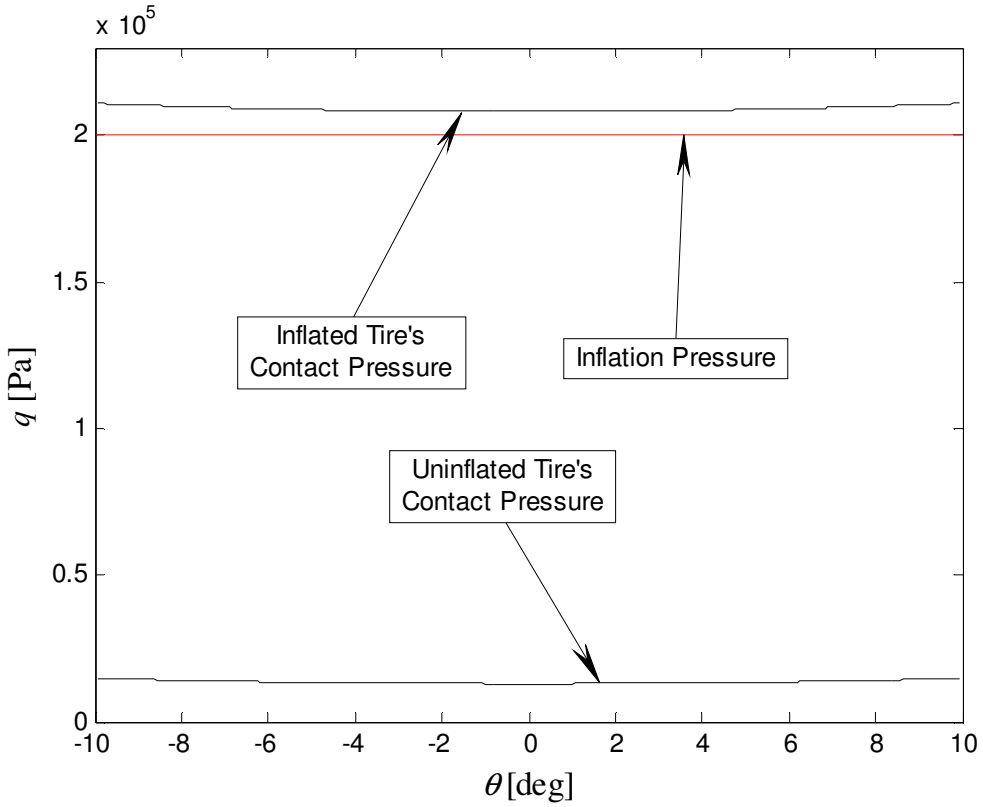

Figure 3.20. Contact pressure of both an inflated and uninflated tire compared to the inflation pressure used in the inflated tire

This shows that the model is predicting the expected contact pressure for a given inflation pressure.

3.6. Conclusion

It has been shown that the solution found in Chapter 2 satisfies the governing differential equations, and is also symmetric, continuous across the regions boundaries, and converges as the value of m increases. Furthermore, it has been shown that the model can reproduce the results from a non-linear Abaqus model. This provides great confidence that the solution is mathematically accurate and can accurately represent reality well. However, the inability to precisely match the experimental load vs. deflation and load vs. counter-deflection

data shows that more work needs to be done to be able to accurately calculate the stiffness parameters.

WORKS CITED

[1] A. Gasmi, P. F. Joseph, T. B. Rhyne and S. M. Cron, "Development of a Two-Dimensional Model of a Compliant Non-Pneumatic Tire," *International Journal of Solids and Structures,* 2012.

[2] R. D. McGinty, T. B. Rhyne and S. M. Cron, "Analytical Solution for the Stresses Arising in +/- Angle Ply Belts of Radial Tires," *Tire Science and Technology,* vol. 36, no. 4, pp. 244-274, 2008.

CHAPTER 4
–
SENSITIVITY STUDIES

4.1. Introduction

The model developed in Chapter 2 and validated in Chapter 3 can quickly calculate results for many cases over a wide range of parameters. The two sets of inputs used in Chapter 3 will now be used as base-cases to perform two sensitivity studies on all the parameters that are possible with the model. These parameters are presented in Table 3.1.

4.2. Load vs. Deflection and Load vs. Counter-deflection

The relationship between the total vertical load and the vertical deflection at the bottom of the tire is an important determining factor in vehicle ride. The counter-deflection is the amount of deflection at the top of the tire in response to an applied load at the bottom of the tire and is a useful measure to check that the predicted deformed shape of the tire matches the actual shape. Comparison with these two force-displacement measures is non-trivial validation tests for the model.

The effect of the various structural parameters on this relationship is studied by varying individual parameters and calculating the total vertical load, the vertical deflection, and the counter-deflection that result from imposing contact angles ranging from 0 to 20 degrees on the tire.

4.2.1. P = 2 bar Sensitivity Study

Figure 4.1 shows the sensitivity of these characteristics to the value of EA. From this, it is clear that both the vertical deflection and the counter-deflection of the tire are mostly unchanged by changing the value of EA.

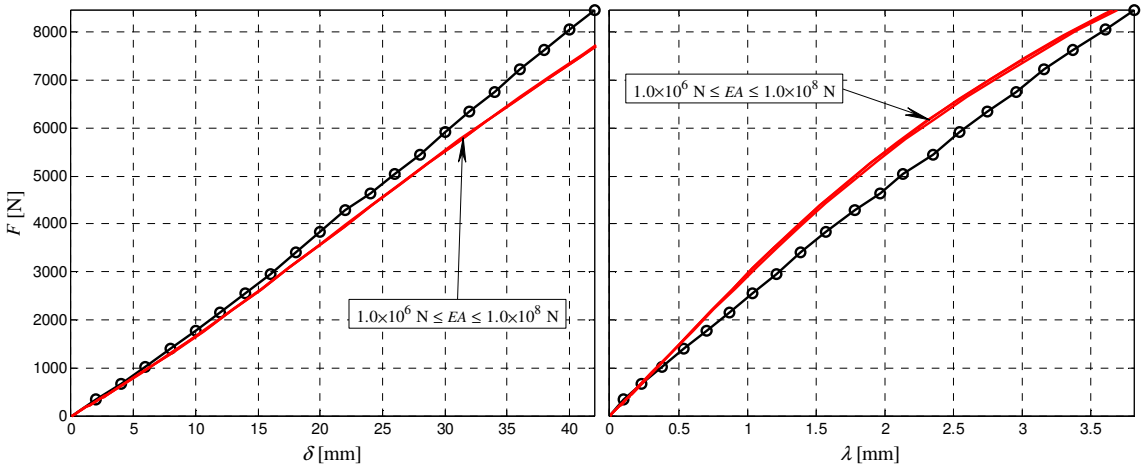

Figure 4.1. Sensitivity of the relationship between the total vertical load, the vertical deflection, and the counter-deflection to the axial stiffness of the belts, EA

In Figure 4.2, the variation of the results in response to changing the bending stiffness is observed. It is clear from this that increasing EI stiffens the initial stiffness and softens the final stiffness of both results. This is primarily due to the fact that while increasing EI increases the vertical load corresponding to a given contact length only slightly, it requires a greater vertical deflection to produce a small contact length and a smaller vertical deflection to produce a large contact length, compared to the magnitude of the vertical deflection at the small EI. This has an effect on the counter-deflection because the length of the belts must be mostly conserved (due to the high value for EA) and decreasing the contact length corresponding to a given vertical deflection requires a greater expansion at the top of the tire.

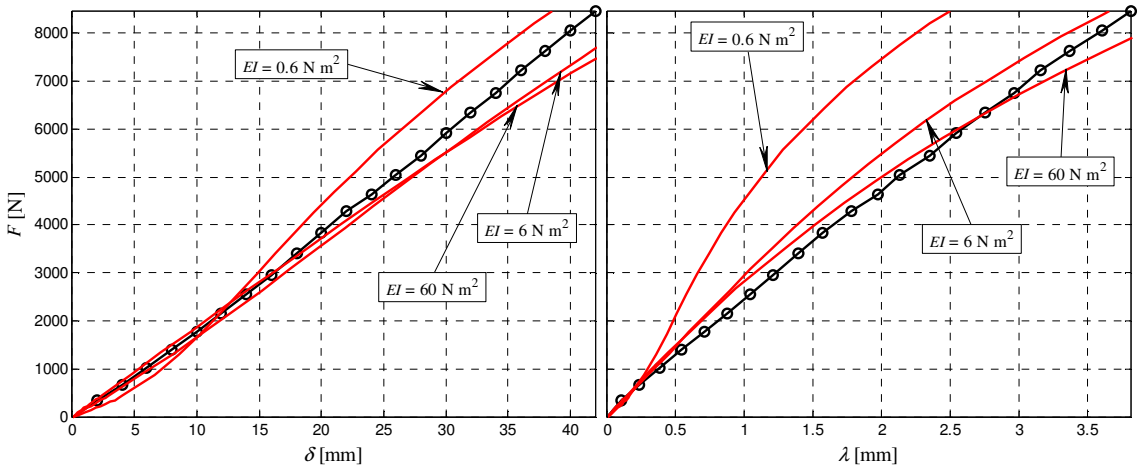

Figure 4.2. Sensitivity of the relationship between the total vertical load, the vertical deflection, and the counter-deflection to the bending stiffness of the belts, EI

For the results in Figure 4.3, the effect of the shear stiffness, GA, can be seen to have an significant impact on the initial stiffness, but does not affect the stiffness much as the deformation becomes large. Again this primarily due to the fact that increasing GA increases the amount of vertical deflection required to achieve a given contact length.

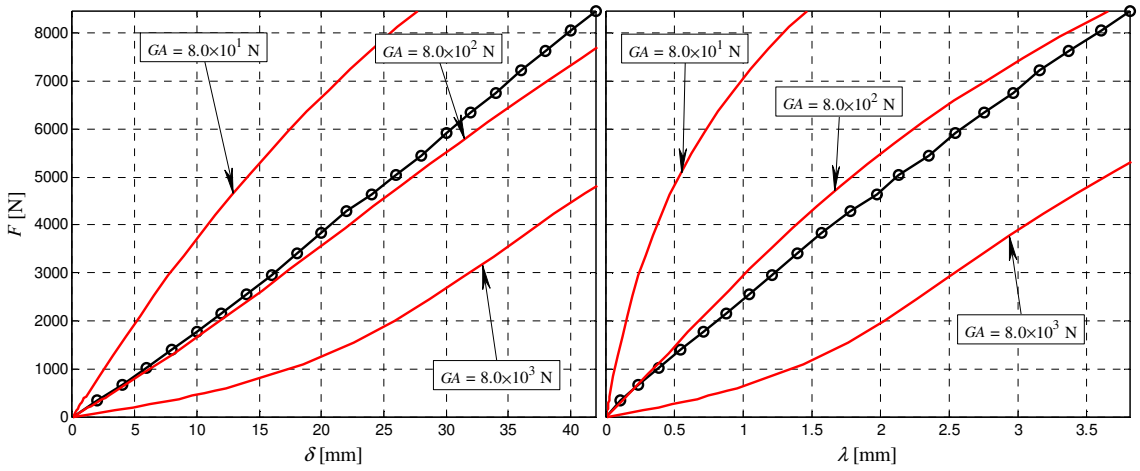

Figure 4.3. Sensitivity of the relationship between the total vertical load, the vertical deflection, and the counter-deflection to the shear stiffness of the belts, GA

Figure 4.4 shows the sensitivity of the results to the circumferential stiffness of the sidewall. These show that increasing this sidewall stiffness has more of an effect on the counter-deflection than on the vertical deflection. This is again due to the effect of K_θ on vertical deflection for a given contact length, since the total load for a given contact length remains constant for the most part.

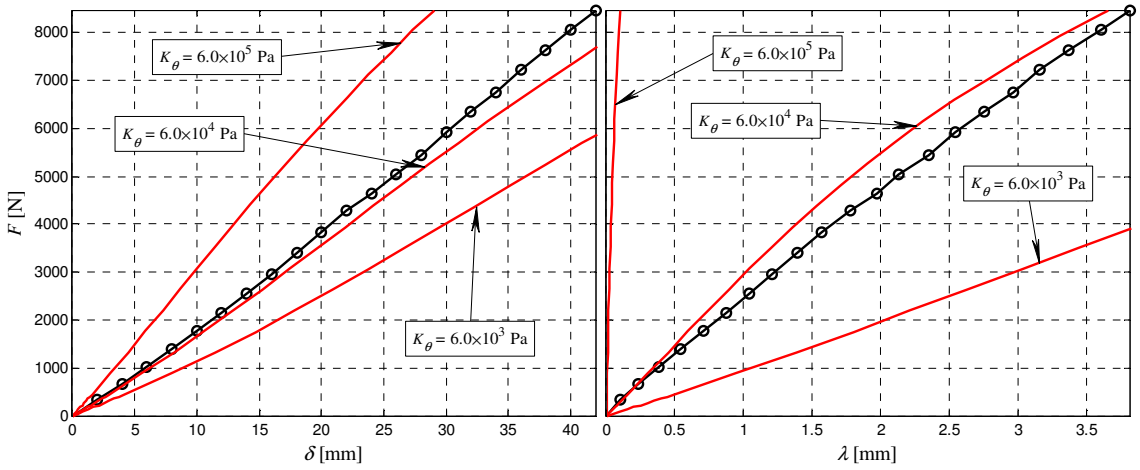

Figure 4.4. Sensitivity of the relationship between the total vertical load, the vertical deflection, and the counter-deflection to the circumferential stiffness of the sidewall, K_θ

Figure 4.5 shows the effect of the radial stiffness of the carcass in tension on the load-deflection relationship. This shows that stiffening the sidewall in the radial direction corresponds to a significant increase in the vertical stiffness of the tire. The effect is again largely due to a change in the vertical deflection corresponding to a given contact length. Additionally, the counter-deflection shows that as the radial stiffness of the tire's sidewall in tension drops below a certain point, the counter-deflection suddenly becomes negative. This is primarily due to the tire expanding laterally in response to contact pressure, but not vertically. Therefore, all the length that previously went to expanding the top of the tire upward is going to expanding the tire laterally, in this case.

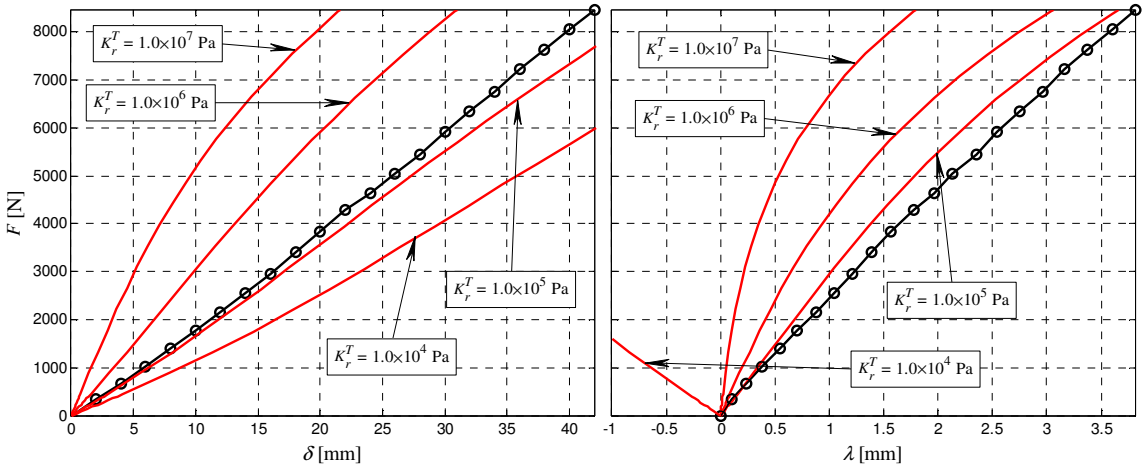

Figure 4.5. Sensitivity of the relationship between the total vertical load, the vertical deflection, and the counter-deflection to the radial stiffness of the sidewall in tension, K_r^T

In Figure 4.6, the radial stiffness of the sidewall in compression is observed to stiffen the initial stiffness of the tire, but as the bifurcation angle becomes larger, the change in the radial sidewall stiffness has less of an effect. The total load in this case does change some due to increases in K_r^C, but the dominant effect is still the change in vertical deflection corresponding to a given contact length.

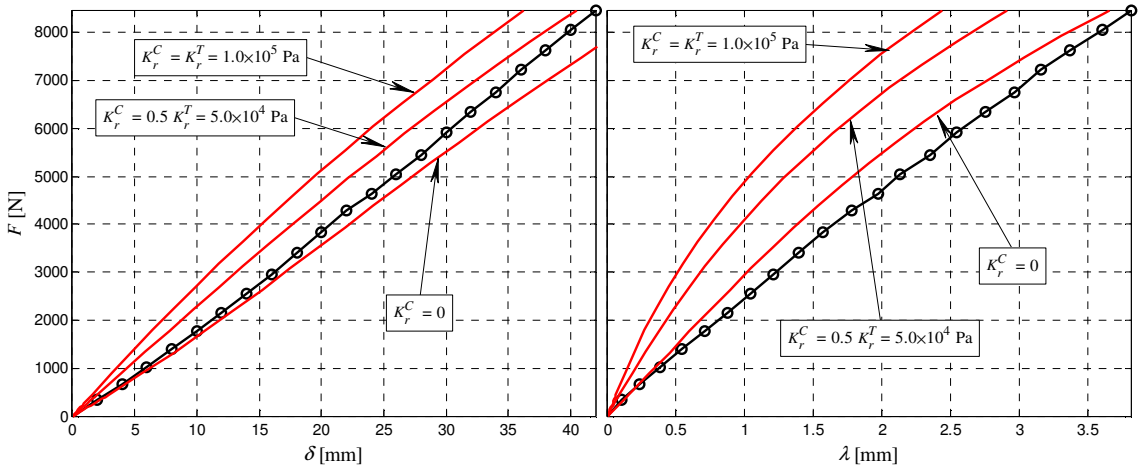

Figure 4.6. Sensitivity of the relationship between the total vertical load, the vertical deflection, and the counter-deflection to the radial stiffness of the carcass in compression, K_r^C

The results in Figure 4.7 show that the effect of the inflation pressure pre-tensioning is primarily that of softening the tire. This is because F_P^* reduces the effective inflation pressure applied to the tire, which in-turn reduces the stiffness of the tire. Therefore, when F_P^* is equal to $P\,b$, the vertical stiffness of the tire is the same as it would be for the uninflated tire with all other parameters the same.

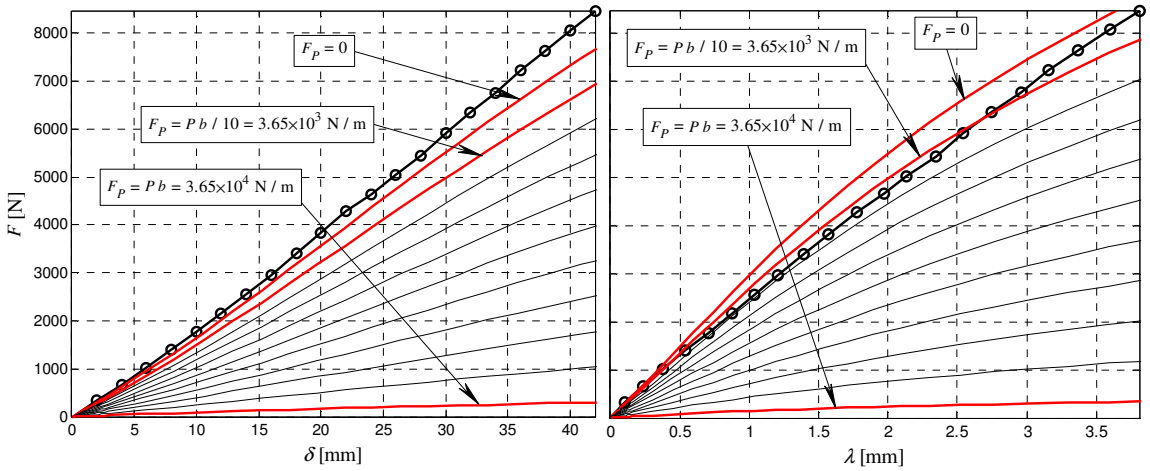

Figure 4.7. Sensitivity of the relationship between the total vertical load, the vertical deflection, and the counter-deflection to the pre-tensioning of the carcass, F_P

4.2.2. $P = 0$ Sensitivity Study

Figure 4.8 shows the sensitivity of these characteristics to the value of EA. From this, it is clear that while the vertical deflection is not very sensitive to the magnitude of EA (stiffening only slightly), the counter-deflection is much more sensitive to changes in EA.

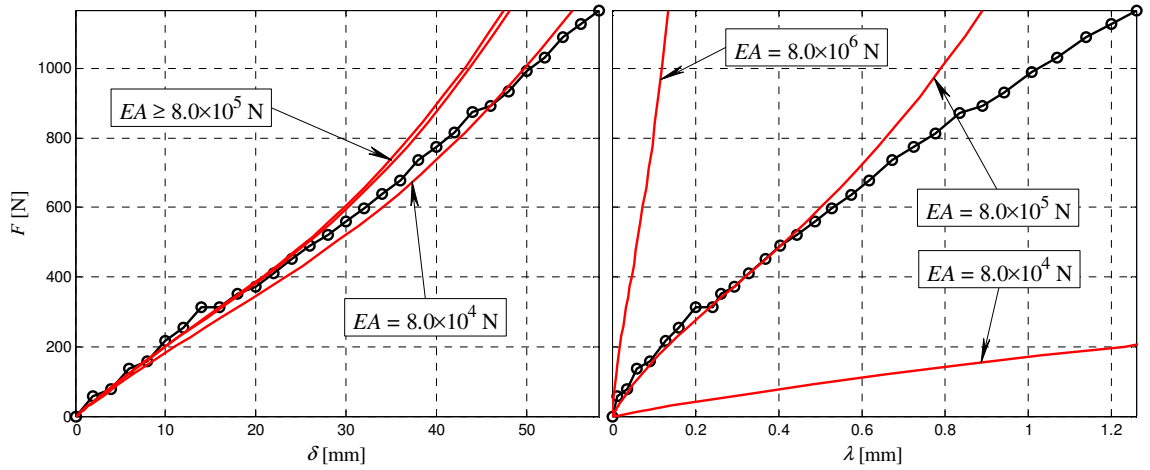

Figure 4.8. Sensitivity of the relationship between the total vertical load, the vertical deflection, and the counter-deflection to the axial stiffness of the belts, EA

Figure 4.9 shows that both the vertical deflection and the counter-deflection stiffen equally with increasing EI. This is primarily due to the fact that while increasing EI increases the vertical load corresponding to a given contact length only slightly, it requires a greater vertical deflection to produce a small contact length and a smaller vertical deflection to produce a large contact length, compared to the magnitude of the vertical deflection at the small EI. This has an effect on the counter-deflection because the length of the belts must be mostly conserved (due to the high value for EA) and decreasing the contact length corresponding to a given vertical deflection requires a greater expansion at the top of the tire.

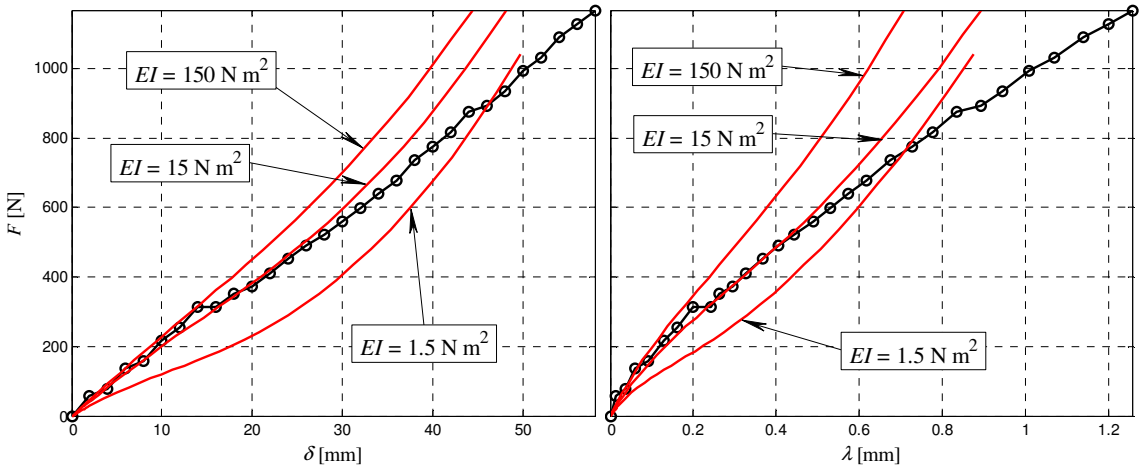

Figure 4.9. Sensitivity of the relationship between the total vertical load, the vertical deflection, and the counter-deflection to the bending stiffness of the belts, EI

For the results in Figure 4.10, the effect of the shear stiffness, GA, can be seen to have an significant impact on the initial stiffness, but does not affect the stiffness much as the deformation becomes large. Again this primarily due to the fact that increasing GA increases the amount of vertical deflection required to achieve a given contact length.

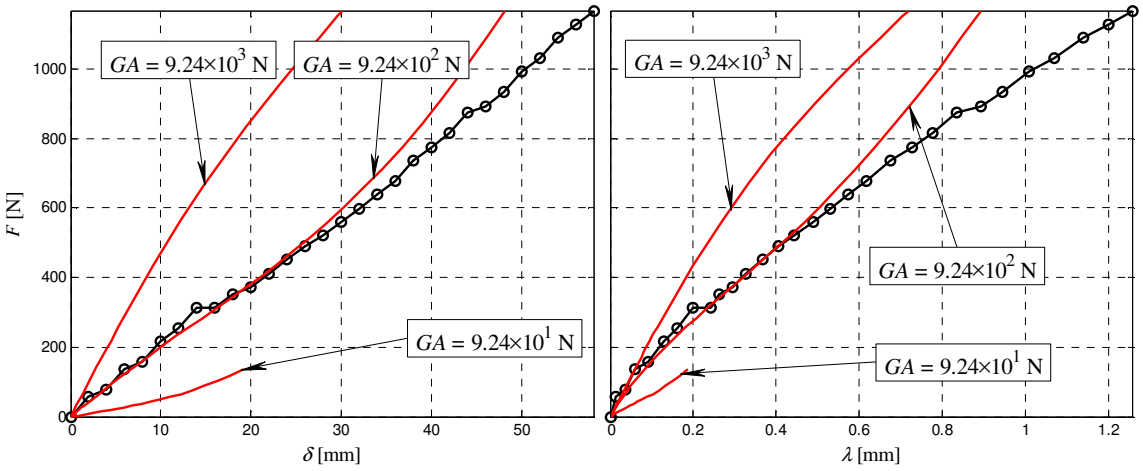

Figure 4.10. Sensitivity of the relationship between the total vertical load, the vertical deflection, and the counter-deflection to the shear stiffness of the belts, GA

Figure 4.11 shows the sensitivity of the results to the circumferential stiffness of the sidewall. These show that increasing this sidewall stiffness has more of an effect on the counter-deflection than on the vertical deflection. This is again due to the effect of K_θ on vertical deflection for a given contact length, since the total load for a given contact length remains constant for the most part. Additionally, contrary to the results in Figure 4.4, it is observed that increasing the circumferential stiffness can decrease the stiffness of the counter-deflection results.

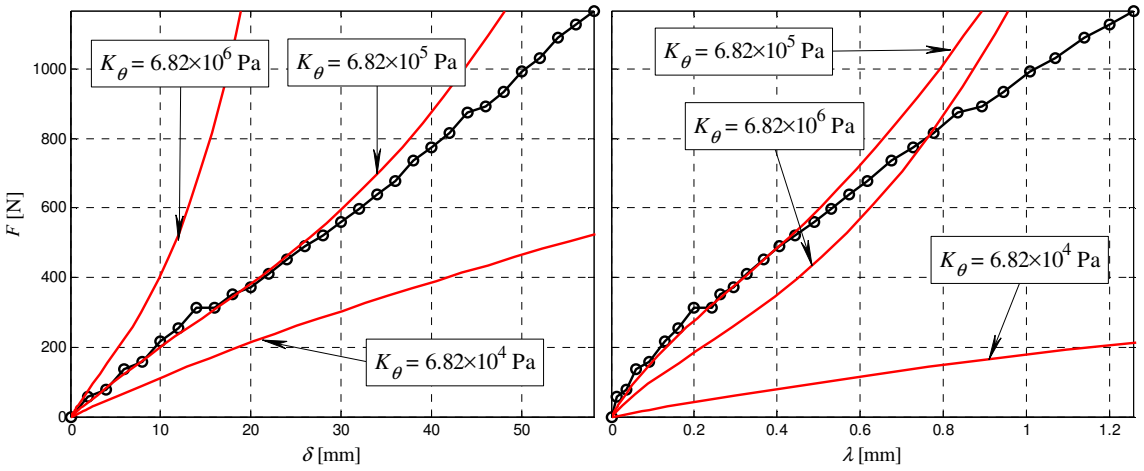

Figure 4.11. Sensitivity of the relationship between the total vertical load, the vertical deflection, and the counter-deflection to the circumferential stiffness of the sidewall, K_θ

Figure 4.12 shows the effect of the radial stiffness of the carcass in tension on the load-deflection relationship. This shows that stiffening the sidewall in the radial direction corresponds to only a small increase in the vertical stiffness of the tire. The effect is again largely due to a change in the vertical deflection corresponding to a given contact length. Additionally, it is observed that increasing the radial stiffness in tension can decrease the stiffness of the counter-deflection results.

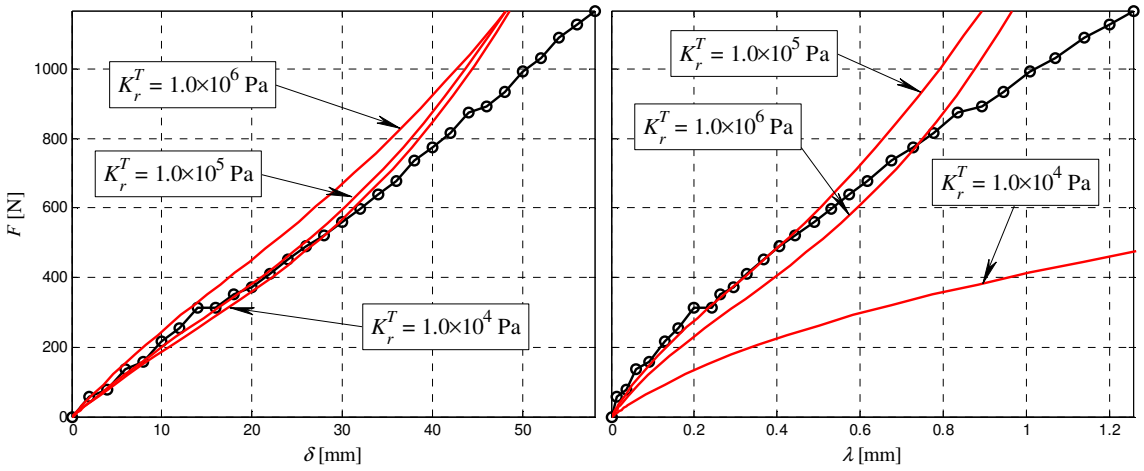

Figure 4.12. Sensitivity of the relationship between the total vertical load, the vertical deflection, and the counter-deflection to the radial stiffness of the sidewall in tension, K_r^T

In Figure 4.13, the radial stiffness of the sidewall in compression is observed to stiffen the initial stiffness of the tire, but as the bifurcation angle becomes larger, the change in the radial sidewall stiffness has less of an effect. The total load in this case does change some due to increases in K_r^C, but the dominant effect is still the change in vertical deflection corresponding to a given contact length.

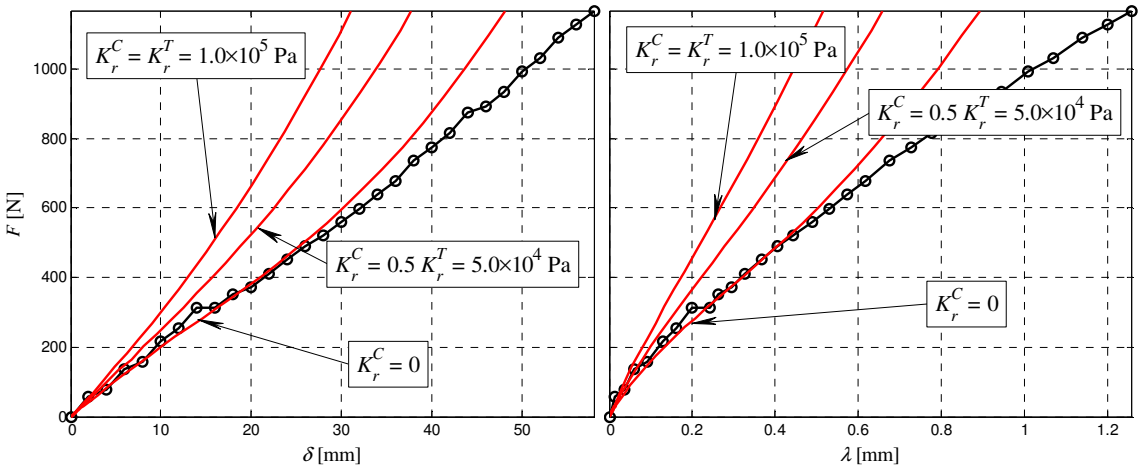

Figure 4.13. Sensitivity of the relationship between the total vertical load, the vertical deflection, and the counter-deflection to the radial stiffness of the carcass in compression, K_r^C

CHAPTER 5
–
DISCUSSION

5.1. Improvements to the Non-pneumatic Tire Model

The linear model of the non-pneumatic tire developed by Gasmi, et al. [1] has been improved to be able to represent a pneumatic tire. These improvements include the following:

- Addition of a torsional stiffness of the sidewall
- Addition of inflation pressure
- Addition of pre-tensioning
- Addition of a non-zero stiffness of the sidewall when it is compressed beyond its inflated position
- Accounting for the effects of non-linear geometry

The overall procedure to solve the pneumatic tire problem requires a so-called superposition to address the effect of inflation pressure in a large deformation mechanics problem. A structural solution, which is addressed within a linear context, is superposed to a non-linear membrane solution, in which the inflation pressure is easily accounted for. In the structural solution, which allows for any combination of pressure and applied force, a special pressure, P^*, is selected for a given force to minimize the error associated with large deformation by making the normal force zero at the edge of contact. As such, there is very little error associated with the structural solution. However, in the membrane solution, there is error since the effect of pressure will be slightly different in the deformed state (resulting from the linear model) than in the undeformed state. While this step does introduce some error, the

results have shown that it is sufficiently accurate to predict some behavior much more accurately than the original model can. For example, the non-pneumatic tire's non-linear force-deflection response was predicted almost exactly by adding back in the pressure P^* using this superposition procedure. Furthermore, it has been shown that the inaccuracies produced by not making that assumption for an inflated tire are far more significant than the inaccuracies produced by it. Therefore, the most difficult part of the solution has been obtained with a linear solution that does not seem to suffer from small deformation assumptions.

The purpose of the model was to gain some insight into how the vertical stiffness of the tire was affected by the structural parameters describing the tire. The sensitivity of the results to these parameters shows that indeed the vertical stiffness of the tire can be tuned by the structural parameters. This is useful in both determining how standard tires should be designed as well as guiding the design of tires in the future that are entirely different from the dominant tire design right now. For example, the developed model should be able to represent pneumatic tires for vehicles from golf carts to large earth-moving equipment. Furthermore, several tire companies have begun to develop tires that do not need air. A few examples are the run-flat tire, Michelin's TWEEL©, and Bridgestone's Air-Free Concept. All these types of tires could be modeled with this model. In fact, the only type of tire that the model would have difficulty modeling is a tire that requires a rounded cross-section, such as a motorcycle tire.

5.2. Obtaining Belt Stiffnesses

The belt stiffness parameters, EA, EI, and GA, were obtained by using analytical calculations to guide the matching of the experimental data. The primary source for this was McGinty, et al. [1], where the Young's modulus of the tire is derived in terms of the cord-rubber

composite material definition, with the assumption that all deformation takes place in the rubber surrounding the cords.

This initial prediction gave a value for EA that was too low to permit the results to match the experimental data. This was primarily because the calculated EA, being too low, resulted in the counter-deflection being far too small.

A different method to calculate EA involves the use of experimental data relating inflation pressure to the resulting radial expansion. Knowing the dimensions of the tire and the amount of inflation pressure pre-tensioning in the tire (i.e. F_P), the value of EA can be easily calculated. This yields a much higher value for EA which increases the amount of counter-deflection significantly.

From there, EA and the other belt stiffness parameters were varied further, in collaboration with Dr. Timothy Rhyne from Michelin to obtain the current parameter set, which matches the experimental data very well.

In this study, the belt parameters were not considered a function of the inflation pressure. However, the three-dimensional complexity of a tire likely makes the choices of "equivalent" values of EA, EI and possibly GA, a function of pressure, via, a "Poisson" type effect.

While all of these parameters can be permitted to become relatively small as far as the model's ability to produce a converged result is concerned, when they become too small, a solution can become significantly more difficult to find. Furthermore, the stiffness parameters cannot be permitted to become zero since that would significantly change the differential equations and therefore produce errors in the current solution.

5.3. Obtaining Sidewall Stiffnesses

Due to the lack of extensive study on the sidewall in the currently available literature, much of the understanding explained in this study had to be developed through new research. The choice of two of these parameters (K_θ and F_P) can be obtained using experimental data, as described at the beginning of Chapter 2.

These parameters along with the other two parameters (K_r^T and K_r^C) are then varied further in order to determine the set of parameters that permitted the best fit of the experimental data.

For this solution, all three parameters describing the sidewall in the radial direction (i.e. K_r^T, K_r^C, and F_P) can be permitted to become zero, since this does not significantly change the differential equations. However, because a non-zero K_θ does significantly change the differential equations, it is required to be non-zero in this solution.

The "pre-tensioning" parameter F_P was the most difficult to interpret within the context of the model results. A simple sensitivity analysis of this parameter keeping all other parameters constant, which includes K_r^C = 0, produced contact pressures that were below the inflation pressure. The reason for this is the incorrectly large tensile stress of F_P / b applied to the belt from the sidewall in the contact region. It appears as though a sensitivity analysis of the F_P parameter must also modify K_r^C to eliminate this effect, which means that K_r^C should be a function of the loading.

Similar to the belt stiffnesses, the sidewall stiffnesses were not considered functions of the inflation pressure in the sensitivity analyses or in the comparisons with the results.

5.4. Conclusion

In conclusion, it is apparent that the tire is a complex three-dimensional structure that is difficult to model; however, it seems that the model presented here can accurately predict its behavior under a static load very well. To say the least, it has been shown that the developed model can predict the behavior of many different types of tires. The evidence of this is two-fold. First, the non-linear finite element model of the non-pneumatic tire was matched precisely. Second, the pneumatic tire (with all of its non-linear behavior) is very difficult to model, and even in this case, the linear model does very well. Furthermore, the practicality for studying, designing, and comparing the behavior of a wide variety of tires is very beneficial.

WORKS CITED

[1] R. D. McGinty, T. B. Rhyne and S. M. Cron, "Analytical Solution for the Stresses Arising in +/- Angle Ply Belts of Radial Tires," *Tire Science and Technology,* vol. 36, no. 4, pp. 244-274, 2008.

[2] A. Gasmi, On the Modeling of Contact Problems for Curved and Straight Elastic Thin Continuums with Application to Non-Pneumatic Tires, Clemson, 2011.

CHAPTER 6
–
CONCLUSIONS AND FUTURE WORK

6.1. Conclusions

The following conclusions can be made from the completed research:

- The model developed by Gasmi, et al. [1] can be made much more general so that both pneumatic and non-pneumatic tires of many different types can be represented.
- A linear model of a pneumatic tire is possible as long as an assumption is made for accounting for the inflation pressure. This large deformation membrane assumption cannot be avoided when a linear model is used.
- The difficult "structural" portion of the solution can be obtained by a linear model that does not suffer from small deformation assumptions. This is accomplished by selecting loading parameters that minimize error due to the large deformation.
- Force-deflection, force-counter deflection, and pressure distribution over a large range of inflation pressures are predicted with reasonable accuracy given that a two-dimensional analytical model is attempting to address a highly non-linear three dimensional problem.
- The determination of stiffness parameters that allow the model to match experimental data is not a trivial matter.

6.2. Future Work

Several things could be done to improve upon the work that has been completed.

- Several experiments could be done to obtain better calculations of the input parameters. These experiments are the following:
    - Radial expansion resulting from inflation pressure
    - Rotation due to an applied torque at several inflation pressures
    - Measurement of both the stiffnesses of the sidewall in the radial direction at several different inflation pressures
    - Measurement of the belt's bending and shear stiffnesses

  The first two of these have already been done, but achieving greater resolution in the results could provide input parameters that are more accurate. The easiest way perform the last two experiments would probably be through the use of a finite element model, since a physical test would require the destruction of a tire and would probably be significantly more difficult.

- The model created by Gasmi, et al. [1] to validate the results for the non-pneumatic tire could be re-created for a pneumatic tire. The advantage of such a model is that the inclusion of geometric non-linearity can be easily turned on or off, which would allow for an evaluation of the superposition scheme required by the analytical model. This superposition scheme would not be required by the non-linear finite element model.

- Based on the above finite element model, it would be beneficial to find the conditions for which the assumptions made to account for the non-linear

geometry are not valid. For example, it is known that the moment predicted by the current model is slightly different from the actual moment in the tire; therefore, it would be interesting to determine how this difference is affected by increasing inflation pressure.

- Additional work could be done to determine whether the differences between the predicted results and the experimental data are the result of sidewall behavior not being captured by the current model or if this is merely caused by incorrect input parameters.

WORKS CITED

[1] A. Gasmi, On the Modeling of Contact Problems for Curved and Straight Elastic Thin Continuums with Application to Non-Pneumatic Tires, Clemson, 2011.